

“Numerical and experimental investigation of low Reynolds number wind turbine airfoils under stall and post-stall conditions”

Copyright © 2013, Elia Daniele.

All rights reserved. Printed in Italy. This publication is protected by copyright, and permission must be obtained from the publisher prior to any prohibited reproduction, storage in a retrieval system, or transmission in any form or by any means, electronic, mechanical, photocopying, recording, or likewise. For information regarding permissions, write to:

3D TECH SRLS Via San Vito, 65, 80014, Giugliano in Campania, Naples, Italy.

Type-setted with L^AT_EX and PGF/TikZ

Text printed in Italy at Universal Book SRL, Via S. Botticelli, 22, 87036 Rende, Cosenza.



UNIVERSITÀ DEGLI STUDI DI NAPOLI
FEDERICO II



Department of Industrial Engineering
School of Doctoral Research in Aerospace, Naval and Quality Engineering

NUMERICAL AND EXPERIMENTAL INVESTIGATION OF
LOW REYNOLDS NUMBER WIND TURBINE AIRFOILS
UNDER STALL AND POST-STALL CONDITIONS

CANDIDATE

Elia Daniele

TUTOR

Prof. Domenico P. Coiro

COORDINATOR

Prof. Luigi de Luca

Submitted on April 2013 for the XXV cycle

I, Elia Daniele, declare that this thesis titled, "Numerical and experimental investigation of low Reynolds number wind turbine airfoils under stall and post-stall conditions" and the work presented in it are my own work. I confirm that:

- this work was done wholly or mainly while in candidature for a research degree at this University;
- where any part of this thesis has previously been submitted for a degree or any other qualification at this University or any other institution, this has been clearly stated;
- where I have consulted the published work of others, this is always clearly attributed;
- where I have quoted from the work of others, the source is always given and with the exception of such quotations, this thesis is entirely my own work;
- I have acknowledged all main sources of help;
- where the thesis is based on work done by myself jointly with others, I have made clear exactly what was done by others and what I have contributed myself.

This PhD thesis has been defended in a public dissertation on May, 3rd 2013 under the judgement of a specialized commission composed by:

- Prof. Giorgio Guglieri, Department of Mechanical and Aerospace Engineering, Politecnico di Torino;
- Prof. Giulio Avanzini, Department of Innovation Engineering, Università del Salento;
- Prof. Salvatore Miranda, Department of Industrial Engineering, Università degli Studi di Napoli "Federico II".

April 2013
Department of Industrial Engineering
University of Naples Federico II
Naples

Elia Daniele

SOMMARIO

Questo lavoro riguarda un'indagine numerica e sperimentale di profili di turbine eoliche per bassi numeri di Reynolds in condizioni di stallo e post-stallo. Una verifica dei modelli semi empirici per alti angoli di attacco, precisamente il Viterna-Corrigana e l'AERODAS di Spera, è richiesta per consolidare l'affidabilità dei dati di ingresso per i codici di calcolo delle prestazioni delle turbine eoliche ad asse verticale (in inglese VAWT) basati sulla teoria dell'elemento di pala e della quantità di moto (in inglese BEM) e in aggiunta la predizione delle prestazioni per le turbine eoliche ad asse orizzontale (in inglese HAWT) per le quali un controllo di stallo passivo deve essere garantito da un'affidabile distribuzione dei coefficienti aerodinamici in post-stallo. Una grossa sfida è costituita dal basso numero di Reynolds relativo al fenomeno (considerando VAWT per installazione urbana e piccola taglia di generazione di potenza elettrica) e la presenza di un possibile stallo indotto da esplosione di bolla laminare. In caso in cui non si osservi un effetto della bolla laminare sul comportamento allo stallo, è comunque presente una forte dipendenza del massimo coefficiente di portanza ottenibile dalla intensità di turbolenza. Viene prestata inoltre attenzione alle condizioni operative non pulite di una VAWT come quelle presenti lontano nel tempo dal periodo di manutenzione in cui una transizione dal regime di flusso laminare al turbolento si può supporre essere promossa dall'accumulo di materiale di deposito e sporczia sulla regione del bordo d'attacco della pala. Simulazioni di fluidodinamica numerica (CFD) usando la libreria OpenFOAM ed un modello di turbolenza con transizione sono usate come confronto dei risultati sperimentali derivanti dalla campagna di prove condotta nella galleria del vento a camera di prova chiusa del Dipartimento di Ingegneria Industriale della Università degli Studi di Napoli "Federico II", per condizioni di transizione libera e bloccata. Un successivo confronto con gli esperimenti dell'Università di Delft è stato fatto per numeri di Reynolds simili, ed inoltre, un'analisi dell'effetto del bloccaggio attraverso un'altra campagna di prove nella galleria a camera di prova aperta è stata condotta per capire l'influenza delle pareti della galleria sul secondo picco del coefficiente di portanza e sul massimo valore del coefficiente di resistenza.

ABSTRACT

This work concerns a numerical and experimental investigation of low Reynolds number wind turbine airfoils under stall and post-stall conditions. A verification of high angle of attack semi empirical models, namely Viterna-Corrigan and Aerodas from Spera, is needed to assess the input data reliability for Blade Element Momentum (BEM) based Vertical Axis Wind Turbine (VAWT) performance code and also the performance predictions for Horizontal Axis Wind Turbine (HAWT) where passive stall control must be guaranteed by a reliable post-stall aerodynamic coefficients distribution. A great challenge is inherited by the low Reynolds number related to the phenomenon (considering VAWT for urban installation and small size generation) and the presence of possible laminar bubble burst induced stall. In case for which no laminar bubble promotion is observed on the stall behavior, still a strong dependency on turbulence intensity is present for the maximum lift coefficient attainable. Attention is also paid to not clean VAWT operating conditions as those occurring far from maintenance period in which a transition from laminar to turbulent flow regime could be supposed to be promoted by dirty material accumulation on the blade leading edge region. Computational Fluid Dynamics (CFD) simulations using OpenFOAM library and a transitional turbulence model are used as a comparison for the experimental results derived from the test campaign conducted in the closed test section wind tunnel facility of the Department of Industrial Engineering of University of Naples, for both free and fixed transition condition. A further comparison with Delft University experiments is performed for similar Reynolds number, and moreover, an analysis of blockage effect by means of another test campaign in the open test section wind tunnel facility is conducted to understand the influence of wind tunnel walls on secondary lift coefficient peak and maximum drag coefficient value.

RINGRAZIAMENTI

Un lavoro durato tre anni ha potuto vedere la luce grazie anche al supporto ed alla competenza delle tante persone che mi hanno aiutato. In primo luogo il gruppo di ricerca ADAG, guidato dal Prof. Coiro, grazie al quale ho potuto preparare ed eseguire la parte sperimentale di questo lavoro ed avere la possibilità di seguire i molti studenti che hanno svolto la loro tesi di laurea nel nostro ambito di ricerca, confrontandomi spesso con tanti diversi ed affascinanti problemi. In secondo luogo voglio ringraziare il Prof. Peinke, il Dr. Stoevesandt e la Dr. Ing. Heinzemann, insieme ai ragazzi dell'IWES Fraunhofer, del centro Forwind e dell'Università di Oldenburg, per la bellissima esperienza sia lavorativa che umana che mi hanno permesso di vivere insieme a loro ad Oldenburg. In terzo luogo voglio ringraziare la Prof. Mallozzi ed i colleghi Egidio D'Amato, Angelo De Fenza, Pierluigi Della Vecchia e Giovanni Petrone, per aver contribuito a stimolare la mia curiosità ed aver intrapreso numerose ed affascinanti attività di ricerca che hanno contribuito al mio arricchimento.

Infine voglio ringraziare la mia famiglia per quello che "sono" e per la serenità, il sostegno, la comprensione, la disponibilità ed in generale l'affetto che non mi hanno mai fatto mancare da tanto tempo quanto io possa ricordare. Ai miei amici voglio dire grazie per la felicità dei tanti momenti trascorsi insieme e per aver letteralmente riempito i miei giorni: Anna, Anna Chiara, Annagrazia, Dino, Domenico, Lucio, Luigi, Simone, Stefania ed Umberto.

L'ultimo ringraziamento è per chi non può leggerlo nemmeno. Per chi mi ha fatto amare il disegno e le "cause perse", conoscere la dignità del lavoro ed il valore di una promessa. Per colui la cui mano ho stretto quando la sua presa salda più non era, colui da cui non posso più ricevere un cenno per quel che di buono avrò fatto seguendo il suo esempio. Il mio grazie a te, cui devo il mio nome.

Elio Daniele

ACKNOWLEDGEMENTS

A three years long work has come into being thanks also to the support and skill of all the people that have helped me. Firstly the ADAG research group, lead by Prof. Coiro, thanks to whom I have been able to prepare and perform the experimental part of this work together with the chance of supervising many of the students that have conducted their thesis within our research field, facing in many cases with several different and fascinating problems. Secondly, I would like to thank Prof. Peinke, Dr. Stoevesandt and Dr. Ing. Heinzelmann, together with the guys from IWES Fraunhofer, Forwind centre and Oldenburg University, for the amazing both working and human experience they let me spent among them in Oldenburg. Thirdly, I would like to thank Prof. Mallozzi and the colleagues Egidio D'Amato, Angelo De Fenza, Pierluigi Della Vecchia and Giovanni Petrone, for their contribution in stimulating my curiosity and taking up several and fascinating research activities that have contributed to my enrichment.

Finally, I would like to thank my family for what I "am" and for the serenity, the support, the comprehension, the availability and in general the affection that they have never let me feel missing since as much time as I can remember. To my friends I would like to say thanks for the happiness of all the moments we shared and for literally have filled up my days: Anna, Anna Chiara, Annagrazia, Dino, Domenico, Lucio, Luigi, Simone, Stefania and Umberto.

The last thanks goes to whom cannot even read it. To whom let me love drawing and the "lost causes", to whom let me know the dignity of gainful employment and the value of a promise. To whom whose hand I have hold when his grasp not more firm was, to the man from whom I cannot expect any more a nod for what good I would have done following his model. My thanks to you, whom I owe my name.

Elia Daniele

[...]

*I shall be telling this with a sigh
somewhere ages and ages hence:
two roads diverged in a wood, and I,
I took the one less traveled by,
and that has made all the difference.*

ROBERT FROST (1874-1963), in *Mountain Interval*, 1920.

CONTENTS

1	Introduction	1
2	Method	5
2.1	Numerical methodology	5
2.1.1	$k_T - k_L - \omega$ transition model	6
2.1.2	Roughness sensitivity	12
2.1.3	Simulations set-up	13
2.2	Semi-empirical models	19
2.2.1	Viterna-Corrigan	19
2.2.2	AERODAS	24
2.3	Experimental set-up	29
2.3.1	Corrections of measurements	32
3	Results	35
3.1	A test case: DU-97-W-300	35
3.1.1	Free transition	35
3.1.2	Fixed transition	37
3.2	Naca 0018	40
3.2.1	Experiments	40
3.2.2	Numerical simulations	50
3.2.3	Post-stall modelling	65
3.2.4	Comparison with Delft experiments	86
3.2.5	Effect of wind tunnel wall on blockage	90
3.3	GT10	94
3.3.1	Numerical simulations	94
3.3.2	Post-stall modelling	97
4	Conclusions	103
A	$k_T - k_L - \omega$ model formulation	105

LIST OF FIGURES

Figure 1	VAWT scheme for operating condition	1
Figure 2	VAWT and HAWT of size compatible for incentive feeding	4
Figure 3	Decay law application	10
Figure 4	Theoretical decay	11
Figure 5	Theoretical vs. numerical decay for $T_i = 3.6\%$	11
Figure 6	Trip schematization with major parameters indication	12
Figure 7	DU-97-W-300 airfoil geometry	12
Figure 8	Trip detail in numerical grid	13
Figure 9	Blockage effect on lift coefficient	14
Figure 10	Blockage effect on drag coefficient	14
Figure 11	Blockage effect on velocity field at 40 degrees for $H/c = 5$ and $H/c = \infty$	15
Figure 12	Blockage effect on velocity field at 60 degrees for $H/c = 5$ and $H/c = \infty$	16
Figure 13	Blockage effect on velocity field at 70 degrees for $H/c = 5$ and $H/c = \infty$	17
Figure 14	Blockage effect on velocity field at 90 degrees for $H/c = 5$ and $H/c = \infty$	18
Figure 15	Sketch of Viterna-Corrigan lift coefficient distribution (solid line) together with flate plate theory result (dashed line) for some measurements data (squares)	21
Figure 16	Sketch of Viterna-Corrigan drag coefficient distribution (solid line) together with flate plate theory result (dashed line) for some measurements data (squares)	22
Figure 17	Effects of blade planform on aerodynamic power vs wind speed	23
Figure 18	Effects of V.C. settings on aerodynamic power vs wind speed	23
Figure 19	Configurations of the proposed AERODAS models for calculating lift and drag coefficients in the pre-stall and post-stall regimes. Input parameters are underlined. Lift coefficient model (from [66]).	26
Figure 20	Configurations of the proposed AERODAS models for calculating lift and drag coefficients in the pre-stall and post-stall regimes. Input parameters are underlined. Drag coefficient model (from [66]).	27
Figure 21	Configuration of test section with the additional wall	29
Figure 22	NACA 0018 sketch of the pressure ports distribution on the mid span section	29
Figure 23	NACA 0018 model pressure ports distribution on the mid span section, upper side surface	30
Figure 24	NACA 0018 model arrangement in the closed test section wind tunnel with additional wall	30
Figure 25	Mushroom shaped stall cell from literature and experiments	31

List of Figures

Figure 26	NACA 0018 comparison of numerical and experimental measurements for drag coefficient vs AoA at about $Re = 300e3$	32
Figure 27	Trip detail in numerical grid for DU-97-W-300 airfoil.	36
Figure 28	DU-97-W-300, lift coefficient vs angle of attack	36
Figure 29	DU-97-W-300, drag coefficient vs angle of attack	37
Figure 30	DU-97-W-300, lift coefficient vs angle of attack tripped case	38
Figure 31	DU-97-W-300, drag coefficient vs angle of attack tripped case	38
Figure 32	NACA 0018 detail of experimental lift coefficient vs angle of attack	40
Figure 33	NACA 0018 experimental lift coefficient vs angle of attack	41
Figure 34	NACA 0018 experimental drag coefficient vs angle of attack	42
Figure 35	NACA 0018 experimental aerodynamic efficiency vs angle of attack	42
Figure 36	NACA 0018 detail of experimental lift coefficient vs angle of attack for tripped case	43
Figure 37	NACA 0018 experimental lift coefficient vs angle of attack for tripped case	44
Figure 38	NACA 0018 experimental drag coefficient vs angle of attack for tripped case	45
Figure 39	NACA 0018 experimental aerodynamic efficiency coefficient angle of attack for tripped case	45
Figure 40	Comparison of lift coefficient for clean and tripped case at $Re = 115e3$	47
Figure 41	Comparison of drag coefficient for clean and tripped case at $Re = 115e3$	47
Figure 42	Comparison of lift coefficient for clean and tripped case at $Re = 230e3$	48
Figure 43	Comparison of drag coefficient for clean and tripped case at $Re = 230e3$	48
Figure 44	Comparison of lift coefficient for clean and tripped case at $Re = 290e3$	49
Figure 45	Comparison of drag coefficient for clean and tripped case at $Re = 290e3$	49
Figure 46	Trip detail in numerical grid for NACA 0018 airfoil	50
Figure 47	Comparison of lift coefficient distribution between experiments and numerical simulation at $Re = 115e3$	51
Figure 48	Comparison of drag coefficient distribution between experiments and numerical simulation at $Re = 115e3$	52
Figure 49	Comparison of lift coefficient distribution between experiments and numerical simulation at $Re = 230e3$	52
Figure 50	Comparison of drag coefficient distribution between experiments and numerical simulation at $Re = 230e3$	53
Figure 51	Comparison of lift coefficient distribution between experiments and numerical simulation at $Re = 290e3$	54
Figure 52	Comparison of drag coefficient distribution between experiments and numerical simulation at $Re = 290e3$	54

- Figure 53 Comparison of lift coefficient distribution between experiments and numerical simulation at $Re = 115e3$ for tripped case 55
- Figure 54 Comparison of drag coefficient distribution between experiments and numerical simulation at $Re = 115e3$ for tripped case 56
- Figure 55 Comparison of lift coefficient distribution between experiments and numerical simulation at $Re = 230e3$ for tripped case 56
- Figure 56 Comparison of drag coefficient distribution between experiments and numerical simulation at $Re = 230e3$ for tripped case 57
- Figure 57 Comparison of lift coefficient distribution between experiments and numerical simulation at $Re = 290e3$ for tripped case 58
- Figure 58 Comparison of drag coefficient distribution between experiments and numerical simulation at $Re = 290e3$ for tripped case 58
- Figure 59 Comparison of lift coefficient vs AoA between experiments and numerical simulation at $Re = 115e3$ for clean and tripped case 59
- Figure 60 Comparison of drag coefficient vs AoA between experiments and numerical simulation at $Re = 115e3$ for clean and tripped case 60
- Figure 61 Comparison of lift coefficient vs AoA between experiments and numerical simulation at $Re = 230e3$ for clean and tripped case 60
- Figure 62 Comparison of drag coefficient vs AoA between experiments and numerical simulation at $Re = 230e3$ for clean and tripped case 61
- Figure 63 Comparison of lift coefficient vs AoA between experiments and numerical simulation at $Re = 290e3$ for clean and tripped case 61
- Figure 64 Comparison of drag coefficient vs AoA between experiments and numerical simulation at $Re = 290e3$ for clean and tripped case 62
- Figure 65 NACA 0018 comparison of lift coefficient vs AoA for experiments and post-stall model at $Re = 115e3$ with $AR = 50$ for clean condition 66
- Figure 66 NACA 0018 comparison of lift coefficient vs AoA for experiments and post-stall model at $Re = 230e3$ with $AR = 50$ for clean condition 66
- Figure 67 NACA 0018 comparison of lift coefficient vs AoA for experiments and post-stall model at $Re = 290e3$ with $AR = 50$ for clean condition 67
- Figure 68 NACA 0018 comparison of lift coefficient vs AoA for experiments and post-stall model at $Re = 115e3$ with $AR = 10$ for clean condition 67

List of Figures

- Figure 69 NACA 0018 comparison of lift coefficient vs AoA for experiments and post-stall model at $Re = 230e3$ with $AR = 10$ for clean condition 68
- Figure 70 NACA 0018 comparison of lift coefficient vs AoA for experiments and post-stall model at $Re = 290e3$ with $AR = 10$ for clean condition 68
- Figure 71 NACA 0018 comparison of lift coefficient vs AoA for experiments and post-stall model at $Re = 115e3$ with $AR = 30$ for clean condition 69
- Figure 72 NACA 0018 comparison of lift coefficient vs AoA for experiments and post-stall model at $Re = 230e3$ with $AR = 30$ for clean condition 69
- Figure 73 NACA 0018 comparison of lift coefficient vs AoA for experiments and post-stall model at $Re = 290e3$ with $AR = 30$ for clean condition 70
- Figure 74 NACA 0018 comparison of drag coefficient vs AoA for experiments and post-stall model at $Re = 115e3$ with $AR = 50$ for clean condition 71
- Figure 75 NACA 0018 comparison of drag coefficient vs AoA for experiments and post-stall model at $Re = 230e3$ with $AR = 50$ for clean condition 72
- Figure 76 NACA 0018 comparison of drag coefficient vs AoA for experiments and post-stall model at $Re = 290e3$ with $AR = 50$ for clean condition 72
- Figure 77 NACA 0018 comparison of drag coefficient vs AoA for experiments and post-stall model at $Re = 115e3$ with $AR = 10$ for clean condition 73
- Figure 78 NACA 0018 comparison of drag coefficient vs AoA for experiments and post-stall model at $Re = 230e3$ with $AR = 10$ for clean condition 73
- Figure 79 NACA 0018 comparison of drag coefficient vs AoA for experiments and post-stall model at $Re = 290e3$ with $AR = 10$ for clean condition 74
- Figure 80 NACA 0018 comparison of drag coefficient vs AoA for experiments and post-stall model at $Re = 115e3$ with $AR = 30$ for clean condition 74
- Figure 81 NACA 0018 comparison of drag coefficient vs AoA for experiments and post-stall model at $Re = 230e3$ with $AR = 30$ for clean condition 75
- Figure 82 NACA 0018 comparison of drag coefficient vs AoA for experiments and post-stall model at $Re = 290e3$ with $AR = 30$ for clean condition 75
- Figure 83 NACA 0018 comparison of lift coefficient vs AoA for experiments and post-stall model at $Re = 115e3$ with $AR = 50$ for tripped condition 76
- Figure 84 NACA 0018 comparison of lift coefficient vs AoA for experiments and post-stall model at $Re = 230e3$ with $AR = 50$ for tripped condition 77

- Figure 85 NACA 0018 comparison of lift coefficient vs AoA for experiments and post-stall model at $Re = 290e3$ with $AR = 50$ for tripped condition 77
- Figure 86 NACA 0018 comparison of lift coefficient vs AoA for experiments and post-stall model at $Re = 115e3$ with $AR = 10$ for tripped condition 78
- Figure 87 NACA 0018 comparison of lift coefficient vs AoA for experiments and post-stall model at $Re = 230e3$ with $AR = 10$ for tripped condition 78
- Figure 88 NACA 0018 comparison of lift coefficient vs AoA for experiments and post-stall model at $Re = 290e3$ with $AR = 10$ for tripped condition 79
- Figure 89 NACA 0018 comparison of lift coefficient vs AoA for experiments and post-stall model at $Re = 115e3$ with $AR = 30$ for tripped condition 79
- Figure 90 NACA 0018 comparison of lift coefficient vs AoA for experiments and post-stall model at $Re = 230e3$ with $AR = 30$ for tripped condition 80
- Figure 91 NACA 0018 comparison of lift coefficient vs AoA for experiments and post-stall model at $Re = 290e3$ with $AR = 30$ for tripped condition 80
- Figure 92 NACA 0018 comparison of drag coefficient vs AoA for experiments and post-stall model at $Re = 115e3$ with $AR = 50$ for tripped condition 81
- Figure 93 NACA 0018 comparison of drag coefficient vs AoA for experiments and post-stall model at $Re = 230e3$ with $AR = 50$ for tripped condition 82
- Figure 94 NACA 0018 comparison of drag coefficient vs AoA for experiments and post-stall model at $Re = 290e3$ with $AR = 50$ for tripped condition 82
- Figure 95 NACA 0018 comparison of drag coefficient vs AoA for experiments and post-stall model at $Re = 115e3$ with $AR = 10$ for tripped condition 83
- Figure 96 NACA 0018 comparison of drag coefficient vs AoA for experiments and post-stall model at $Re = 230e3$ with $AR = 10$ for tripped condition 83
- Figure 97 NACA 0018 comparison of drag coefficient vs AoA for experiments and post-stall model at $Re = 290e3$ with $AR = 10$ for tripped condition 84
- Figure 98 NACA 0018 comparison of drag coefficient vs AoA for experiments and post-stall model at $Re = 115e3$ with $AR = 30$ for tripped condition 84
- Figure 99 NACA 0018 comparison of drag coefficient vs AoA for experiments and post-stall model at $Re = 230e3$ with $AR = 30$ for tripped condition 85
- Figure 100 NACA 0018 comparison of drag coefficient vs AoA for experiments and post-stall model at $Re = 290e3$ with $AR = 30$ for tripped condition 85

List of Figures

- Figure 101 NACA 0018 comparison with Delft experiments for lift coefficient 86
- Figure 102 NACA 0018 comparison with Delft experiments for drag coefficient 87
- Figure 103 NACA 0018 simulations compared to Delft experiments for lift coefficient 88
- Figure 104 NACA 0018 simulations compared to Delft experiments for drag coefficient: 89
- Figure 105 Open test section wind tunnel facility detail 90
- Figure 106 NACA 0015 airfoil at $Re = 209e3$ lift coefficient vs AoA from Rainbird experiments 91
- Figure 107 NACA 0015 airfoil at $Re = 209e3$ drag coefficient vs AoA from Rainbird experiments 92
- Figure 108 Blockage effects on NACA 0018 lift coefficient vs AoA for $Re = 230e3$ 92
- Figure 109 Blockage effects on NACA 0018 lift coefficient vs AoA detail in pre-stall and stall region for $Re = 230e3$ 93
- Figure 110 GT10 numerical lift coefficient vs AoA for clean case 94
- Figure 111 GT10 numerical drag coefficient vs AoA for clean case 95
- Figure 112 GT10 numerical aerodynamic efficiency coefficient vs AoA for clean case 96
- Figure 113 GT10 numerical aerodynamic efficiency coefficient vs AoA for clean case, a detail 96
- Figure 114 GT10 comparison of lift coefficient vs AoA for experiments and post-stall model at $Re = 290e3$ with $AR = 50$ for clean condition 97
- Figure 115 GT10 comparison of lift coefficient vs AoA for experiments and post-stall model at $Re = 290e3$ with $AR = 10$ for clean condition 98
- Figure 116 GT10 comparison of lift coefficient vs AoA for experiments and post-stall model at $Re = 115e3$ with $AR = 30$ for clean condition 98
- Figure 117 GT10 comparison of lift coefficient vs AoA for experiments and post-stall model at $Re = 230e3$ with $AR = 30$ for clean condition 99
- Figure 118 GT10 comparison of lift coefficient vs AoA for experiments and post-stall model at $Re = 290e3$ with $AR = 30$ for clean condition 99
- Figure 119 GT10 comparison of drag coefficient vs AoA for experiments and post-stall model at $Re = 290e3$ with $AR = 50$ for clean condition 100
- Figure 120 GT10 comparison of drag coefficient vs AoA for experiments and post-stall model at $Re = 290e3$ with $AR = 10$ for clean condition 100
- Figure 121 GT10 comparison of drag coefficient vs AoA for experiments and post-stall model at $Re = 115e3$ with $AR = 30$ for clean condition 101

- Figure 122 GT₁₀ comparison of drag coefficient vs AoA for experiments and post-stall model at $Re = 230e3$ with $AR = 30$ for clean condition 101
- Figure 123 GT₁₀ comparison of drag coefficient vs AoA for experiments and post-stall model at $Re = 290e3$ with $AR = 30$ for clean condition 102

LIST OF TABLES

Table 1	Trip parameters for experiments	12	
Table 2	Computational grid parameters.	13	
Table 3	Test section with additional wall experiments setting.	29	
Table 4	Trip parameters for experiments conducted in TU Delft[74, 77].	35	
Table 5	Computational parameters for DU-97-W-300 airfoil.	35	
Table 6	DU-97-W-300 synoptic table for aerodynamic characteristics	39	
Table 7	Estimated efficiency loss due to roughness effects for NACA 0018	46	
Table 8	Trip parameters for experiments conducted in University of Naples Federico II	50	
Table 9	Computational parameters for NACA 0018 airfoil	50	
Table 10	NACA 0018 synoptic table for aerodynamic characteristics	64	
Table 11	GT10 synoptic table for aerodynamic characteristics	95	
Table 12	Constants value for $k_T - k_L - \omega$ model.	108	

1

INTRODUCTION

A verification of the more common high angle of attack semi empirical models, i.e. Viterna-Corrigan and Aerodas from Spera, is needed to assess the input data reliability for Blade Element Momentum (BEM) based Vertical Axis Wind Turbine (VAWT) performance code and also the performance predictions for Horizontal Axis Wind Turbine (HAWT) where passive stall control must be guaranteed by a reliable post-stall aerodynamic coefficients distribution [71, 72]. In Figure 1 the normal operating condition for a small size VAWT is depicted so that the large angle of attack variation could be easily figured out. This is due to the great influence of the low Reynolds number related to the phenomenon (considering VAWT for urban installation and small size generation) and the presence of possible laminar bubble burst induced stall. In case for which no laminar bubble promotion is observed on the stall behavior, still a strong dependency on turbulence intensity is observed for the maximum lift coefficient attainable [14].

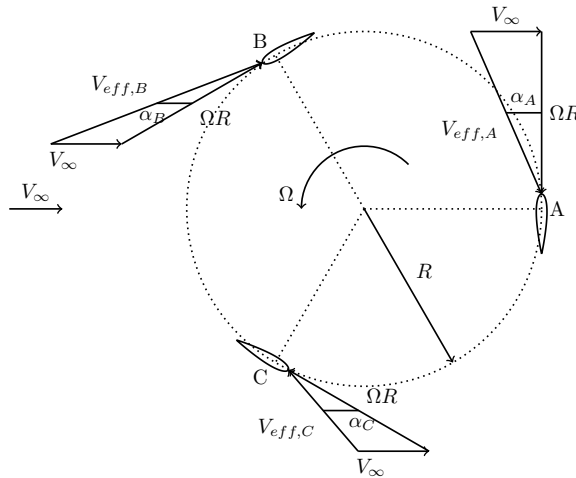


Figure 1: VAWT scheme for operating condition

Attention is also paid to not clean VAWT operating conditions as those occurring far from maintenance period in which a transition from laminar to turbulent flow regime could be supposed to be promoted by dirty material accumulation on the blade leading edge region. The needs of investigating low Reynolds number flow, such that the flow-field is mostly laminar or transitional, has lead us to take in consideration the use of a transition model. However, in this work a different transition model as been used, which is available in OpenFOAM library (starting from 2.1.0 release [43]), developed by Walters and Cokljat [83] and known as $k_T - k_L - \omega$ model, not very far from the model presented in the same year by Taghavi-Zenouz et al. [67]. The transition model used throughout

the simulations performed is the one developed by Walters and Cokljat [83] as implemented in OpenFOAM 2.1.0 library and further release. For so called two-equation models, two additional transport equations are solved to obtain the turbulence quantities used to compute the eddy viscosity. For example, a $k - \omega$ model form, which forms the basis for the used model, solves equations for the turbulent kinetic energy k_T and for the inverse time-scale ω (also interpreted as the specific dissipation rate). In this method, an additional transport equation is included in order to represent pre-transitional (i. e. non-turbulent) velocity fluctuations, namely a k_L equation for laminar fluctuation energy. We will refer in the following to a $k_T - k_L - \omega$ model. The numerical treatment of airfoil roughness is not been introduced in the turbulence modelling imposing somehow the transition onset (as it is possible with the codes XFOIL [17], MSES [18], RFOIL [74]), neither by switching to a fully turbulent model as the Spalart-Allmaras one [64, 3], instead by means of a mesh block directly representing the step-shape of a transition trip in 2D in a way similar to what has been done for stall strips by Zahle [85]. The first semi-empirical post-stall model is the one developed by Viterna and Corrigan [78, 79] correcting airfoil characteristics for use with blade element-momentum theory. The airfoil data below stall is corrected for the finite length of the blade. This approach appears to account for the induced effects better than classical blade element-momentum theory alone, particularly for highly loaded low aspect ratio blades, resulting in nearly constant power in high winds and showing good agreement with experimental data from several rotor configurations [44, 45, 46]. The second semi-empirical post-stall model is the AERODAS model [66] where an empirical approach is applied, in which the trends of test data are identified for a wide variety of airfoils and for the Unsteady Aerodynamics Experiment (UAE) wind turbine. These trends are then modelled by a set of algebraic equations based on the best fit of the model to available test data and not on aerodynamic theory. The lift and drag properties of infinite- and finite-length circular cylinders and thin plates are also modelled by these same empirical equations. Other semi empirical extrapolations were suggested besides these two, as the one of Sheldahl and Kilmas [59, 60], extensively discussed in other more recent works [52, 84], but they're not been considered because of the greater reliability assessed by some simulation codes (FAST [20], GH Bladed [22]) on the Viterna-Corrigan. The airfoil models are horizontally mounted and instrumented with staggered pressure ports on the midspan surface, while the force measurements are accomplished by force balance for lift and pitching moment. A double measurements system, composed by both force and pressure sensors has been adopted, thus having an integral description of lift coefficient avoiding the problem of local flow condition because of stall cells at high angle of attack, while keep tracking via the pressure taps on the body the pressure coefficient C_p chord-wise distribution describing the laminar bubble position and importance, and finally capturing the drag coefficient value in post-stall region.

As aforementioned the direct application of this study focuses on the good description of wind turbine behaviour in off-design operating condition, as for HAWT, and starting condition, as for VAWT that would normally experience low starting performance due to stalled condition in which operate the blades. Conversely, the HAWT will reliably self start at low wind speeds, and produce a useful output at average Italy wind speeds (around 4 m/s for most of the country, can be up to 7 m/s on higher ground in the south and on the islands Sicily

and Sardinia) even though this value is below rated speeds for most designs [76]. Certainly for a large turbine intended for use in a wind farm, a HAWT would be the most sensible choice, but for smaller installations, VAWTs have several advantages [7]. Thanks to their vertical axis, heavy generation equipment can be located on the ground. Impossible without gearing on a HAWT, which reduces efficiency and increases the likelihood of a breakdown, this is desirable as it not only reduces the strength required in the supporting mast, but also eases the maintenance process considerably; it negates the need to climb to a nacelle mounted generator [24]. The installation process is also simplified, the generator being the heaviest single component. Yaw mechanisms are another component which are acceptable on larger turbines where they can easily be actively controlled, but on smaller examples passive, wind-vane style controls would be used, which are aerodynamically damaging to the flow through the blades. Whether active or passive, the mechanisms can be unresponsive in sudden changes of flow direction, common in flow around buildings; if they hold the turbine only a few degrees out of optimum position loss of efficiency can be considerable [5]. Since VAWTs have no need for yawing, accepting as they do wind from any direction, these problems are avoided. VAWTs are usually mounted in the slower, less laminar air movements close to ground level, unlike loftier HAWTs. Uneven landscapes and other obstacles, such as housing and trees, are to blame for these flow conditions. Low mounting is often presented as a disadvantage when compared to HAWTs, but it makes VAWTs ideal for rooftop mounting in an urban environment. Since λ values are lower than HAWTs, they create less aerodynamic noise too, another important consideration when mounting to buildings [47]. A critical issue of VAWT lies in the cyclical nature of the wind loading on individual blades and supports could be very damaging over time; loading on HAWT blades is constant throughout rotation. There may also be problems with aerodynamic efficiency compared to that of HAWTs - modern examples of which achieve figures of 42%, though previous studies have found values to be similar. By far the biggest hindrance to VAWTs is their starting problems. Though motion is induced well enough even in light breezes, in winds with speeds below their rated value λ values are poor; HAWTs produce useful outputs for speeds well below that at which they are rated.

In Figure 2 both a micro VAWT for house roof installation¹ and a 60 kW HAWT² are shown: for the latter case the author has been since his Master's Thesis project in the aerodynamic design of the blade[12]. Good characteristics for micro-generation installations are of particular importance in Italy, thanks to the implemented government policy. In the past, renewable energy installations have usually been large, public ventures; now the government is looking to individuals and businesses to make up some of the country's electricity needs through smaller schemes with the "Tariffa Fissa Omnicomprensiva" (or "Tariffa Omnicomprensiva", TO), that limits to 200 kW the plants size to be fed with incentives for a maximum of 15 years [49, 51, 29].

A far greater general interest for renewable energy and environment friendly technology has been fed during the research period as demonstrated by other collateral research conducted concerning morphing winglet for pollution reduction in commercial aircraft transportation [15], and moreover a certain knowledge of

¹ <http://www.cleanenergywisconsin.com/wind.php>

² <http://www.eolart.it/it/installazioni.aspx?l=it#>



(a) Micro VAWT for house installation



(b) EOL-CK-60

Figure 2: VAWT and HAWT of size compatible for incentive feeding

optimization procedure has been achieved in the meanwhile [9, 10, 11] giving some good perspective for an integrated design for both HAWT and VAWT that would be based on reliable post-stall data with some chance of further development in dedicated airfoil design as illustrated in [8].

This thesis is articulated as follows: in Chapter 2 the numerical, semi-empirical and experimental methodology is illustrated, in Chapter 3 the results from both experiments, post-stall model application and CFD analysis are presented and finally in Chapter 4 the conclusions are summarized.

2 | METHOD

2.1 NUMERICAL METHODOLOGY

The needs of investigating low Reynolds number flow, such that the flow-field is mostly laminar or transitional, has lead us to take in consideration the use of a transition model.

Even if with the S-A and $k-\omega$ SST models it is not possible to predict the transition point to agree with the real physical transition, some recommendations for free stream turbulence levels have been made [55, 65]. Such suggestions were not based upon matching free stream turbulence levels from wind tunnel or flight, but rather upon considerations related to preserving potential cores and maintaining the integrity of the turbulence quantities throughout the boundary layers .

The author has investigated the possibility to achieve a fair agreement between the S-A and $k-\omega$ SST turbulence methods acting on *Turbulence Intensity* for $k-\omega$ SST for the free stream boundary condition. In [13] the Spalart Allmaras method [64] in its standard form has been used for the calculations shown in this work, modifying the turbulence Intensity to very low values, such that a bubble formation, separation and transition to turbulence flow condition could be observed. The turbulence intensity values used in the approach of Menter [41, 31] are related strictly to the one foreseeable in wind tunnel testing. This method of predicting transition is based upon experimental correlations that usually relate the free-stream turbulence intensity and the local pressure gradient to the transition momentum thickness Reynolds number, defined as $Re_\theta = \rho\theta U_0/\mu$, where θ is the momentum thickness and U_0 the local free stream velocity. Such task is even more complicated in modern CFD methods based on non structured grid (used to approximate complex geometries) and parallel calculation, in which the information must be shared on different machine, since the integration of boundary layer parameters would result very difficult.

As detailed in [42, 30], the transition model is based on two transport equations: a transport equation for intermittency, used to trigger transition locally; and a second transport equation that computes the transition onset momentum-thickness Reynolds number. The essential part of the model lies in the second transport equation that links the empirical correlation to the onset criteria in the intermittency equation, coupled with SST $k-\omega$ model of Menter [40]. This model is known as $\gamma - Re_\theta$ transition model.

However, in this work a different transition model as been used, which is available in OpenFOAM library (starting from 2.1.0 release [43]), developed by Walters and Cokljat [83] and known as $k_T - k_L - \omega$ model, not very far from the model presented in the same year by Taghavi-Zenouz et al. [67].

2.1.1 $k_T - k_L - \omega$ transition model

The transition model used throughout the simulations performed is the one developed by Walters and Cokljat [83] as implemented in OpenFOAM 2.1.0 library and further release. For so called two-equation models, two additional transport equations are solved to obtain the turbulence quantities used to compute the eddy viscosity. For example, a $k - \omega$ model form, which forms the basis for the used model, solves equations for the turbulent kinetic energy k_T and for the inverse time-scale ω (also interpreted as the specific dissipation rate). In this method, an additional transport equation is included in order to represent pre-transitional (i.e., non-turbulent) velocity fluctuations, namely a k_L equation for laminar fluctuation energy. We will refer in the following to a $k_T - k_L - \omega$ model. Some more words on transition-sensitive modelling concept. The pre-transitional boundary layer is effectively laminar in terms of the mean velocity profile. For free stream turbulence intensities less than about 1%, the development of low amplitude pre-transitional velocity fluctuations is dominated by self sustained instability mechanisms, namely Tollmien-Schlichting waves [57]. As free stream turbulence intensity (Tu_∞) increases, the mean velocity in the pre-transitional boundary layer becomes noticeably distorted from the typical Blasius profile, with an increase in momentum in the inner region and a decrease in the outer, even for Tu_∞ as low as about 1% [37]. This shift in mean velocity profile is accompanied by the development of relatively high-amplitude stream-wise fluctuations, which can reach intensities several times the free stream level [28]. This process results in an augmentation of skin friction and heat transfer in the pre-transitional region, and eventually leads to transition through the breakdown of the stream-wise fluctuations. This process is known as bypass transition. The pre-transitional fluctuations leading to bypass transition are due to the presence of low frequency / low amplitude stream-wise vortices in the boundary layer, and appear as “streaky structures” in flow visualizations, direct numerical simulations [27], and large-eddy simulations [32].

Since the total fluctuation energy in the model is comprised of the sum of k_L and k_T , the transfer of energy from one to another is appropriately interpreted as energy redistribution rather than production due to interaction with the mean flow or dissipation due to viscous mechanisms. It is proposed that the relevant dimensionless quantity responsible for transition inception is the ratio between the turbulent production time-scale and the molecular diffusion time-scale. The onset of transition is therefore assumed to occur when the time-scale ratio reaches a critical value. The natural transition criterion is therefore a function of the ratio of the Tollmien-Schlichting time-scale to the molecular diffusion time-scale. These two dimensionless parameters are used to develop the transition-sensitive damping functions for the turbulence production term in the model equations.

Model equations

Here are introduced the model equations focusing on incompressible single-phase flow with no body forces, governed by the steady Reynolds-averaged con-

tinuity and momentum equations, and a linear eddy-viscosity model is adopted for the Reynolds stresses

$$\rho \overline{u_i u_j} - \frac{1}{3} \overline{u_k u_k} \delta_{ij} = \mu_T S_{ij}. \quad (2.1)$$

Three additional model transport equations are solved for the turbulent kinetic energy k_T , the laminar kinetic energy k_L , and the scale-determining variable ω , defined here as $\omega = \varepsilon/k_T$, where ε is the isotropic dissipation. The transport equations are:

$$\begin{aligned} \frac{Dk_T}{Dt} &= P_{k_T} + R_{BP} + R_{NAT} - \omega k_t - D_T \\ &\quad \frac{\partial}{\partial x_j} \left[\left(\nu + \frac{\alpha_T}{\sigma_k} \right) \frac{\partial k_T}{\partial x_j} \right] \end{aligned} \quad (2.2)$$

$$\frac{Dk_L}{Dt} = P_{k_L} + R_{BP} + R_{NAT} - D_L + \frac{\partial}{\partial x_j} \left[\nu \frac{\partial k_L}{\partial x_j} \right] \quad (2.3)$$

$$\begin{aligned} \frac{D\omega}{Dt} &= C_{\omega 1} \frac{\omega}{k_T} P_{k_T} + \left(\frac{C_{\omega R}}{f_W} - 1 \right) \frac{\omega}{k_T} (R_{BP} + R_{NAT}) \\ &\quad - C_{\omega 2} \omega^2 + C_{\omega 3} f_{\omega} \alpha_T f_W^2 \frac{\sqrt{k_T}}{d^3} + \frac{\partial}{\partial x_j} \left[\left(\nu + \frac{\alpha_T}{\sigma_{\omega}} \right) \frac{\partial \omega}{\partial x_j} \right]. \end{aligned} \quad (2.4)$$

In the ω equation, the fully turbulent production, destruction, and gradient transport terms (first, third, and fifth terms on the right-hand side of Eq. 2.4) are analogous to the similar terms in the k_T and k_L equations and are similar to terms that appear in other $k - \omega$ model forms. The transition production term (second term on right-hand side) is intended to produce a reduction in turbulence length scale during the transition breakdown process. More details on this model are presented in Appendix A.

Boundary conditions at body

The boundary conditions for the three equation model are similar to those for more commonly used $k - \omega$ and $k - \varepsilon$ models. At solid boundaries, the no-slip condition enforces

$$k_T = k_L = 0. \quad (2.5)$$

A zero-normal-gradient condition is used for ω

$$\frac{\partial \omega}{\partial \eta} = 0, \quad (2.6)$$

where η is the wall-normal coordinate direction. Note that the wall boundary condition (Equation 2.6) is substantially different from that commonly used in other $k - \omega$ model forms. The reason for this is that, in most other models, the value of ω must increase in the viscous sublayer to model the increased level of dissipation near the wall and to ensure asymptotically correct behavior of the

model in the near-wall region. The current model adopts an alternative approach similar to many low-Re $k - \omega$ models, in which the increased viscous dissipation in the sublayer is incorporated into the k_L and k_T equations through a viscous wall destruction term (Eq.s A.22,A.23). The product ωk_T therefore represents a scalar isotropic dissipation [82], which approaches zero with $O(\eta^2)$ as the wall distance approaches zero. Viscous destruction in the k_T and k_L equations near the wall is therefore dominated by the wall destruction terms.

Boundary conditions at inflow

At flow inlets, the values of k_T and ω are prescribed exactly analogous to other two-equation models. The turbulent kinetic energy is often determined based on the inlet turbulence intensity Tu_∞ , assuming isotropic free stream turbulence:

$$Tu_\infty = \frac{\sqrt{\frac{2}{3}k_T}}{U_\infty}. \quad (2.7)$$

The value of the specific dissipation is chosen to coincide with the available free stream information. For example, if the turbulent length scale or the decay rate is known, ω may be chosen to reproduce the appropriate free stream conditions. For velocity inlets sufficiently far from solid walls, the inlet flow may be considered to be completely outside the boundary layer. In that case, the laminar kinetic energy associated with pretransitional fluctuations is zero. The appropriate inlet boundary condition is therefore $k_L = 0$, and this condition was used for all of the simulations performed.

Particular care is given to the turbulence quantities settings for the inlet boundary as pointed out by Spalart [65]. In order to achieve a turbulence intensity comparable with that of the experiments, the free decayment of the turbulence quantities from the inlet to the airfoil should be taken into account. In the following we denote with k , ε and \mathcal{P} respectively the turbulent kinetic energy, the turbulent dissipation and the turbulent kinetic energy production, while the model constants are $C_{\varepsilon 1}$, $C_{\varepsilon 2}$, σ_k , and σ_ε . We will achieve the kinematic viscosity information from the turbulent kinetic energy and the turbulent dissipation values. Considering the solution of $k - \varepsilon$ equations

$$\frac{Dk}{Dt} = \mathcal{P} - \varepsilon + \frac{\partial}{\partial x_j} \left[\left(\nu + \frac{\nu_t}{\sigma_k} \right) \frac{\partial k}{\partial x_j} \right], \quad (2.8)$$

$$\frac{D\varepsilon}{Dt} = \frac{\varepsilon}{k} (C_{\varepsilon 1} \mathcal{P} - C_{\varepsilon 2} \varepsilon) + \frac{\partial}{\partial x_j} \left[\left(\nu + \frac{\nu_t}{\sigma_\varepsilon} \right) \frac{\partial \varepsilon}{\partial x_j} \right], \quad (2.9)$$

and assuming that when approaching the body only the destruction terms are active (approximating as $Uk_x = -\varepsilon$ and $U\varepsilon_x = -C_{\varepsilon 2}\varepsilon^2/k$), one get the solution

$$\frac{k}{\varepsilon} = \left(\frac{k}{\varepsilon} \right)_I + (C_{\varepsilon 2} - 1) \frac{x}{U_\infty}, \quad (2.10)$$

where the suffix I stands for ‘‘inflow’’, x is the distance from the inflow boundary and the body and U_∞ the inflow velocity. The solution for the turbulent quantities are

$$k = k_I \left[1 + (C_{\varepsilon 2} - 1) \left(\frac{\varepsilon}{k} \right)_I \frac{\chi}{U_\infty} \right]^{\frac{-1}{C_{\varepsilon 2} - 1}}, \quad (2.11)$$

$$\varepsilon = \varepsilon_I \left[1 + (C_{\varepsilon 2} - 1) \left(\frac{\varepsilon}{k} \right)_I \frac{\chi}{U_\infty} \right]^{\frac{-C_{\varepsilon 2}}{C_{\varepsilon 2} - 1}}, \quad (2.12)$$

$$\nu_t = \nu_{tI} \left[1 + (C_{\varepsilon 2} - 1) \left(\frac{\varepsilon}{k} \right)_I \frac{\chi}{U_\infty} \right]^{\frac{C_{\varepsilon 2} - 2}{C_{\varepsilon 2} - 1}}, \quad (2.13)$$

from which one can find the modified turbulent viscosity at the inlet using the S–A model relation [64]:

$$\tilde{\nu}_t = \frac{\nu_t}{f_{\nu 1}}, \quad (2.14)$$

$$f_{\nu 1} = \frac{\chi^3}{\chi^3 + C_{\nu 1}^3}, \quad (2.15)$$

where, assuming what suggested in [65], $\chi = 3$, $C_{\nu 1} = 3.2$ so that $f_{\nu 1} \simeq 0.4517$.

In this case, the turbulence intensity is significantly higher than the values analysed by Spalart [65], so we have considered the Eq. 2.7 to obtain a turbulent kinetic energy value. Furthermore, this relationship

$$\varepsilon = C_\mu^{\frac{3}{4}} k_{exp}^{\frac{3}{2}} / c, \quad (2.16)$$

where $C_\mu = 0.09$ and c is the airfoil chord, was used for determining the turbulent dissipation, in order to use the system of Equations 2.11–2.13 to find the *inlet* value for the turbulent viscosity. The turbulent viscosity from experiments is related to kinetic energy and dissipation as

$$\nu_{t,exp} = C_\mu \frac{k_{exp}^2}{\varepsilon_{exp}}, \quad (2.17)$$

Figure 3 helps to understand the procedure involved in estimating from experiments the proper values for turbulent quantities to be set on inflow boundary. Using Eq.s 2.7, 2.16, 2.17 one could compute the boundary values to solve the system of Eq.s 2.11–2.13 to establish the correct turbulent quantities at the inflow boundary of the computational domain.

The author in [14] has tested this method comparing it with an experiment for which three turbulent inflow conditions are generated via three different rectangular grids installed on the nozzle of the wind tunnel with grids width of 25 mm (case A), 50 mm (B) and 100 mm (C) [58]. The turbulence intensity is defined as

$$Ti = \frac{\sigma_u}{\bar{u}}, \quad (2.18)$$

where \bar{u} is the mean wind speed and σ_u the standard deviation.

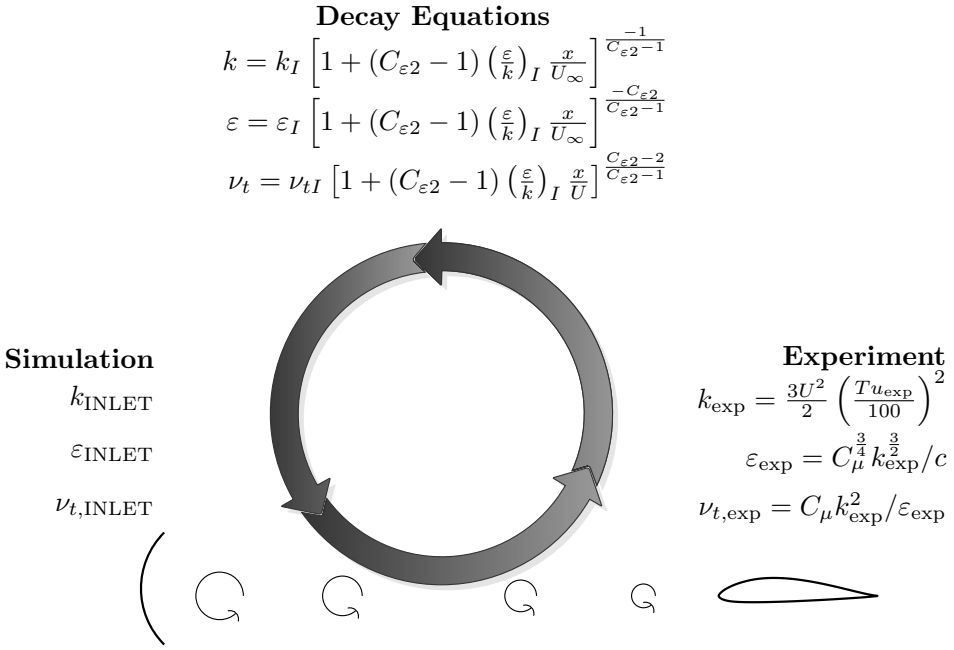


Figure 3: Decay law application

A comparison of the modified turbulent viscosity decay between the theoretical model and the numerical result has been performed. The modified turbulent viscosity in the flow-field has been normalized with its value at the body $\tilde{\nu}_{t,\text{exp}}$ derived from the turbulence intensity that was experimentally measured. Its value for the different grids is respectively equal to 0.34 (A), 0.56 (B) and 1.05 m²/s (C). This procedure is adopted for the theoretical model and for the numerical result. Figures 4 and 5 show the turbulent viscosity decaying with and without the presence of the body.

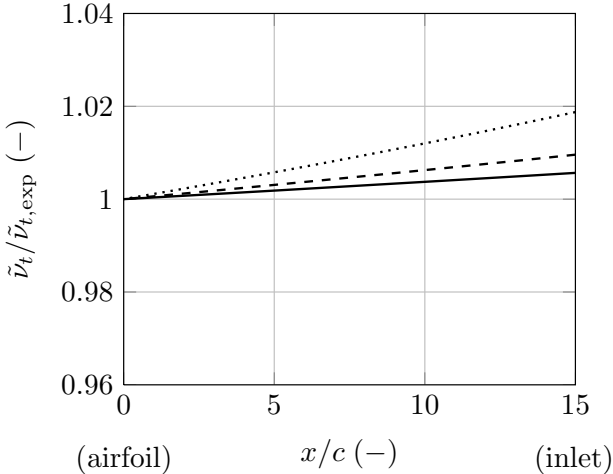


Figure 4: Theoretical decay: —Theory (A), - -Theory (B), ... Theory (C)

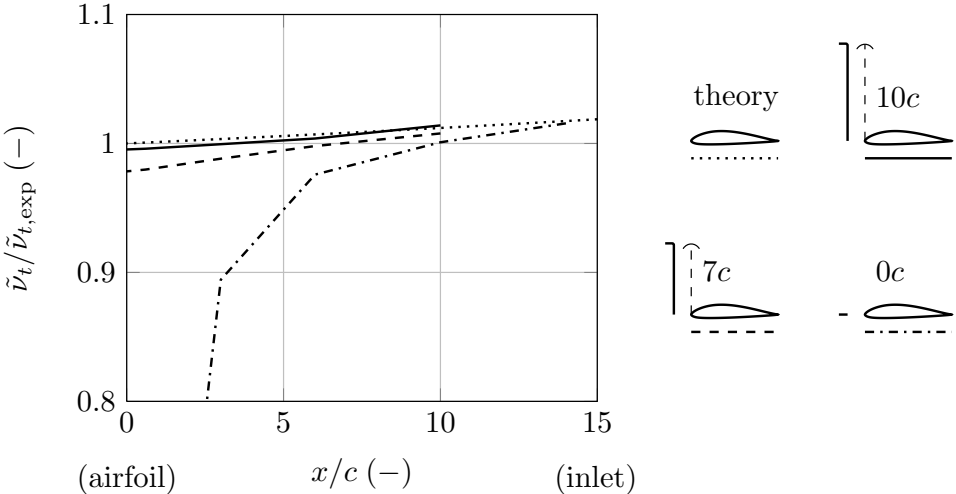


Figure 5: Theoretical vs. numerical decay for $\text{Ti} = 3.6\%$

2.1.2 Roughness sensitivity

A study on roughness sensitivity has also been performed. The standard roughness (also called sand roughness) is defined for a whole surface covered with a layer of spheres packed together as dense as possible. The diameter of these spheres is then called sand roughness height k_s [57]. In our case the roughness is introduced nor by sand neither by dust [54], instead via transition trip [62, 63] collocated in such a chordwise position to avoid laminar bubble formation at first computed with XFOIL then verified with oil visualization. The effect of transition trip results in alleviation of laminar bubble-induced unsteadiness on the airfoil [38] and bubble-induced separation prior to a laminar-to-turbulent transition [53, 2, 86].

The numerical treatment of airfoil roughness is not been introduced in the turbulence modelling imposing somehow the transition onset (as it is possible with the codes XFOIL [17], MSES [18], RFOIL [74]), neither by switching to a fully turbulent model as the Spalart-Allmaras one [64, 3], instead by means of a mesh block directly representing the step-shape of a transition trip in 2D in a way similar to what has been done for stall strips by Zahle [85].

In Figure 6 is sketched the trip used in experiments, with indication of major geometric parameters that are specified for each airfoil analysed in Table 1. Trip configuration is close to what arranged in [74, 77] dealing with several airfoils among which the DU-97-W-300 used here as a test case (see Figure 7 for airfoil geometry).

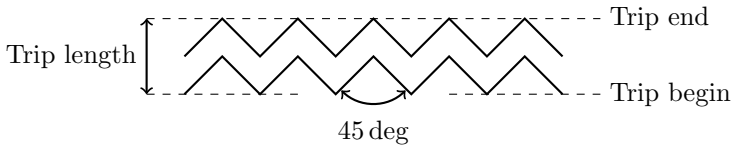


Figure 6: Trip schematization with major parameters indication

Airfoil	Trip begin	Trip length	Trip height
NACA 0018	0.1 %c	6.7 %c	0.25 mm
DU-97-W-300	5.0 %c	1.7 %c	0.35 mm

Table 1: Trip parameters for experiments

In Figure 8 are shown detailed view of numerical grid generated by *blockMesh* tool for all the analysed airfoils with the same parameters summarised in Table 1.

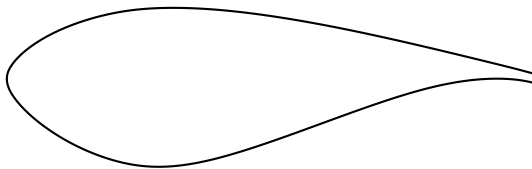


Figure 7: DU-97-W-300 airfoil geometry

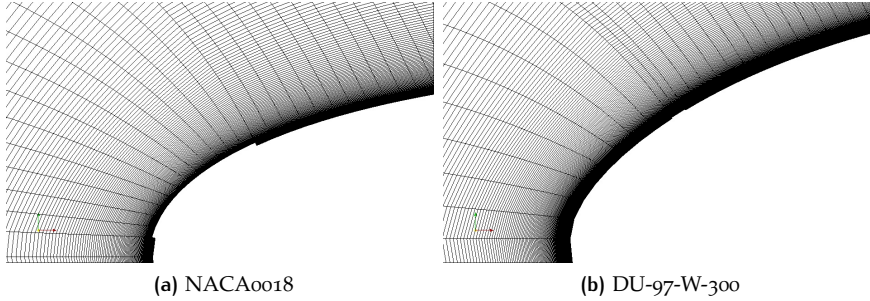


Figure 8: Trip detail in numerical grid

2.1.3 Simulations set-up

In this subsection are summarized the settings for all the simulations performed. Both NACA0018 and GT10 airfoils are analysed for three Reynolds numbers between $1e^5$ and $3e^5$ while the reference airfoil for the test case DU-97-W-300 has been analysed at a Reynolds number of $3e^6$ for comparison with experimental data in [74, 77]. Turbulence at inlet is imposed such to realize at the airfoil test condition, i.e. for all the airfoils a value of about 0.1%. The extensions of the rectangular computational domain are in all cases proportional to chord length and equal to 15 chords in all direction starting from the airfoil aerodynamic centre located at a quarter chord. The inner portion of the domain, close to the airfoil has a circular shape in order to use the same topology varying the angle of attack via body rotation, instead of modifying velocity components on boundary. No interface is present cause the two grid portion are merged together within *blockMesh*. Computational grid sizes for each case, in terms of cell number, have been established after separate sensitivity analyse on aerodynamic coefficients, keeping the y^+ value around 1: the values are summarised in Table 2.

Airfoil	Cells	Re	y^+
NACA 0018	$107e^3$	$115 \dots 290e3$	~ 1
NACA 0018 (trip)	$86e^3$	$115 \dots 290e3$	~ 1
GT10	$107e^3$	$115 \dots 290e3$	~ 1
DU-97-W-300	$82e3$	$3e6$	~ 1
DU-97-W-300 (trip)	$125e3$	$3e6$	~ 1

Table 2: Computational grid parameters.

The choice of the top-to-bottom dimension H , here equal to 30 chords, is related to avoid the blockage effects of the wind tunnel walls that also in the numerical simulations would affect the lift and drag coefficient values, especially and respectively, at the onset of the secondary peak around 45 degrees and at the maximum value around 90 degrees. In Figure 9 and 10, respectively, the lift and drag coefficient vs angle of attack are shown: with the continuous line the case with top and bottom wall such that $H/c = 5$ is indicated, showing both a higher peak for lift coefficient post-stall and maximum drag coefficient; with the dashed line the case with $H/c = 5$ corrected for blockage effects (see subsection 2.3.1) is

indicated, clearly exhibit a fairly good agreement with the simulation for which $H/c = \infty$ (i.e. no top and bottom wall present) indicated by the dotted line. This situation exploits the good approximation of a *open test section* simulation (i.e. $H/c = \infty$, no walls) with respect to a more realistic *closed test section* simulation (i.e. $H/c = 5$) corrected for blockage effects, that is in contrast with what stated by Worasinchai [84] (see a more detailed discussion in subsection), even if the maximum drag coefficient has a maximum value quite different from that prescribed by flat plate (see Equation 2.35 on 21) theory and several experiments.

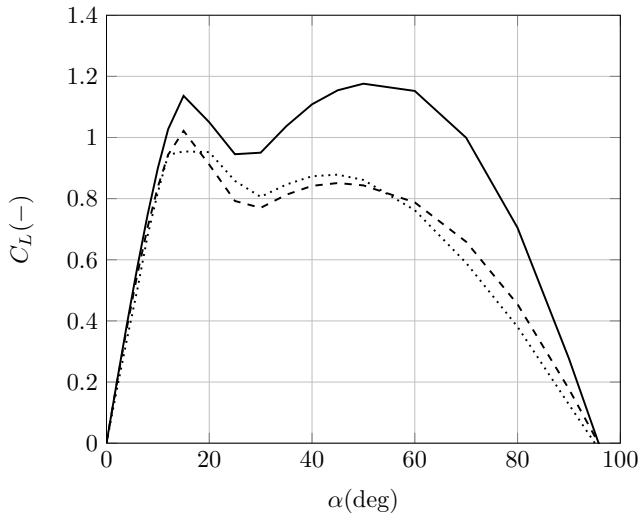


Figure 9: Blockage effect on lift coefficient: — $H/c = 5$, - - H/c corrected, \cdots $H/c = \infty$

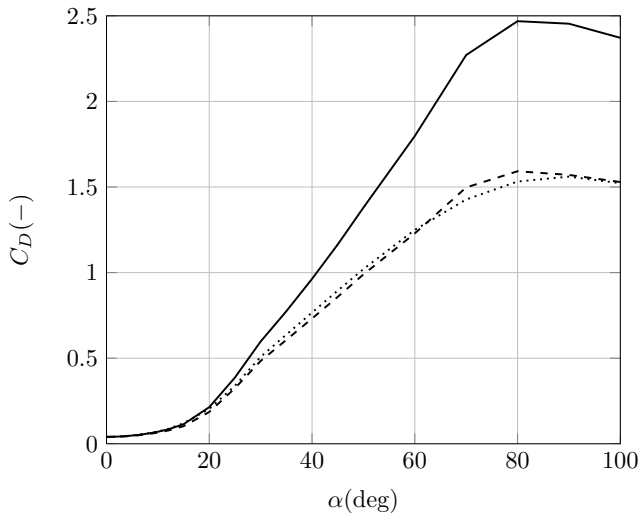
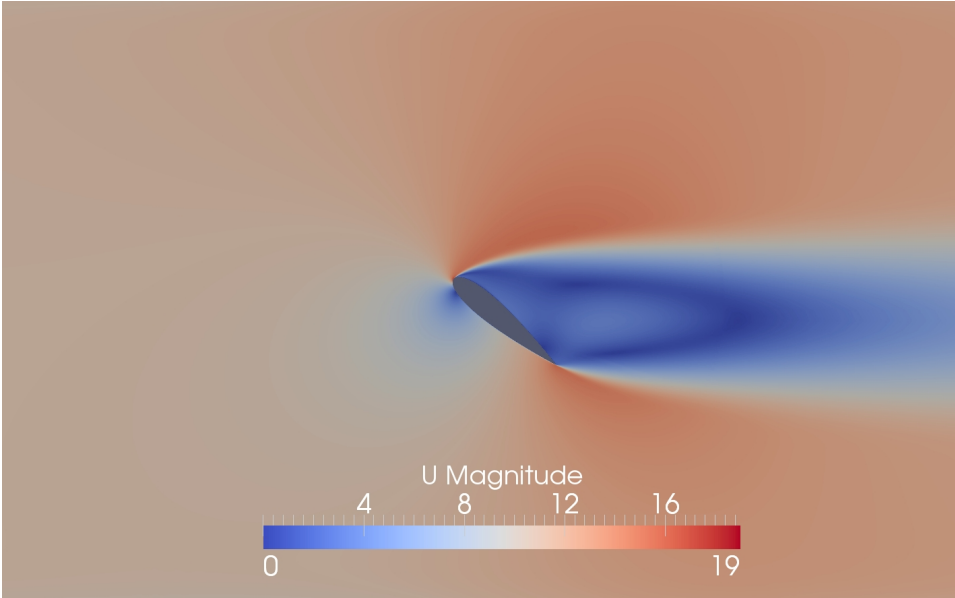
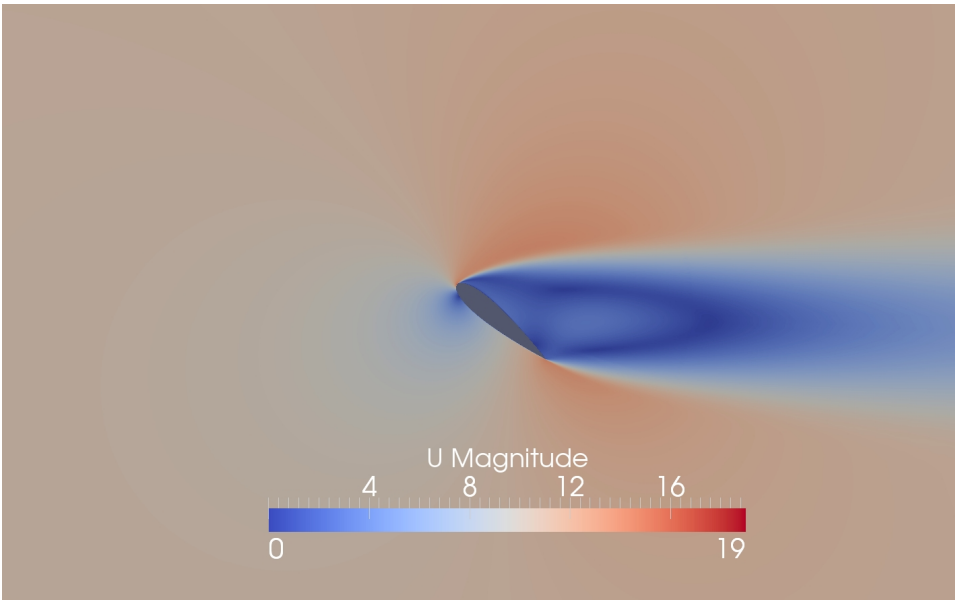


Figure 10: Blockage effect on drag coefficient: — $H/c = 5$, - - H/c corrected, \cdots $H/c = \infty$

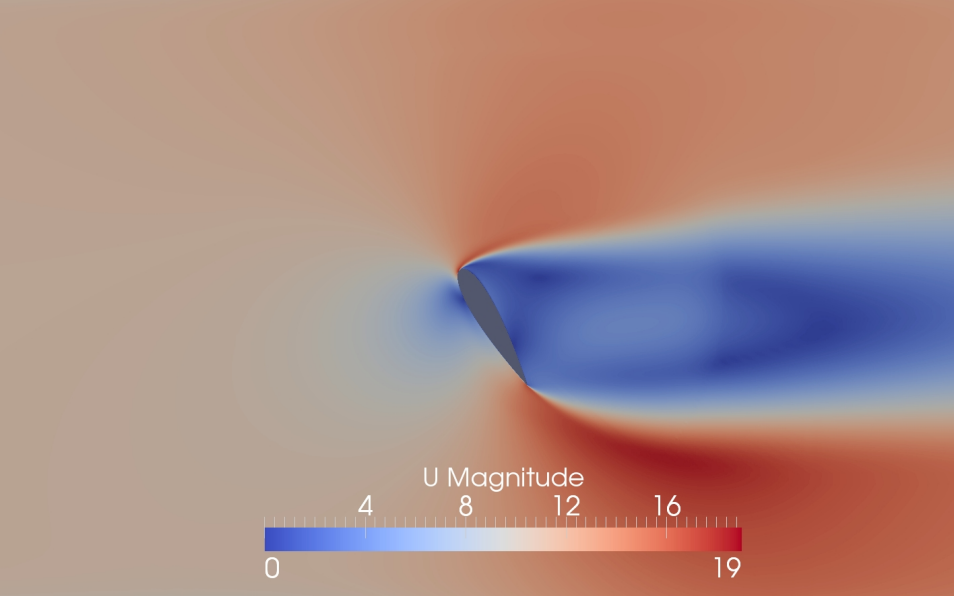


(a) $H/c = 5$

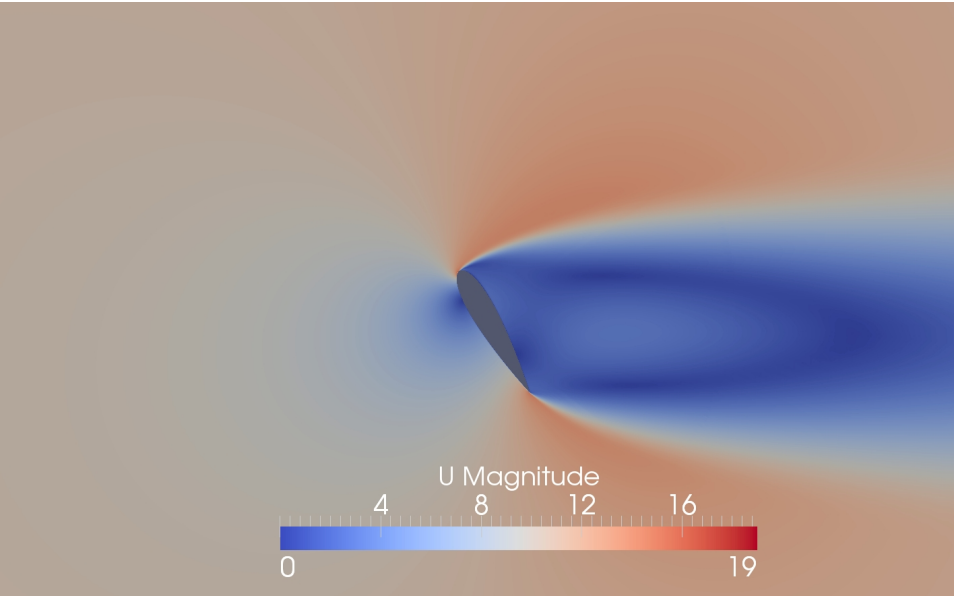


(b) $H/c = \infty$

Figure 11: Blockage effect on velocity field at 40 degrees for $H/c = 5$ and $H/c = \infty$

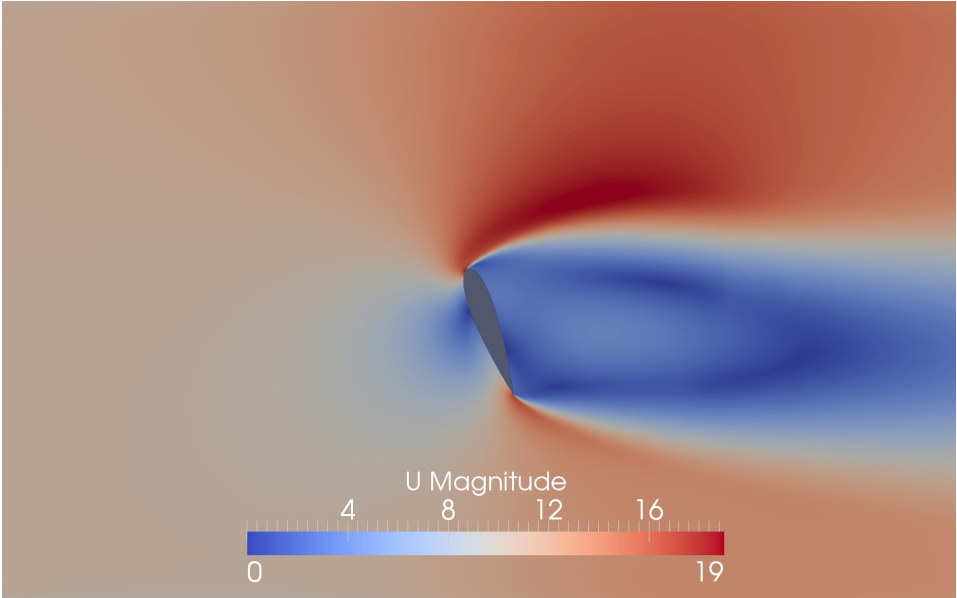


(a) $H/c = 5$

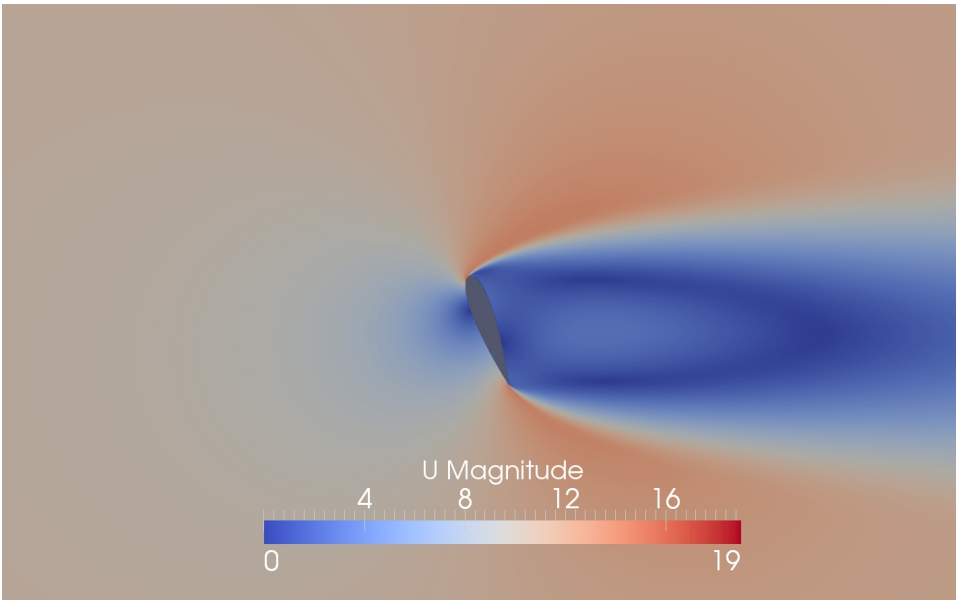


(b) $H/c = \infty$

Figure 12: Blockage effect on velocity field at 60 degrees for $H/c = 5$ and $H/c = \infty$

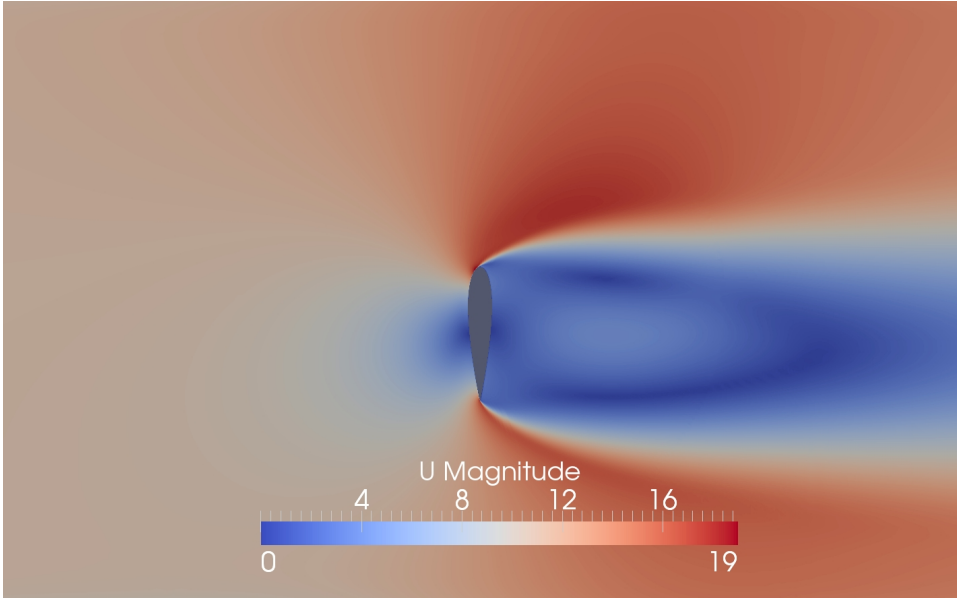


(a) $H/c = 5$

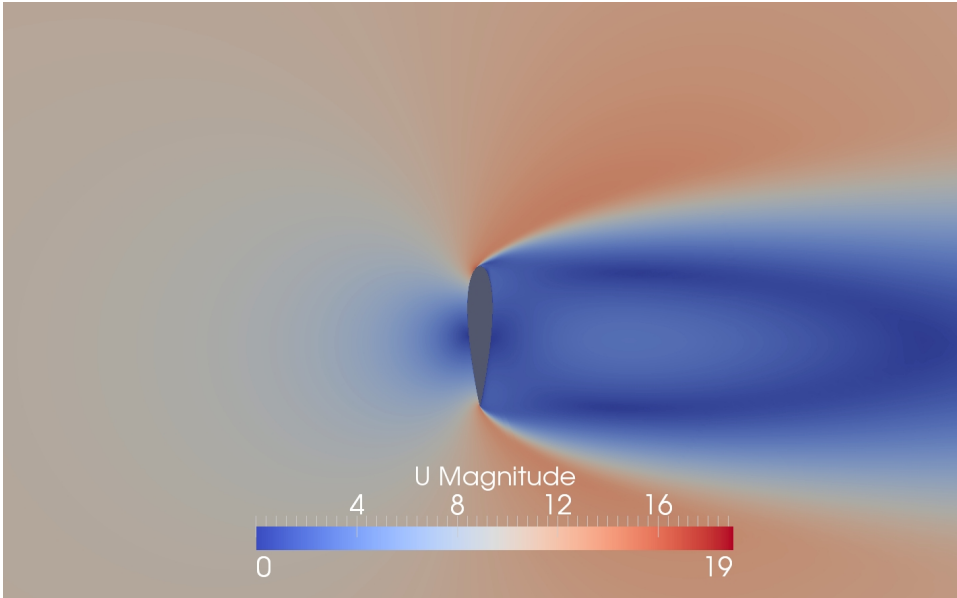


(b) $H/c = \infty$

Figure 13: Blockage effect on velocity field at 70 degrees for $H/c = 5$ and $H/c = \infty$



(a) $H/c = 5$



(b) $H/c = \infty$

Figure 14: Blockage effect on velocity field at 90 degrees for $H/c = 5$ and $H/c = \infty$

2.2 SEMI-EMPIRICAL MODELS

In this section two different semi-empirical model are introduced. Both try to describe the high angle of attack aerodynamic characteristics for airfoil used on wind turbines. The Viterna-Corrigan is first illustrated as it in 1982 original paper was formulated, and then the Aerodas method developed by Spera more recently (2008) is described. Other semi empirical extrapolations were suggested besides these two, as the one of Sheldahl and Kilmas [59, 60], extensively discussed in other more recent works [52, 84], but they're not been considered because of the greater reliability assessed by some simulation codes (FAST [20], GH Bladed [22]) on the Viterna-Corrigan. Both semi-empirical proposals are firmly based on the early results of experiments performed on flat plate that seem to be not in good agreement with what can be achieved through numerical simulations, at least in two-dimensional case [39, 68, 69].

2.2.1 Viterna-Corrigan

In the work of Viterna and Corrigan [78, 79] a method of correcting airfoil characteristics for use with blade element-momentum theory has been developed. The airfoil data below stall is corrected for the finite length of the blade. This approach appears to account for the induced effects better than classical blade element-momentum theory alone, particularly for highly loaded low aspect ratio blades. An idealized model for aerodynamic characteristics after stall has been developed which results in nearly constant power in high winds. This model shows good agreement with experimental data from several rotor configurations [44, 45, 46].

Viterna assumes the following expressions for the torque coefficient and torque

$$C_Q = C_L \sin(\alpha) - C_D \cos(\alpha), \quad (2.19)$$

$$Q \sim C_Q V_R^2, \quad (2.20)$$

where C_L, C_D are, respectively, the lift and drag coefficient, α the angle of attack and V_R the resultant speed that the blade section (i.e. the airfoil) sees while rotating. For a constant rotor speed, V_Ω , it can also be stated that

$$Q \sim C_Q \frac{V_R^2}{V_\Omega}, \quad (2.21)$$

so that for chord line parallel to plane of rotation it holds

$$Q \sim \frac{C_Q}{\cos(\alpha)^2}, \quad (2.22)$$

and substituting the Equation 2.19 in it one obtains:

$$Q \sim \frac{C_L \cos(\alpha)}{\cos(\alpha)^2} - \frac{C_D}{\cos(\alpha)}. \quad (2.23)$$

The post-stall behavior is described with the following equations:

$$C_{L,VC} = A_1 \sin(2\alpha) + A_2 \frac{\cos(\alpha)^2}{\sin(\alpha)}, \quad (2.24)$$

$$C_{D,VC} = B_1 \sin(\alpha)^2 + B_2 \cos(\alpha), \quad (2.25)$$

that substituted into Eq. 2.23 give:

$$Q \sim (2A_1 - B_1) \sin(\alpha) \tan(\alpha) + (A_2 + B_2). \quad (2.26)$$

Eq.s 2.24 describes lift coefficient with maximum value at 45 deg and null value at 90 deg, while 2.25 prescribes a bell shaped drag coefficient with angle of attack with maximum value at 90 deg; both these equations hold strictly for flat plate but give only reasonable values for airfoils. Since the measured torque after stall is independent of wind speed it should be independent also of angle of attack, taking the derivative with respect to α provides the expressions for the first pair of model constants as

$$B_1 = C_{D,max}, \quad (2.27)$$

$$A_1 = \frac{B_1}{2} = \frac{C_{D,max}}{2}, \quad (2.28)$$

where the maximum drag coefficient is computed with the following expression based on experimental data for $AR \leq 50$ [25]:

$$C_{D,max} = 1.11 + 0.018 \cdot AR. \quad (2.29)$$

Rearranging Eq.s 2.24 and 2.25 and substituting back into them, respectively, Eq. 2.28 and 2.27, the second pair of model constants is obtained:

$$A_2 = (C_L - C_{D,max} \sin(\alpha) \cos(\alpha)) \frac{\sin(\alpha)}{\cos(\alpha)^2}, \quad (2.30)$$

$$B_2 = \frac{C_D - C_{D,max} \sin(\alpha)^2}{\cos(\alpha)}. \quad (2.31)$$

In order to guarantee continuity at stall Eq.s 2.30 and 2.31 should be rewritten as

$$A_2 = (C_{L,s} - C_{D,max} \sin(\alpha_s) \cos(\alpha_s)) \frac{\sin(\alpha_s)}{\cos(\alpha_s)^2}, \quad (2.32)$$

$$B_2 = \frac{C_{D,s} - C_{D,max} \sin(\alpha_s)^2}{\cos(\alpha_s)}, \quad (2.33)$$

where the subscript s denoted the constant value at stall angle of attack. In Figures 15 and 16 are shown the distribution of lift and drag coefficients as derived from the formulas proposed in Viterna-Corrigan method.

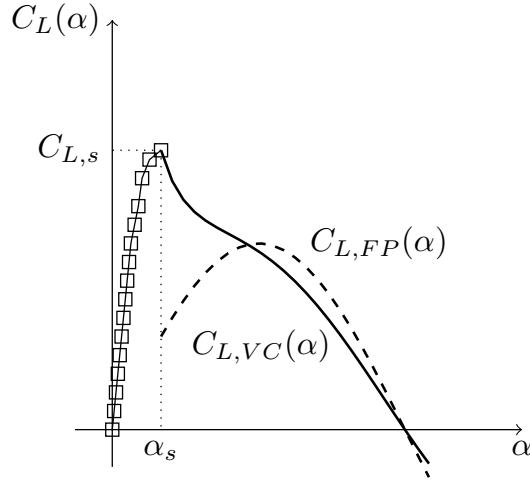


Figure 15: Sketch of Viterna-Corrigan lift coefficient distribution (solid line) together with flat plate theory result (dashed line) for some measurements data (squares)

As stated in Equations 2.24-2.25, the Viterna-Corrigan method consists of two distribution added up together: a first one, related to A_1 , B_1 coefficients, scale-similar to flat plate theory results $C_{L,FP}$, $C_{D,FP}$ as

$$C_{L,FP} = 2 \sin(\alpha) \cos(\alpha) = \sin(2\alpha), \quad (2.34)$$

$$C_{D,FP} = 2 \sin(\alpha)^2, \quad (2.35)$$

and a second one, related to A_2 , B_2 coefficients, that guarantees continuity at stall angle of attack, or in general, at the lowest angle of attack where these post-stall equations are connected.

In [73] is reported that at angles of attack of 20, 30 and 45 degrees, ideal flat plate theory results in C_L/C_D ratios of 2.75, 1.73, and 1.00, respectively. For non-rotating wings of different aspect ratios [46] the C_L/C_D ratio closely followed flat plate theory over the angle of attack range of 30 to 90 degrees. For the rotating Unsteady Aerodynamics Experiment (UAE) rotor the C_L/C_D ratio at the five radial stations, at which pressure measurements were acquired closely follow flat plate theory over the angle of attack range of 20 to 90 degrees. Although flat plate theory provides guidance for the post-stall C_L/C_D ratios for angles of attack in the range of 20 to 90 degrees, wind turbine power calculations are also dependent on the magnitude of the associated C_L and C_D . The magnitudes of these parameters at 20 degrees are airfoil and blade planform dependent. At 20 degrees the rapidly increasing drag dominates the C_L/C_D ratio. At 90 degrees, where the lift is close to zero, blade planform or aspect ratio effects dictate the drag. However, for very large wind turbine blades with airfoil thickness of up to 40 percent, airfoil thickness also becomes a factor in determining the drag at 90 degrees. The airfoil starts acting more like an ellipse than a flat plate. Non-rotating semi-span tests [46] found the maximum drag at 90 degrees to decrease with airfoil thickness over the range of 9 to 18 percent for a given aspect ratio wing.

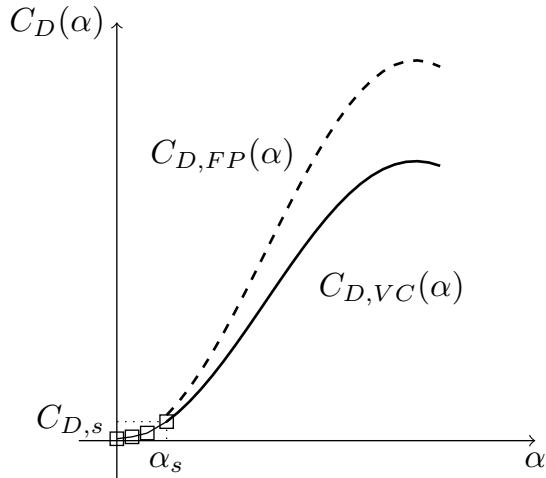


Figure 16: Sketch of Viterna-Corrigan drag coefficient distribution (solid line) together with flat plate theory result (dashed line) for some measurements data (squares)

The original Viterna-Corrigan equations shown below require an initial angle of attack (α_s) with its associated drag ($C_{D,s}$) and lift coefficient ($C_{L,s}$) along with a blade aspect ratio (AR). An important requirement is for the Viterna-Corrigan equations to satisfy flat plate theory. This condition is only satisfied when the C_L/C_D at the initial angle of attack agrees with flat plate theory. Otherwise, the C_L/C_D at higher angles will not agree with flat plate theory. In addition, results with the Viterna-Corrigan equations are largely dependent on the magnitude of the initial values of C_L and C_D . The blade AR selection is of lesser importance. The AR is needed for determining a maximum blade drag coefficient ($C_{D,max}$) at 90 degrees. The AR selection has an effect on post peak power prediction at wind speeds around 20 m/s with a larger AR resulting in greater high wind speed lift, drag and power.

The choice of the airfoil's stall or leading-edge separation angle of attack and associated drag strongly influence predicted power just after peak power. Viterna-Corrigan's equations are based on using the airfoil stall angle at maximum C_L along with the associated maximum C_L and C_D . Another option is to use the leading-edge separation angle that corresponds to the local C_L minimum just after maximum C_L . Unfortunately, neither one of these options provides usually a C_L/C_D for the initial condition of the Viterna-Corrigan equations that satisfy flat plate theory.

Actual design with Viterna-Corrigan post-stall model

The Viterna-Corrigan post-stall model is based on an assumption of no twisted blade, and it can guarantee a constant power extraction after normal operating condition of a HAWT. In principle, it would be possible to adapt this method also to twisted blades that without any other correction would perform poorly, as depicted in Figure 17 with the dashed line.

Because of the twist angle uniformly applied along the span, a decrease in the aerodynamic power curve is obtained. This aspect could be corrected by using a

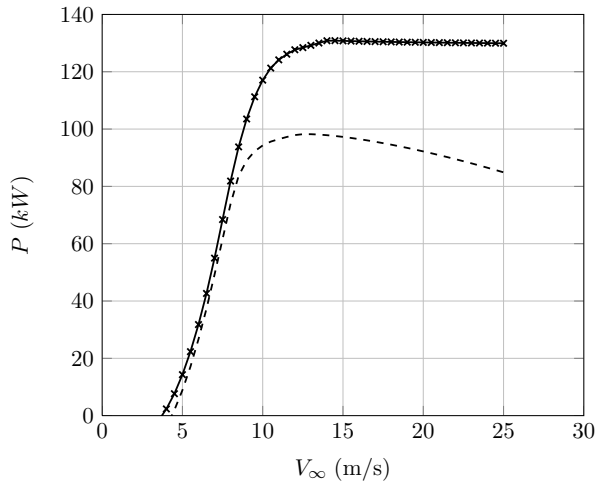


Figure 17: Effects of blade planform on aerodynamic power vs wind speed: — no pitched blade, -- 3 degrees pitched blade, Δ 3 degrees pitched blade with cambered airfoil

cambered airfoil (or a more cambered one), that despite the twist angle, would lead to a similar result as the one obtained for a non twisted blade (see the triangle curve in Figure 17). From this point of view the Vitern-Corrigan method, once has been verified its reliability with respect to experimental data, could be used as a criterion for designing a stall-controlled HAWT blade, suggesting the proper relationship between section twist angle and airfoil camber.

In Figure 18 the aerodynamic power against the wind speed for a case study HAWT with different coupling for extrapolation method. The vertical dashed line marks the beginning of the post-stall model affection on performance.

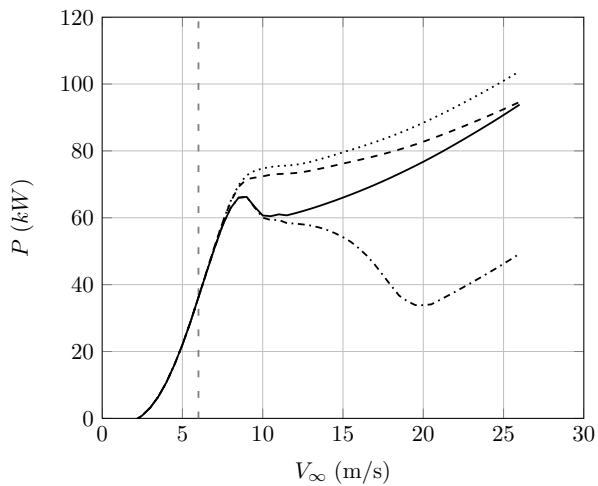


Figure 18: Effects of V.C. settings on aerodynamic power vs wind speed: — V.C. last point., -- V.C. after stall, \cdots V.C. at stall, - · - V.C. flat plate efficiency constraint

2.2.2 AERODAS

In the AERODAS model [66] an empirical approach is applied, in which the trends of test data are identified for a wide variety of airfoils and for the Unsteady Aerodynamics Experiment (UAE) wind turbine. These trends are then modelled by a set of algebraic equations based on the best fit of the model to available test data and not on aerodynamic theory. The lift and drag properties of infinite- and finite-length circular cylinders and thin plates are also modelled by these same empirical equations. The development of lift and drag models in this study extends and broadens previously published work in several areas, as follows:

1. The test data base is significantly broadened to include a wide range of airfoils, aspect ratios, Reynolds numbers, angles of attack, and the presence or absence of leading-edge trip strips.
2. Lift and drag behaviour at high angles of attack in the post-stall regime are not assumed to be the same as the behaviour of flat plates as in earlier simplified models. Instead, empirical equations are derived based on the measured behaviour of the airfoils themselves.
3. Airfoil thickness is added to aspect ratio and angle of attack as another dependent variable in the model equations.
4. Mean and standard deviations of the proposed model from most of the available airfoil test data are calculated. In this way, the accuracy can be measured of the assumption that the lift and drag properties of all airfoils in the post-stall regime can be represented by a single set of models.
5. Wind turbine rotor power and wind tunnel fan pressure rise are calculated on the basis of model lift and drag coefficients as input to a basic blade element-momentum (BEM) performance code. Mean and standard deviations from measured power are calculated. This permits quantitative evaluation of the assumption that static airfoil lift and drag data can be applied successfully in BEM performance analyses of rotating turbine and fan blades.

Input parameters and adjustments for finite aspect ratio

The model input parameters are the angle of attack at which $CL_1 = 0$ for all aspect ratios, A_0 (deg), the angle of attack at maximum pre-stall lift, ACL_1' (deg), the maximum pre-stall lift coefficient at $\alpha = ACL_1'$, CL_{1max}' , the slope of linear segment of pre-stall lift curve, S_1' (1/deg), the minimum drag coefficient at $\alpha = A_0$ for all aspect ratios, CD_0 , the angle of attack at maximum pre-stall drag, ACD_1' (deg), the maximum pre-stall drag coefficient at $\alpha = ACD_1'$, CD_{1max}' . They should be corrected for finite aspect ratio via the following relations:

$$\alpha = \alpha' + 57.3 \cdot CL_1' \left(\frac{1 + \tau}{\pi AR} \right) = \alpha' + 57.3 \cdot CL_1' \cdot E[\tau], \quad (2.36)$$

$$CD_1 = CD_1' + CL_1'^2 \left(\frac{1 + \sigma}{\pi AR} \right) = \alpha' + CL_1'^2 \cdot E[\sigma], \quad (2.37)$$

where $CL1'$ is the pre-stall lift coefficient for infinite aspect ratio, α' is the angle of attack for infinite aspect ratio for a lift coefficient CL' (deg), τ is the empirical reference term for adjusting angle of attack function of aspect ratio, $CD1'$ is the pre-stall drag coefficient for infinite aspect ratio at a lift coefficient $CL1'$, σ is the empirical reference term for adjusting drag coefficient; function of aspect ratio and E is the aspect ratio adjustment function function of τ, σ as

$$E[\tau] = \left(\frac{1 + \tau}{\pi AR} \right) = 0.318 AR^{-0.90}, \quad (2.38)$$

$$E[\sigma] = \left(\frac{1 + \sigma}{\pi AR} \right) = 0.280 AR^{-0.90}, \quad (2.39)$$

that transform Eq.s 2.36 and 2.37 in

$$\alpha = \alpha' + 18.2 CL1' \cdot AR^{-0.90}, \quad (2.40)$$

$$CD1 = CD1' + 0.280 CL1'^2 AR^{-0.90}, \quad (2.41)$$

that help to correct all other input parameters as follows

$$ACL1 = ACL1' + 18.2 CL1_{max}' \cdot AR^{-0.90}, \quad (2.42)$$

$$ACD1 = ACD1' + 18.2 CL1_{max}' \cdot AR^{-0.90}, \quad (2.43)$$

$$S1 = \frac{S1'}{1 + 18.2 S1' \cdot AR^{-0.90}}, \quad (2.44)$$

$$CD1_{max} = CD1_{max}' + 0.280 CL1_{max}'^2 AR^{-0.90}, \quad (2.45)$$

The fifth input parameter, $CL1_{max}'$, is adjusted on the basis of the following empirical equation derived from $CL1_{max}$ test data presented by Ostowari and Naik [44] for NACA 4415 and 4418 airfoils at four Reynolds numbers, with both tripped and clean leading edges:

$$CL1_{max} = CL1_{max}' \left\{ 0.67 + 0.33 \exp \left[- \left(\frac{4}{AR} \right)^2 \right] \right\}, \quad (2.46)$$

Equations for coefficients in the pre-stall regime

The lift coefficient could be computed as

$$C_{L,1} = S1(\alpha - \alpha_0) - R_{C_{L,1}} \left(\frac{\alpha - \alpha_0}{\alpha_{C_{L,1}} - \alpha_0} \right)^{N_1}, \quad (2.47)$$

where $R_{C_{L,1}}$ is the reduction from extension of linear segment of lift curve to $CL1_{max}$ and N_1 is the exponent defining shape of lift curve at $ACL1_{max}$, whose expressions are:

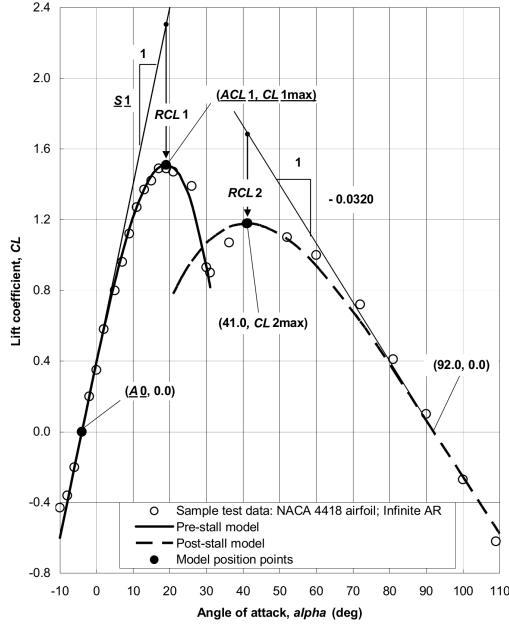


Figure 19: Configurations of the proposed AERODAS models for calculating lift and drag coefficients in the pre-stall and post-stall regimes. Input parameters are underlined. Lift coefficient model (from [66]).

$$R_{C_{L,1}} = S_1 (\alpha_{C_{L,1}} - \alpha_0) - C_{L,1,max} \quad (2.48)$$

$$N_1 = 1 + C_{L,1,max} / R_{C_{L,1}} \quad (2.49)$$

The pre-stall drag curve is commonly defined as a quadratic equation, $M = 2.0$, in terms of the angle of attack, as follows:

$$C_{D,1} = \begin{cases} C_{D,0} + (C_{D,1,max} - C_{D,0}) \left(\frac{\alpha - \alpha_0}{\alpha_{C_{D,1}} - \alpha_0} \right)^2, \\ \quad \text{if } (2A_0 - ACD1) \leq \alpha \leq ACL1 \\ 0, \text{ if } \alpha > ACL1. \end{cases} \quad (2.50)$$

Equations for coefficients in the post-stall regime

Referring to Figure 19-20, the maximum lift and drag coefficients in the post-stall regime are assumed to be functions of the airfoil's thickness-to-chord ratio and its aspect ratio, arranged in the following form:

$$CL2max = F1 [t/c] \cdot F2 [AR], \text{ at } \alpha = 41 \text{ deg}, \quad (2.51)$$

$$CD2max = G1 [t/c] \cdot G2 [AR], \text{ at } \alpha = 90 \text{ deg}, \quad (2.52)$$

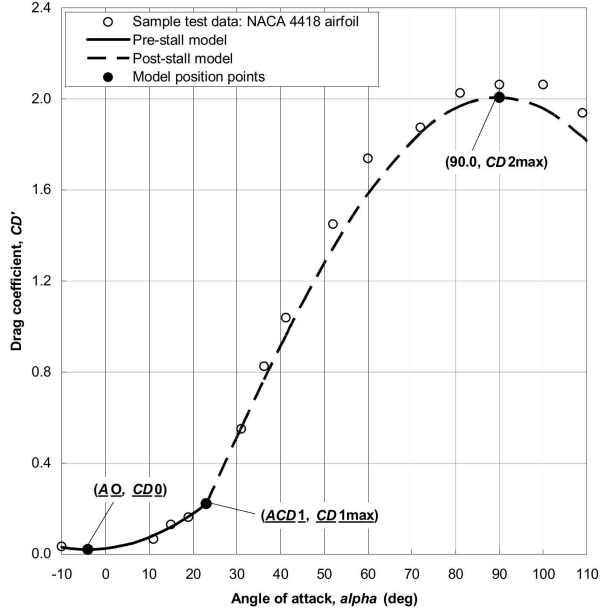


Figure 20: Configurations of the proposed AERODAS models for calculating lift and drag coefficients in the pre-stall and post-stall regimes. Input parameters are underlined. Drag coefficient model (from [66]).

where t/c is the airfoil thickness-to-chord ratio, $F1, G1$ are empirical functions of t/c and $F2, G2$ are empirical functions of AR defined as follows

$$F1 = 1.190 \left[1 - \left(\frac{t}{c} \right)^2 \right], \quad (2.53)$$

$$F2 = 0.65 + 0.35 \exp \left[- \left(\frac{9}{AR} \right)^{2.3} \right], \quad (2.54)$$

$$G1 = 2.3 \exp \left\{ - \left[0.65 \left(\frac{t}{c} \right) \right]^{0.90} \right\}, \quad (2.55)$$

$$G2 = 0.52 + 0.48 \exp \left[- \left(\frac{6.5}{AR} \right)^{1.1} \right]. \quad (2.56)$$

Referring again to Figure 19, lift variation with angle of attack in the post-stall regime is modelled in AERODAS by an equation of the same form as that applied in the pre-stall regime, but with a reversed slope, as follows:

$$C_{L,2} = \begin{cases} 0, & \text{if } 0 \leq \alpha \leq ACL1, \\ -0.032(\alpha - 92) - R_{C_{L,2}} \left(\frac{92 - \alpha}{51} \right)^{N_2}, & \text{if } ACL1 \leq \alpha \leq 92, \\ -0.032(\alpha - 92) + R_{C_{L,2}} \left(\frac{\alpha - 92}{51} \right)^{N_2}, & \text{if } \alpha > 92, \end{cases} \quad (2.57)$$

METHOD

where R_{CL2} is the reduction from extension of linear segment of lift curve to CL_{2max} and N_2 is the exponent defining shape of lift curve at CL_{2max} , both expressed as

$$R_{CL,2} = 1.632 - C_{L,2,max}, \quad (2.58)$$

$$N_2 = 1 + \frac{C_{L,2,max}}{R_{CL,2}}. \quad (2.59)$$

Post-stall lift behaviour at a negative angle of attack is assumed to be anti-symmetric about $\alpha = A_0$.

Referring to Figure 20, the drag variation with angle of attack in the post-stall regime is modelled in AERODAS by a sine curve that peaks at an angle of attack of 90 deg and intersects the pre-stall drag curve at coordinates $(ACD1, CD_{1max})$, as follows:

$$C_{D,2} = \begin{cases} 0, & \text{if } (2A_0 - ACL1) \leq \alpha \leq ACL1, \\ C_{D,1,max} + \\ (C_{D,2,max} - C_{D,1,max}) \sin\left(\frac{\alpha - ACD1}{90 - ACD1} \cdot 90\right), & \\ \text{if } \alpha \geq ACL1. \end{cases} \quad (2.60)$$

At negative angles of attack, the post-stall drag model is symmetrical about $\alpha = A_0$.

Finally one have the general expressions for lift and drag coefficient:

$$C_{L,AERODAS} = \max(C_{L,1}, C_{L,2}), \quad (2.61)$$

$$C_{D,AERODAS} = \max(C_{D,1}, C_{D,2}). \quad (2.62)$$

2.3 EXPERIMENTAL SET-UP

The test section of the closed circuit wind tunnel of the Department of Industrial Engineering of University of Naples Federico II has been equipped with an additional vertical wall to meet the model wingspan reducing the width of the test section (see Figure 21).

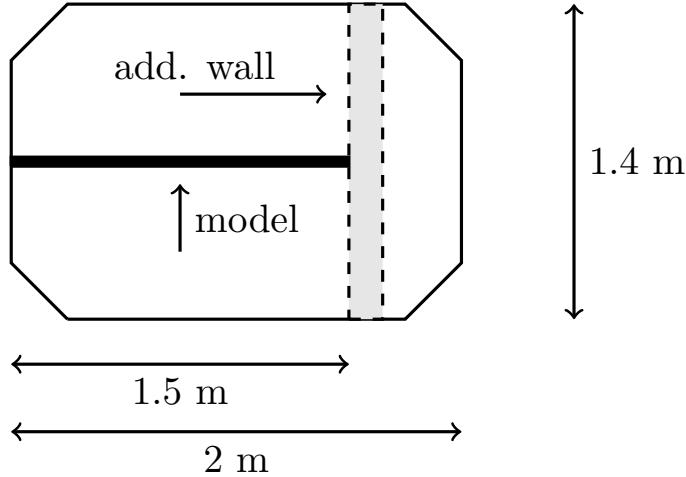


Figure 21: Configuration of test section with the additional wall

The airfoil models are horizontally mounted and instrumented with staggered pressure ports on the midspan surface, while the force measurements are accomplished by force balance for lift and pitching moment. Pressure values are collected via miniature pressure scanner ZOC 33 manufactured by Scanivalve [56] with a full scale range of 10 inch H₂O (i.e. equal to about 2.5 kPa) and an accuracy of $\pm 0.15\%$ of the full scale range (i.e. ± 3.75 Pa). In Table 3 are summarised the informations in more detail.

Airfoil	Pressure ports	Re
NACA 0018	45	115...290e3
NACA 0018 (trip)	40	115...290e3

Table 3: Test section with additional wall experiments setting.

In Figure 22 a sketch of the pressure ports distribution on the midspan section is shown, while in Figure 23 a picture of the pressure ports on the instrumented section is reproduced.



Figure 22: NACA 0018 sketch of the pressure ports distribution on the mid span section

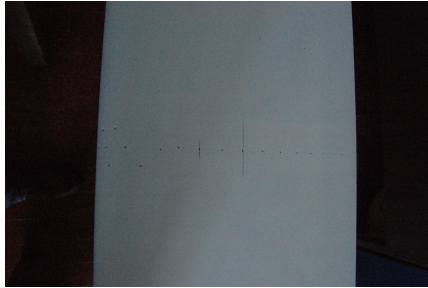
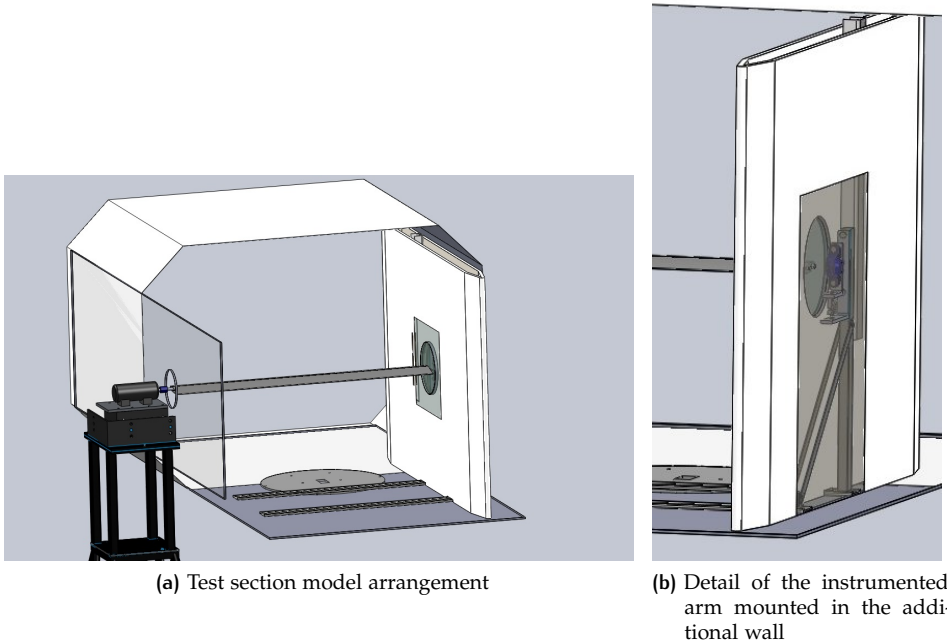


Figure 23: NACA 0018 model pressure ports distribution on the mid span section, upper side surface

In Figure 24a a CAD model (realized with SolidWorks¹) reproducing the testing apparatus is reproduced, with the force balance located on the left side, outside the test section, the airfoil model spanning from left to right up to the additional wall in which is located a second instrumented supporting arm. In Figure 24b a detailed CAD view of the instrumented supporting arm, equipped with a Y-bearing plummer block unit², located in the additional wall is reproduced.



(a) Test section model arrangement

(b) Detail of the instrumented arm mounted in the additional wall

Figure 24: NACA 0018 model arrangement in the closed test section wind tunnel with additional wall

¹ © Dassault Systems <http://www.solidworks.com/sw/education/education-software-mcad.htm>
² <http://www.skf.com/group/products/bearings-units-housings/bearing-units/ball-bearing-units/index.html>

The need for a both force and pressure based measurements system for lift coefficient could be explained as follows: the high angle of attack region where the post-stall its realized constitutes a tough challenge for pressure measurements, especially for those prescribed to lie in only one section, as in this case. Although a 2D testing arrangement has been realized, when the angle of attack is comprised within 25 and 50 degrees, it is always present on the model surface a distribution of stall cells, with a kind of mushroom like shape, whose dimension and placement along the span is dependent on the model geometric aspect ratio, in this case 10. This phenomenon induces an intrinsic local nature of the mid-span pressure sensor measure so that only a force balance measurements could correctly capture the integral (meaning that the lift force is derived by integration of pressure on the body) value of the force acting on the body. In Figure 25 mushroom shaped stall cell from both literature [23] and the experiments carried out in this works has been reproduced.

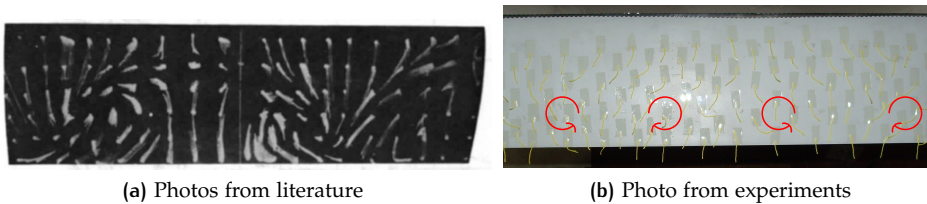


Figure 25: Mushroom shaped stall cell from literature and experiments

In Figure 26 is illustrated the reason for which force balance measurements are used within this work to collect the information about the drag coefficient too, giving a comparison of both numerical and experimental data for drag coefficient vs angle of attack consisting of:

- OpenFOAM CFD simulation, continuous line;
- XFOIL simulation, dotted line;
- experimental measurements from this work, triangles;
- experimental data from Delft, squares.

The grey line indicates the stall onset, so that for higher angle of attack (AoA) is clearly visible a fairly good match between the two experiments data and the CFD simulation, while XFOIL is of course able to describe only the attached flow condition region before the stall onset. The wake pressure rake measurements would have resulted in a good measure only in attached flow region, i. e. not the portion of airfoil operating condition on which mainly focuses this work.

For such reasons a double measurements system, composed by both force and pressure sensors, has been adopted, thus having an integral description of lift coefficient avoiding the problem of local flow condition because of stall cells, while keep tracking via the pressure taps on the body the pressure coefficient C_p chord-wise distribution describing the laminar bubble position and importance, and finally capturing the drag coefficient value in post-stall region.

A comparison with some of the results collected by Timmer in [75] for the NACA 0018 tested in the low speed wind tunnel facility of Delft University would be performed.

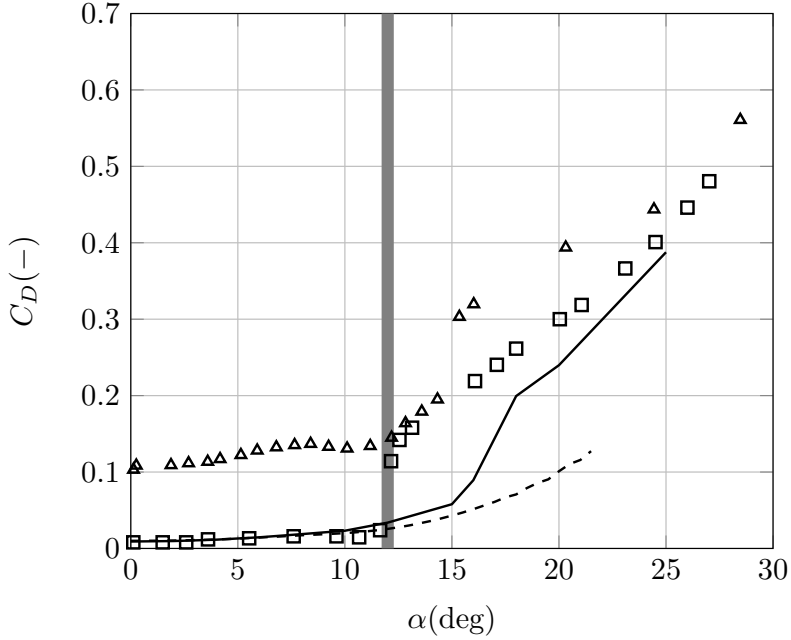


Figure 26: NACA 0018 comparison of numerical and experimental measurements for drag coefficient vs AoA at about $Re = 300e3$: \square Delft exp. $Re = 300e3$, \triangle Exp. $Re = 290e3$, — OpenFOAM $Re = 290e3$, - - XFOIL $Re = 290e3$

2.3.1 Corrections of measurements

Corrections of measured data for blockage and other effects have been made accordingly with literature [36, 21, 19, 4, 6, 16, 26].

Buoyancy corrections

The laminar boundary layer thickness δ_{lbl} at test section exit is:

$$\delta_{lbl} = 1.72 \frac{x}{\sqrt{Re}}, \quad (2.63)$$

where $x = 2.0$ m is the test section length. The effective area $A_{2,eff}$ is:

$$A_{2,eff} = (H - 2\delta_{lbl}) \cdot (L - 2\delta_{lbl}), \quad (2.64)$$

where $H = 1.38$ m is the test section height, $L = 1.50$ m is the test section width. The effective velocity V_2 is:

$$V_2 = V_1 \cdot \frac{A_1}{A_{2,eff}}, \quad (2.65)$$

where V_1 is the velocity at the test section entrance whose area is $A_1 = H \cdot L$. The effective pressure P_2 is:

$$P_2 = P_1 + 0.5 \cdot \rho \cdot (V_1^2 - V_2^2), \quad (2.66)$$

where P_1 is the pressure at the test section entrance and ρ is the air density in the test section. The pressure ratio is:

$$\frac{\partial p}{\partial l} = \frac{P_2 - P_1}{x}, \quad (2.67)$$

Body thickness, chord and volume could be corrected taking into account the angle of attack as follows:

$$t(\alpha) = \max \tau, c \sin \alpha, \quad (2.68a)$$

$$c(\alpha) = c \cos \alpha, \quad (2.68b)$$

$$\text{volume}(\alpha) = 0.7 \cdot t(\alpha) \cdot c(\alpha) \cdot L. \quad (2.68c)$$

The buoyancy drag is:

$$\Delta D_b = -\frac{\partial p}{\partial l} \text{volume}(\alpha). \quad (2.69)$$

Solid blockage

Assuming the following constant $\lambda_2 = 5$, based on model geometry, from literature, the solid blockage coefficient could be derived as follows:

$$\Lambda = 4\lambda_2 \left(\frac{t(\alpha)}{c(\alpha)} \right)^2, \quad (2.70a)$$

$$\sigma = \frac{\pi^2}{48} \left(\frac{c(\alpha)}{H} \right)^2, \quad (2.70b)$$

$$\epsilon_{sb} = \sigma\Lambda. \quad (2.70c)$$

Streamline curvature

Because of the streamline curvature the following corrections should be provided for the angle of attack and the aerodynamic coefficients:

$$\alpha_{\text{corr}} = \alpha + \frac{57.3\sigma}{2\pi} (C_L + 4C_M), \quad (2.71a)$$

$$C_{L,\text{corr}} = C_L(1 - \sigma - 2\epsilon_{sb}), \quad (2.71b)$$

$$C_{M,\text{corr}} = C_M(1 - 2\epsilon_{sb}), \quad (2.71c)$$

$$C_{D,\text{corr}} = C_D(1 - 2\epsilon_{sb}). \quad (2.71d)$$

3 | RESULTS

3.1 A TEST CASE: DU-97-W-300

In this section are collected the results obtained using the method discussed in Section 2.1 for the airfoil DU-97-W-300 tested in the TU Delft low turbulence wind tunnel facility for both clean and tripped configuration [74, 77]. The airfoil designation comprises the Delft University abbreviation, the design year (1997, shortened in 97), the wind energy application as W and the maximum thickness in percent of the chord, in this case 30 (see Figure 7 for airfoil sketch). The experimental data refer to a Reynolds number ($3e6$) quite higher than the one on which this work focuses (see Table 2), however their are intended to show the capability of a grid induced transition in matching the real behaviour observed in wind tunnel test.

The numerical analysis condition and specification are summarized in following tables. In both cases, respectively clean and tripped configuration, the turbulence model described in subsection 2.1.1 has been used.

Airfoil	Chord	Trip begin	Trip length	Trip height
DU-97-W-300	0.6 m	5.0 %c	1.7 %c	0.35 mm

Table 4: Trip parameters for experiments conducted in TU Delft[74, 77].

Airfoil	Cell number	Re	y^+	Tu_∞ (%)
DU-97-W-300	82025	$3e6$	~ 1	0.1
DU-97-W-300 (tripped)	124680	$3e6$	~ 1	0.1

Table 5: Computational parameters for DU-97-W-300 airfoil.

Turbulence intensity equal to 0.1%, as indicated as the maximum value observed during the experiments by Timmer and van Rooij [74, 77].

In figure 27 is shown the computational grid modified in order to include the step-shaped zigzag tape promoting transition to turbulent flow whose characteristics are indicated in table 4 (the image comes from Paraview [48], an open-source, multi-platform data analysis and visualization application).

3.1.1 Free transition

In Figure 28-29 are shown, respectively, the lift coefficient distribution with respect to the angle of attack and the drag coefficient. The lift coefficient linear portion is well captured only in terms of slope ($C_{L,\alpha}$), while the is in almost all

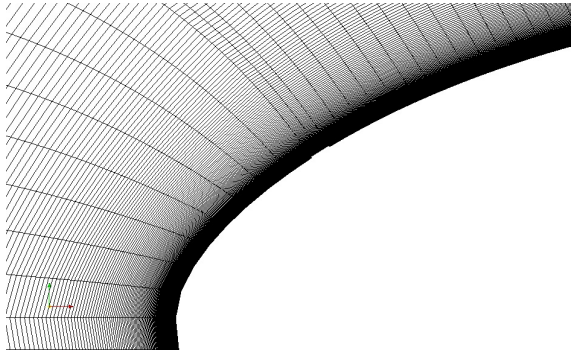


Figure 27: Trip detail in numerical grid for DU-97-W-300 airfoil.

the linear behavior angle of attack range a difference of about 0.2 between the experiments of TU Delft and our numerical simulations. The stall behavior is well captured with only 1 degree difference in terms of stall angle of attack and about 0.1 in terms of maximum attainable lift coefficient ($C_{L,max}$). Drag coefficient distribution exhibits large differences between experiments and numerical simulations that grows rapidly at stall onset so that even a 20-30 counts ($1e^{-4} C_D$) is present in high lift portion.

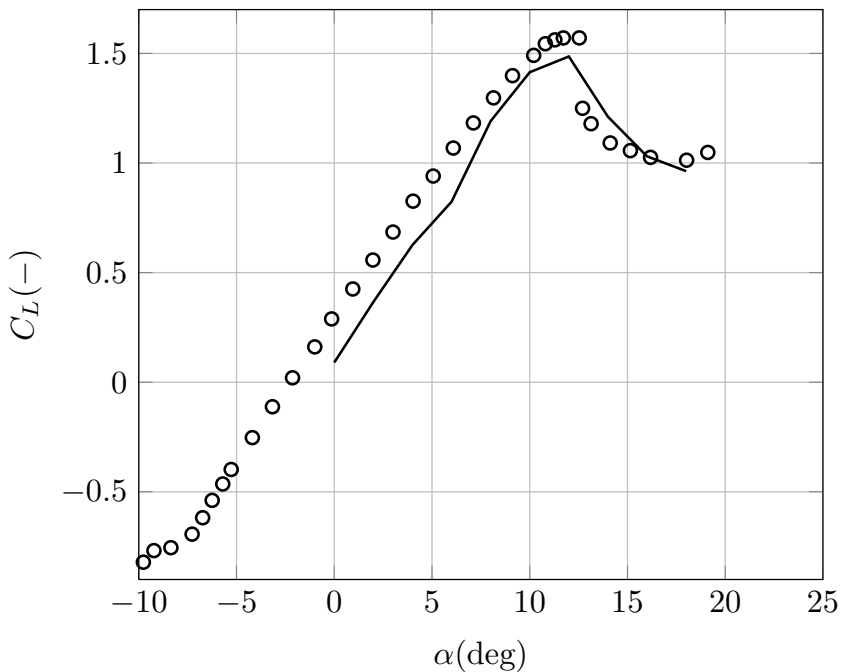


Figure 28: DU-97-W-300, lift coefficient vs angle of attack: Timmer \circ , — num.

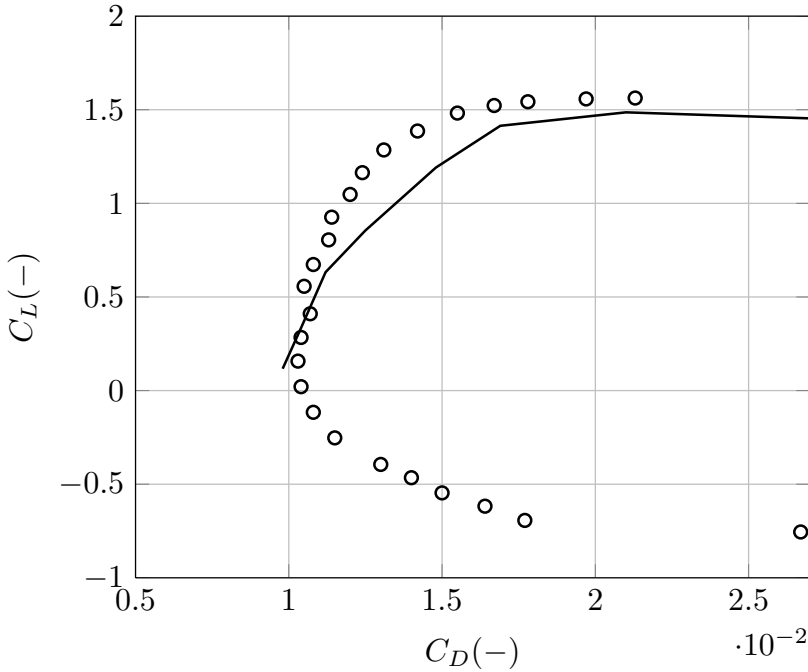


Figure 29: DU-97-W-300, drag coefficient vs angle of attack: Timmer \circ , — num.

3.1.2 Fixed transition

In Figure 30-31 are shown, respectively, the lift coefficient distribution with respect to the angle of attack and the drag coefficient from the imposed transition case. The lift coefficient linear portion is well captured only in terms of slope ($C_{L,\alpha}$), while the is in almost all the linear behavior angle of attack range a difference of about 0.1 between the experiments of TU Delft and our numerical simulations: this appears to be a lower error with respect to the clean case. The stall behavior is well captured with only 1 degree difference in terms of stall angle of attack (it sees a delayed stall) and about 0.2 in terms of maximum attainable lift coefficient ($C_{L,max}$). Drag coefficient distribution exhibits large differences between experiments and numerical simulations that grows rapidly at stall onset so that even a 20-30 counts ($1e^{-4} C_D$) is present in high lift portion, but it seems to have no big differences with respect to the numerical simulation performed for the clean case (see Figure 29).

DU-97-W-300 synoptic table

In this paragraph a synoptic table for the DU-97-W-300 airfoil is presented in order to summarize the main aerodynamic characteristics for both clean and tripped condition derived from a comparison between experimental measurements and numerical analysis.

RESULTS

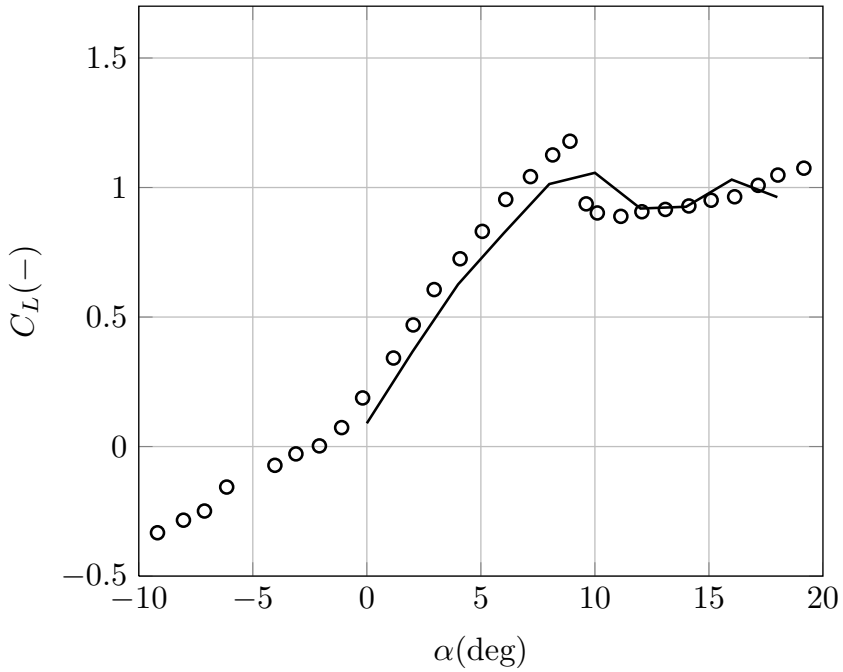


Figure 30: DU-97-W-300, lift coefficient vs angle of attack tripped case: Timmer \circ , — num.

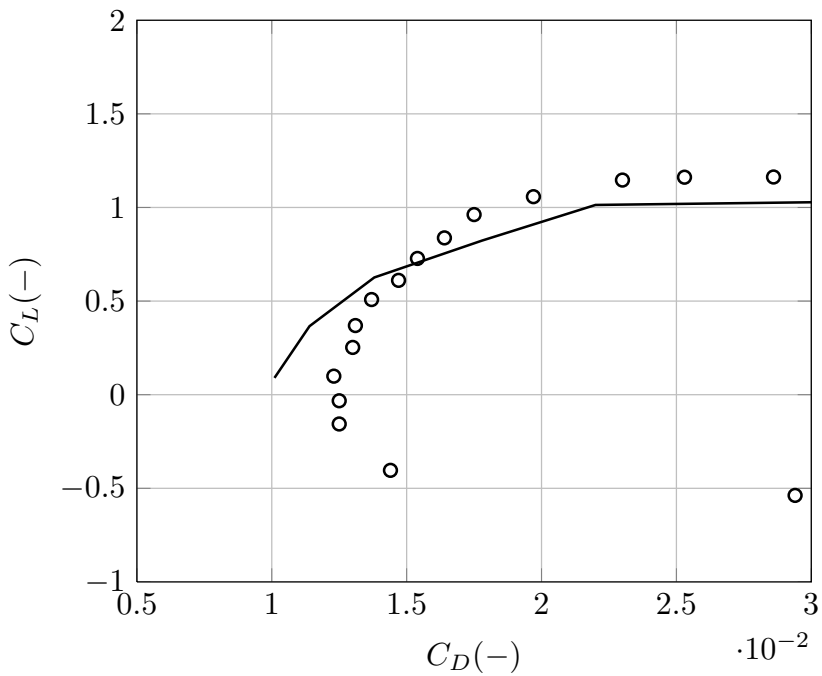


Figure 31: DU-97-W-300, drag coefficient vs angle of attack tripped case: Timmer \circ , — num.

		Re = 3e6		
Parameter		Exp.	Num.	$\Delta(\%)$
clean	α_{0L} (deg)	-2.3	-0.7	+70
	$C_{L,\alpha}$ (deg^{-1})	0.1285	0.1381	+7.5
	E_{\max} (-)	98.1069	83.6805	-15
	$\alpha_{E_{\max}}$ (deg)	6.9	10	+45
	$C_{L,\max}$ (-)	1.5708	1.4861	-5.4
	$\alpha_{C_{L,\max}}$ (deg)	12.5	12	-4
tripped	α_{0L} (deg)	-2.2	-0.7	+68
	$C_{L,\alpha}$ (deg^{-1})	0.1245	0.1381	+11
	E_{\max} (-)	54.9714	46.2528	-16
	$\alpha_{E_{\max}}$ (deg)	6.2	6	-3
	$C_{L,\max}$ (-)	1.1627	1.0568	-9
	$\alpha_{C_{L,\max}}$ (deg)	8.7	10	-15

Table 6: DU-97-W-300 synoptic table for aerodynamic characteristics

3.2 NACA 0018

The results of experimental measurements would be shown at first; a comparison with CFD numerical simulation would be presented at second; finally a comparison with the post-stall semi-empirical models would be performed and discussed.

3.2.1 Experiments

In this section the results from measurements are summarized.

Free transition

In Figure 32 a detail of lift coefficient distribution in low to medium angle of attack regime measured with force balance is shown. The lower Reynolds curve exhibits a large effect of a laminar bubble that induces a higher lift coefficient for angle of attack lower than 6 degrees. The maximum lift coefficient is only limited affected by Reynolds number (about 0.05) while the angle of attack at stall is observed to be located at, respectively, 11, 14 and 15 degrees for Reynolds number from 115e3 to 290e3. The stall behavior is characterized by an abrupt decrease in lift coefficient due to the sudden separation at the end of the laminar bubble that moves forth with increasing angle of attack. After the stall no big differences are noticed with the Reynolds number. Figure 33 shows the complete lift coefficient distribution for the entire angle of attack region investigated.

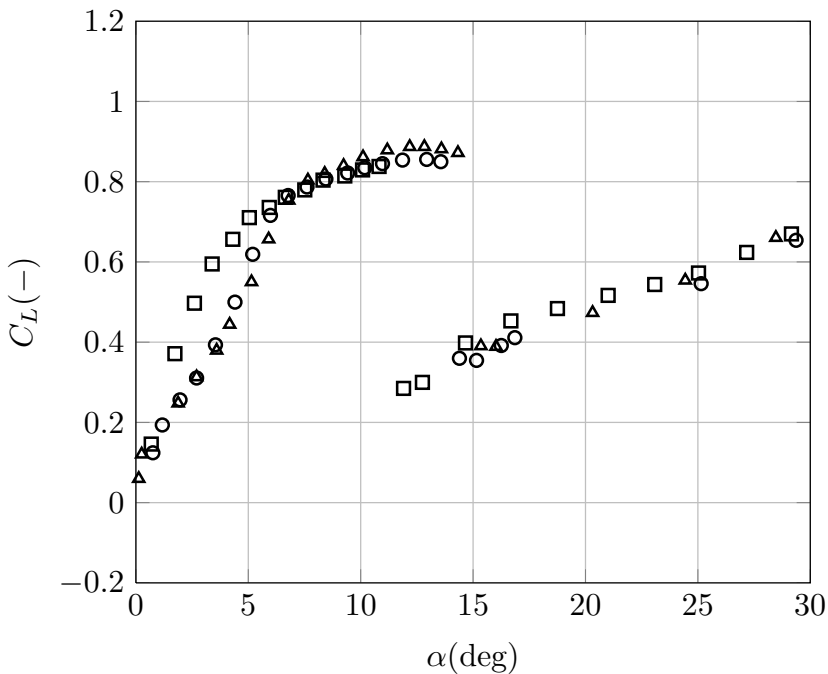


Figure 32: NACA 0018 detail of experimental lift coefficient vs angle of attack: \square Re = 115e3, \circ Re = 230e3, \triangle Re = 290e3

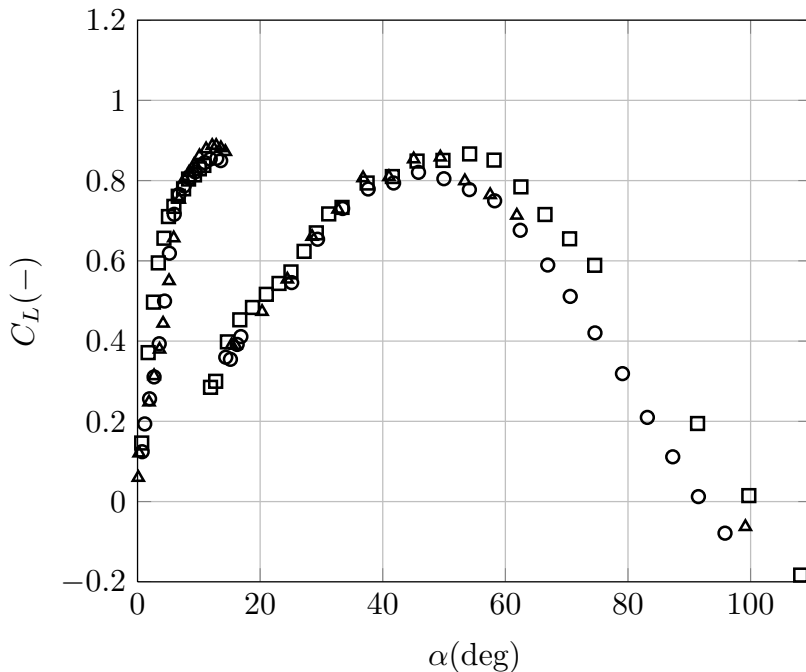


Figure 33: NACA 0018 experimental lift coefficient vs angle of attack: □ Re = 115e3, ○ Re = 230e3, △ Re = 290e3

In Figure 34 is shown the distribution of drag coefficient for the entire range of angle of attack investigated, based on force balance measurements. No detail is shown for the low to medium angle of attack region because of pressure rake wake measurements taken in our experiments. The measurements are compatible with the flat plate theory for very high angle of attack¹.

As reported in section 2.2, Tangler [73] suggest as attachment point of Viterna-Corrigan extrapolation to be located at the angle of attack for which the experimental or numerical data match the flat plate efficiency. In Figure 35 the efficiency of NACA 0018 airfoil for the three Reynolds numbers tested is shown, together with the theoretical value for the flat plate derived dividing equation 2.34 by equation 2.35. The flat plate analytical distribution is met only at very high angle of attack, namely higher than those indicated by Tangler in [73] so that any useful post-stall behavior could be extrapolated if one would need to know in advance aerodynamic coefficient data up to 40 degrees and more. In fact, passive stall controlled HAWT generally operate in off design with blade section experiencing angle of attack comprised between 20 and 35-40 degrees, thus post-stall modelling is strictly needed well below the point where it seems that our experimental results match the theoretical flat plate efficiency.

¹ The results for the lower Reynolds number, namely Re = 115e3, exhibits an quite different behavior with respect to the other two Reynolds number values investigated. However this circumstance is not present for the tripped condition test as shown in Figure 38 on 45

RESULTS

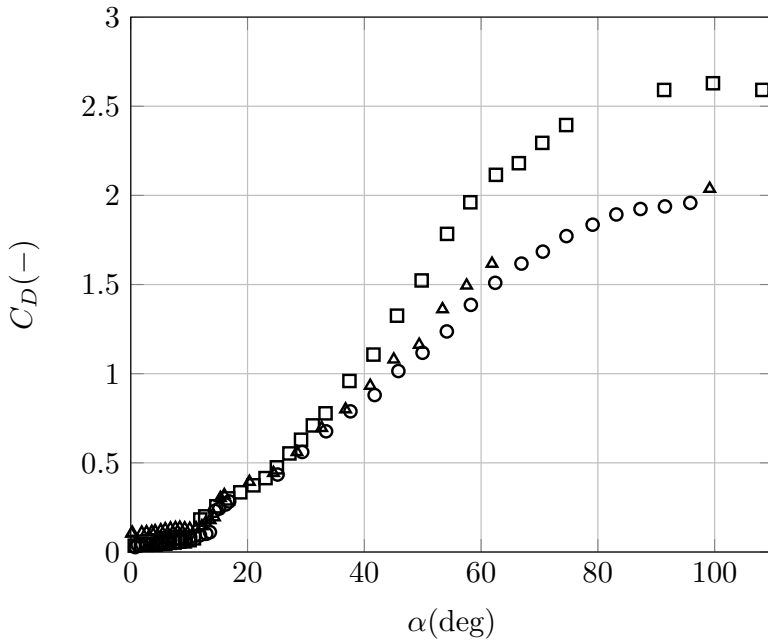


Figure 34: NACA 0018 experimental drag coefficient vs angle of attack: \square $Re = 115e3$, \circ $Re = 230e3$, \triangle $Re = 290e3$

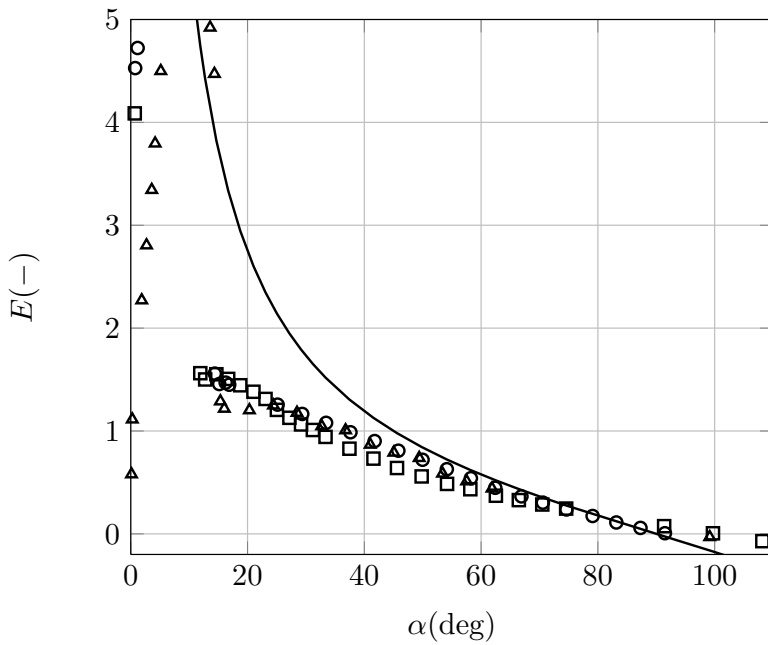


Figure 35: NACA 0018 experimental aerodynamic efficiency vs angle of attack: \square $Re = 115e3$, \circ $Re = 230e3$, \triangle $Re = 290e3$, — flat plate

Fixed transition

In Figure 36 a detail of lift coefficient distribution in low to medium angle of attack regime measured with force balance is shown. The lower Reynolds curve exhibits, as in free transition case, a large effect of a laminar bubble that induces a higher lift coefficient for angle of attack lower than 6 degrees. The maximum lift coefficient is not affected by Reynolds number while the angle of attack of post-stall part begin - i.e. the angle of attack from which it clearly appear the increasing tendency toward the secondary peak in lift coefficient - is observed to be located at, respectively, 20, 22 and 24 degrees for Reynolds number from $115e3$ to $290e3$. The stall behavior is characterized by a flat, nearly constant lift coefficient due to the removed effect of the laminar bubble that in the clean case moves forth with increasing angle of attack.

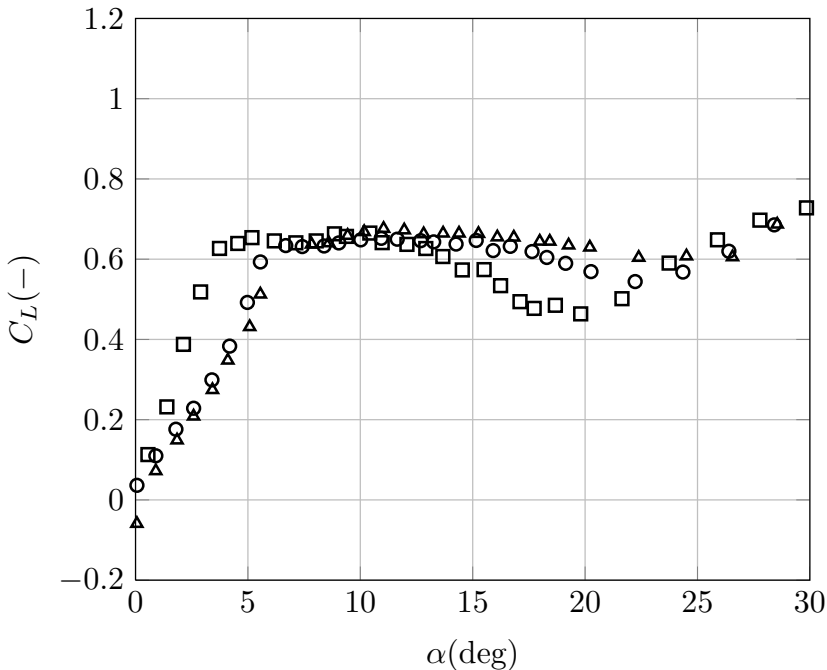


Figure 36: NACA 0018 detail of experimental lift coefficient vs angle of attack for tripped case: \square $Re = 115e3$, \circ $Re = 230e3$, \triangle $Re = 290e3$

After the stall no big differences are noticed with the Reynolds number. Figure 37 shows the complete lift coefficient distribution for the entire angle of attack region investigated.

In Figure 38 is shown the distribution of drag coefficient for the entire range of angle of attack investigated, based on force balance measurements. No detail is shown for the low to medium angle of attack region because of pressure rake wake measurements taken in our experiments. The measurements are compatible with the flat plate theory for very high angle of attack.

As reported in section 2.2, Tangler [73] suggest as attachment point of Viterna-Corrigan extrapolation to be located at the angle of attack for which the experimental or numerical data match the flat plate efficiency. In Figure 39 the efficiency of NACA 0018 airfoil for the three Reynolds numbers tested is shown,

RESULTS

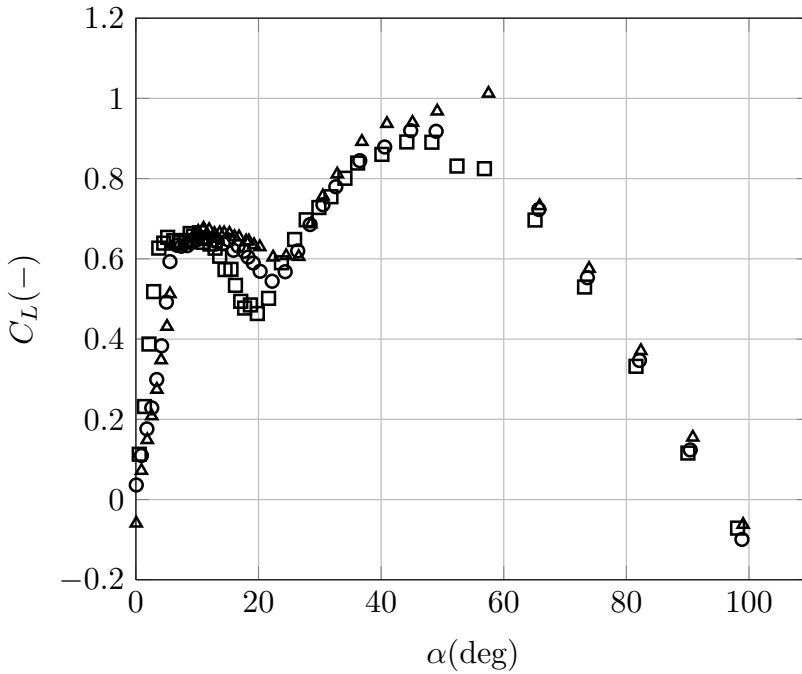


Figure 37: NACA 0018 experimental lift coefficient vs angle of attack for tripped case: \square $Re = 115e3$, \circ $Re = 230e3$, \triangle $Re = 290e3$

together with the theoretical value for the flat plate derived dividing equation 2.34 by equation 2.35. The flat plate analytical distribution is met only at very high angle of attack, namely higher than those indicated by Tangler in [73] so that any useful post-stall behavior could be extrapolated if one would need to know in advance aerodynamic coefficient data up to 40 degrees and more. In fact, passive stall controlled HAWT generally operate in off design with blade section experiencing angle of attack comprised between 20 and 35-40 degrees, thus post-stall modelling is strictly needed well below the point where it seems that our experimental results match the theoretical flat plate efficiency. Moreover, this forced transition case exhibits also that in our experiments the region where bigger difference between measured data and analytical values is located exactly in the post-stall region where HAWT off design operation is needed most.

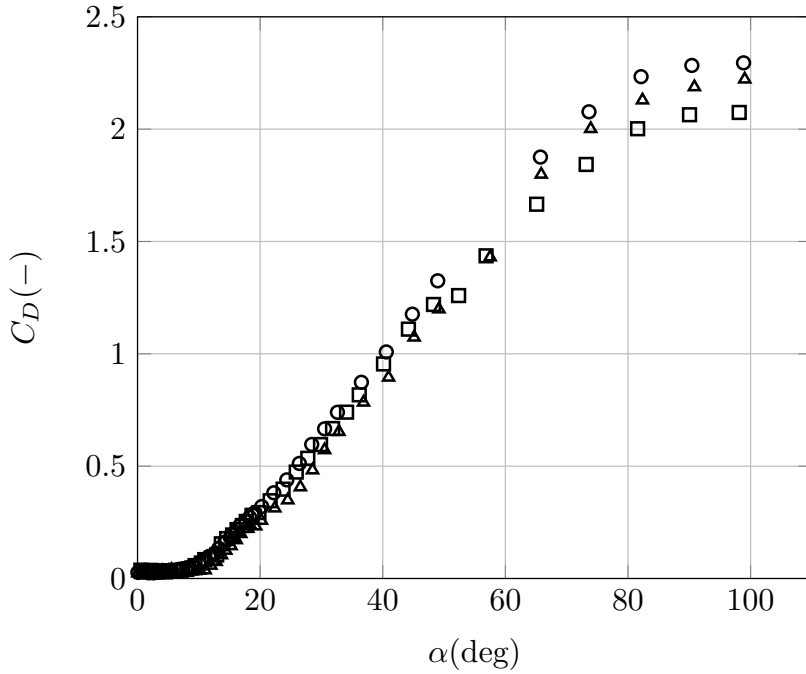


Figure 38: NACA 0018 experimental drag coefficient vs angle of attack for tripped case:
 \square $Re = 115e3$, \circ $Re = 230e3$, \triangle $Re = 290e3$

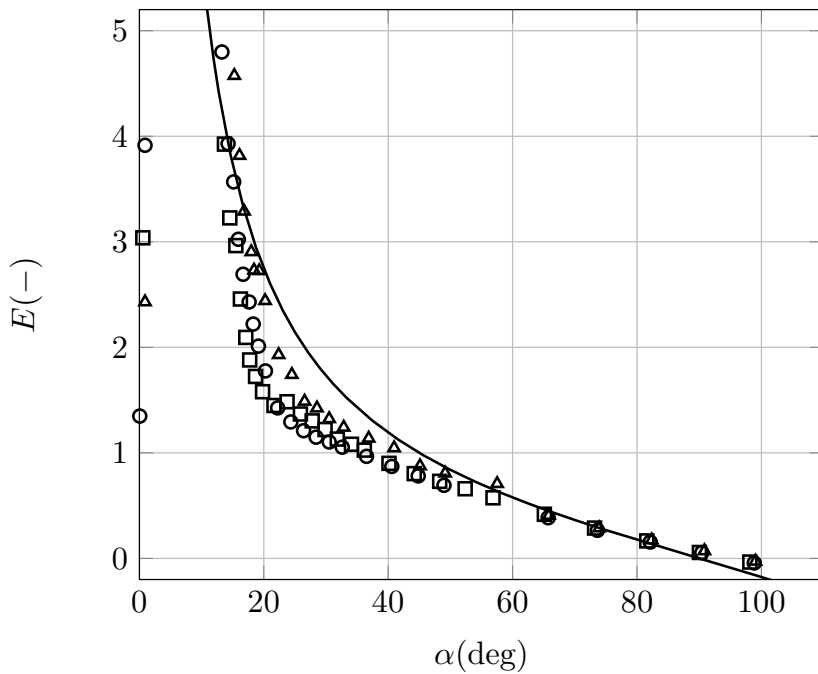


Figure 39: NACA 0018 experimental aerodynamic efficiency coefficient angle of attack for tripped case: \square $Re = 115e3$, \circ $Re = 230e3$, \triangle $Re = 290e3$, — flat plate

Roughness effect

In this paragraph the comparison of measurements in clean and tripped condition. The lift and drag coefficient distribution against angle of attack for each Reynolds number investigated are shown, respectively, in Figure 40-42-44 and 41-43-45. Naturally, the most roughness effect affected portion of these coefficient distributions is the stall onset region that exhibits a consistent reduction of maximum allowable lift coefficient. Because of no wake rake pressure measurements no drag coefficient reliable data are available for the pre-stall region from force balance measurements. However, it could be anyway inferred something about the reduction in aerodynamic efficiency due to airfoil leading edge region contamination or contour imperfections. Assuming that the airfoil maximum efficiency point - in a $\alpha - E$ plane - is generally located just before the beginning of the stall affected region, i.e. where the local slope starts to deviate consistently from the linear range value, a measure of the efficiency loss could be derived by the loss in lift coefficient in a conservative way, considering that the drag coefficient would at least only increase because of the presence of the zigzag tape. So observing Figure 40-42-44 the reduction in airfoil aerodynamic efficiency could be estimated and table summarized these values for each Reynolds number investigated.

Re	$C_L(E_{max})$ clean	$C_L(E_{max})$ tripped	$\Delta(E_{max})$ (%)
115e3	0.78	0.64	-18
230e3	0.79	0.63	-20
290e3	0.80	0.64	-20

Table 7: Estimated efficiency loss due to roughness effects for NACA 0018

This loss in aerodynamic efficiency lead to a direct loss in the allowable power coefficient as could be seen in Eq. 3.1 from [76] related to Darrieus VAWT.

$$C_P = \frac{1}{4\pi} \frac{Nc}{R} \lambda \int_0^{2\pi} \left(\frac{V}{V_\infty} \right)^2 C_L \sin \alpha \left(1 - \frac{1}{E} \arctan \alpha \right) d\phi \quad (3.1)$$

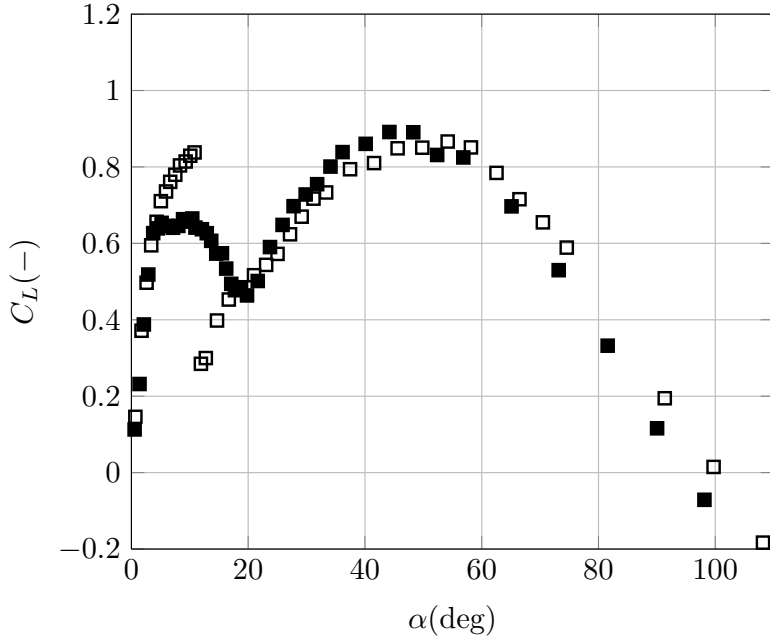


Figure 40: Comparison of lift coefficient for clean and tripped case at $Re = 115e3$: \square clean, \blacksquare tripped

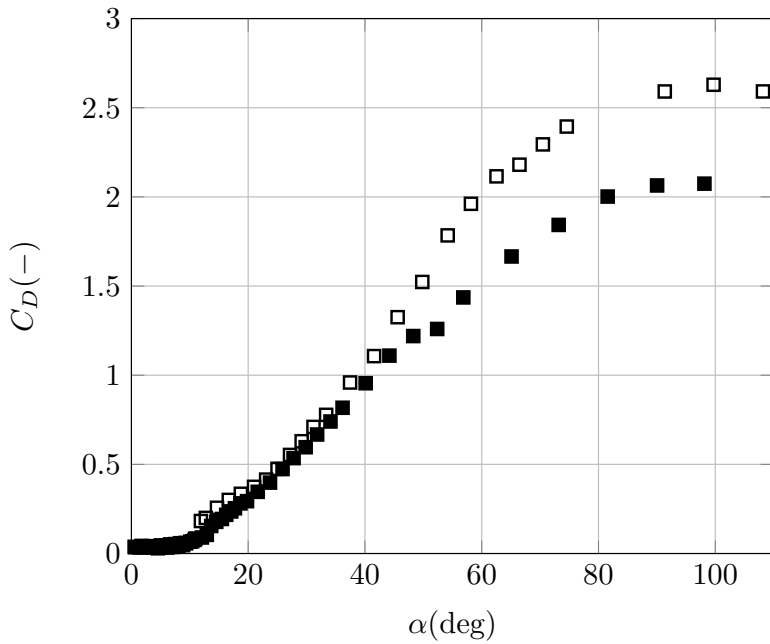


Figure 41: Comparison of drag coefficient for clean and tripped case at $Re = 115e3$: \square clean, \blacksquare tripped

RESULTS

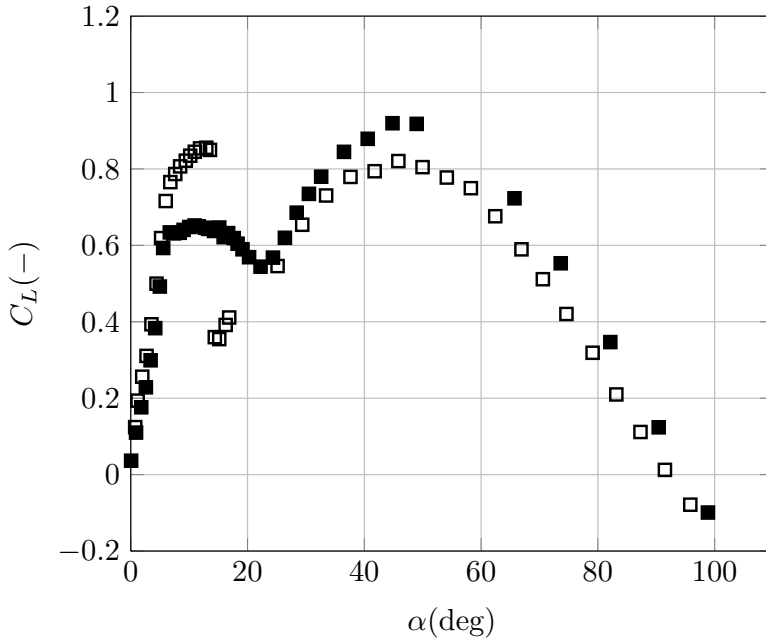


Figure 42: Comparison of lift coefficient for clean and tripped case at $Re = 230e3$: \square clean, \blacksquare tripped

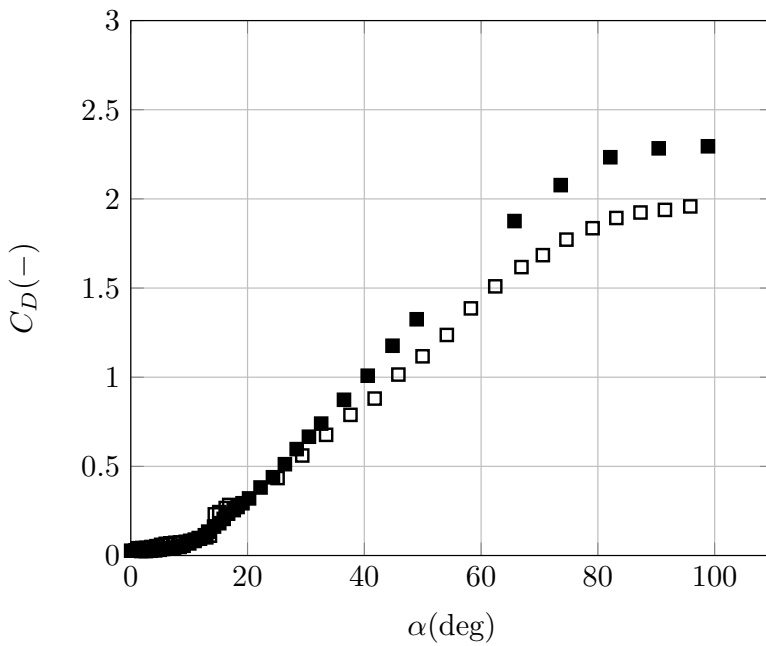


Figure 43: Comparison of drag coefficient for clean and tripped case at $Re = 230e3$: \square clean, \blacksquare tripped

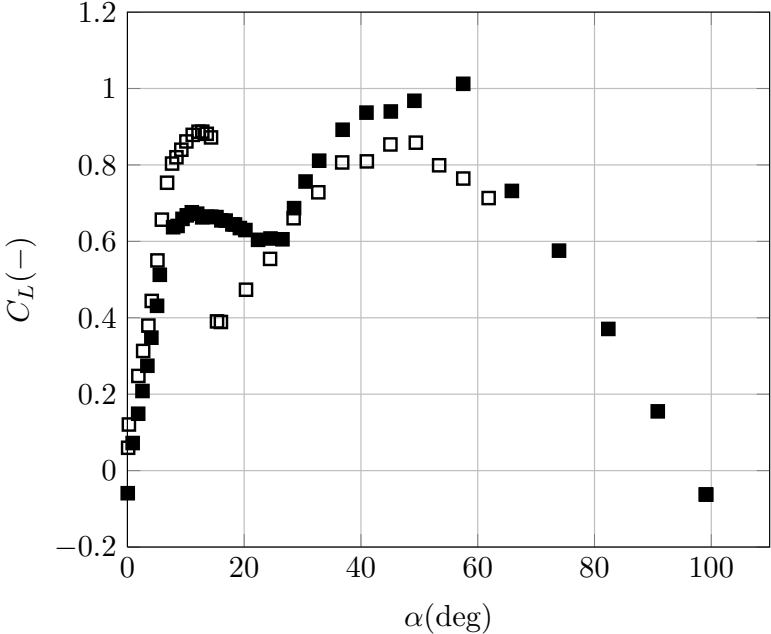


Figure 44: Comparison of lift coefficient for clean and tripped case at $Re = 290e3$: \square clean, \blacksquare tripped

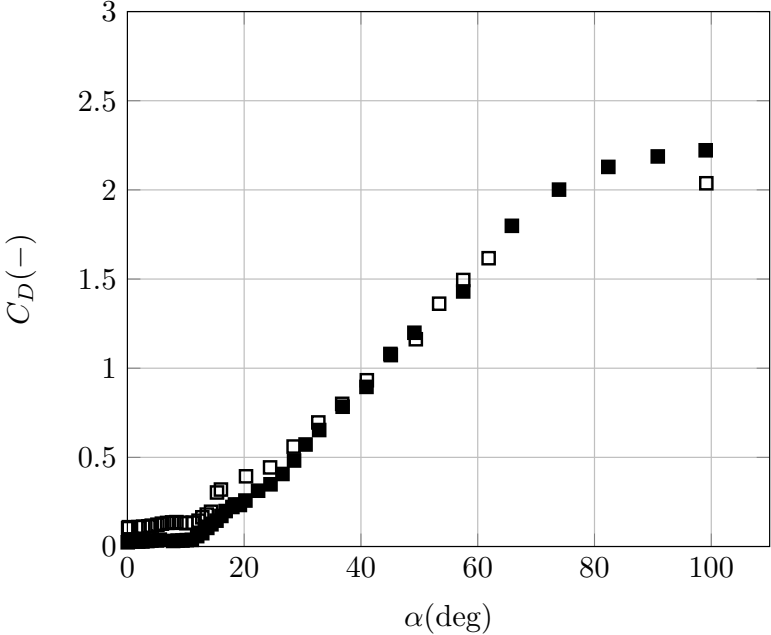


Figure 45: Comparison of drag coefficient for clean and tripped case at $Re = 290e3$: \square clean, \blacksquare tripped

3.2.2 Numerical simulations

The numerical analysis condition and specification are summarized in following tables. In both cases, respectively clean and tripped configuration, the turbulence model described in subsection 2.1.1 has been used, with turbulence intensity equal to 0.1%.

Airfoil	Trip begin	Trip length	Trip height
NACA 0018	0.1 %c	6.7 %c	0.25 mm

Table 8: Trip parameters for experiments conducted in University of Naples Federico II

Airfoil	Cells	Re	y^+	Tu_∞ (%)
NACA 0018	$107e^3$	$115 \dots 290e3$	~ 1	0.1
NACA 0018 (trip)	$86e^3$	$115 \dots 290e3$	~ 1	0.1

Table 9: Computational parameters for NACA 0018 airfoil

In Figure 46 is shown the computational grid modified in order to include the step-shaped zigzag tape promoting transition to turbulent flow whose characteristics are indicated in table 8.

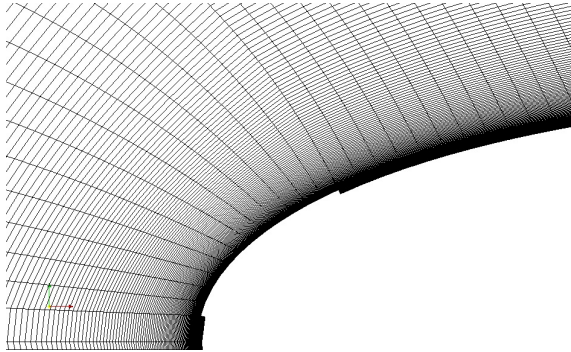


Figure 46: Trip detail in numerical grid for NACA 0018 airfoil

Free transition

In this subsection the comparison between experimental measurements and numerical simulation on NACA 0018 airfoil in clean condition are collected. In Figure 47-49-51 the lift coefficient vs against angle of attack is shown, while in Figure 48-50-52 the drag coefficient vs angle of attack is shown, for each Reynolds number investigated.

Concerning the lift coefficient, a common observation not dependent on the Reynolds number could be made: the maximum attainable lift coefficient is over-predicted by these numerics and a delayed stall onset is forecasted with a not so abrupt reduction in lift coefficient after that the maximum has been reached.

A difference in $C_{L,max}$ up to 0.1 is observed with the location of post-stall beginning again delayed up to 5 degrees. For the lower Reynolds number, the lift-curve slope at very low angle of attack is under-estimated by the numerics, as if the bubble strength would have been severely scaled down. For both Reynolds number 230e3 and 290e3 a prediction closer to experiments is performed in the linear range. The post-stall behavior ($\alpha \in [20, 40]$ deg) is well described with a difference with respect to the experiments that never exceeds 0.05. The high angle of attack regime, i.e. from 50 degrees and further on, there is a good prediction of numerics except for the lower Reynolds number, i.e. 115e3, which outlook has differences as big as 0.1 for lift coefficient, and about 5 degrees for the angle at which the lift becomes negative.

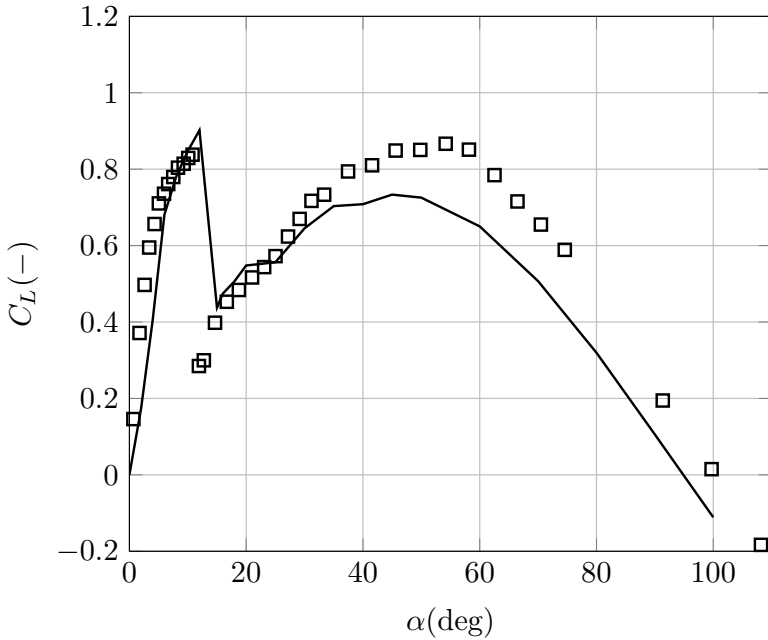


Figure 47: Comparison of lift coefficient distribution between experiments and numerical simulation at $Re = 115e3$: \square exp., — num.

RESULTS

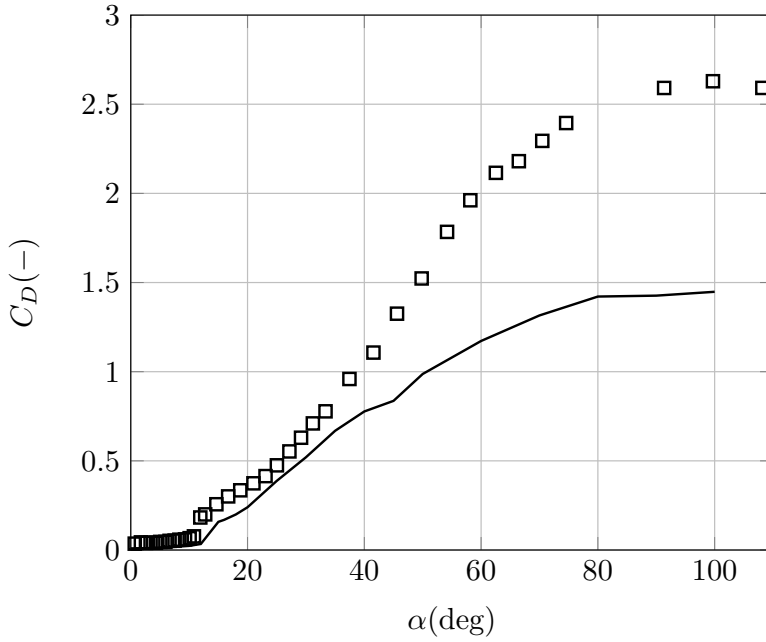


Figure 48: Comparison of drag coefficient distribution between experiments and numerical simulation at $Re = 115e3$: \square exp., — num.

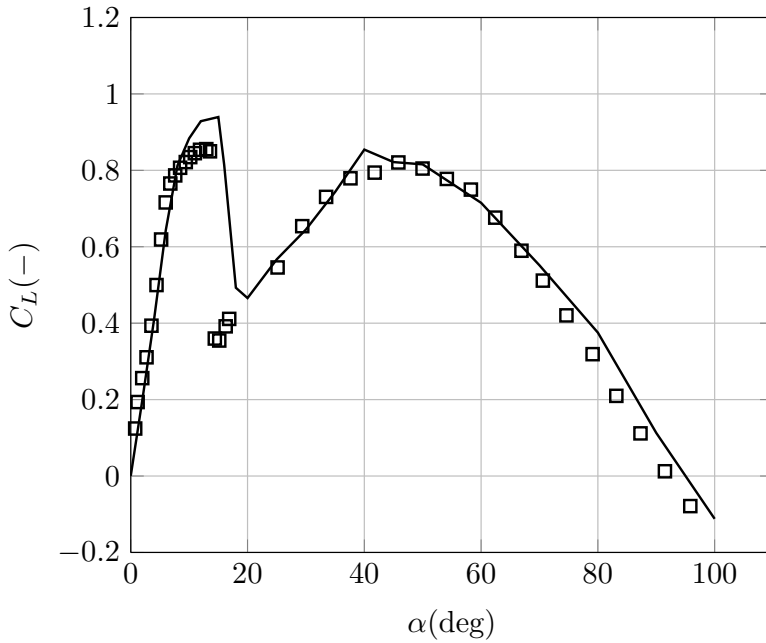


Figure 49: Comparison of lift coefficient distribution between experiments and numerical simulation at $Re = 230e3$: \square exp., — num.

Concerning the drag coefficient, no match could be found at low angle of attack ($\alpha < 20$) because of force balance based drag measurements, while the post-stall behavior is, as for the lift coefficient, well captured. Starting from $\alpha \simeq 50$ degrees and more a drastic difference is present between experiments and numerics: CFD simulations are, for both Reynolds number, agree among them in predicting a maximum drag coefficient that, from what stated by eq. 2.29 (see page 20), seems to be derived by a finite wing and not a bi-dimensional wind tunnel test.

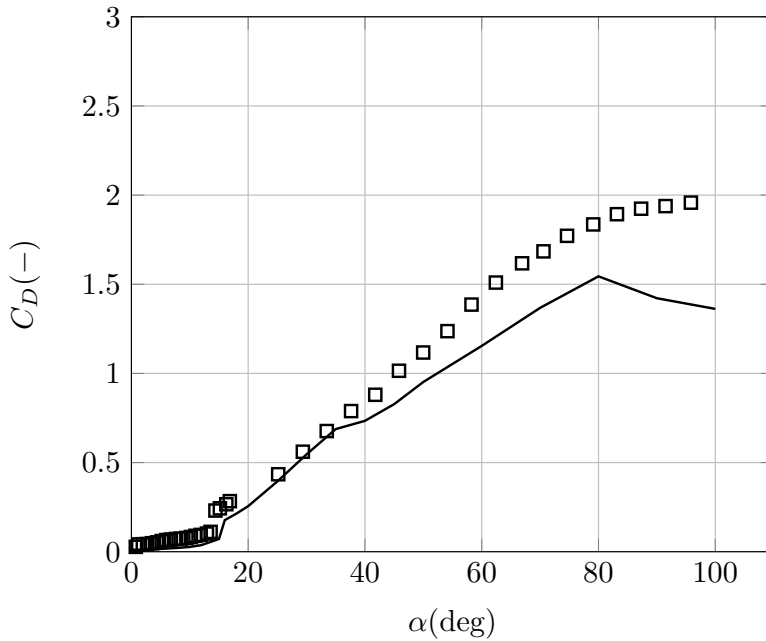


Figure 50: Comparison of drag coefficient distribution between experiments and numerical simulation at $Re = 230e3$: \square exp., — num.

RESULTS

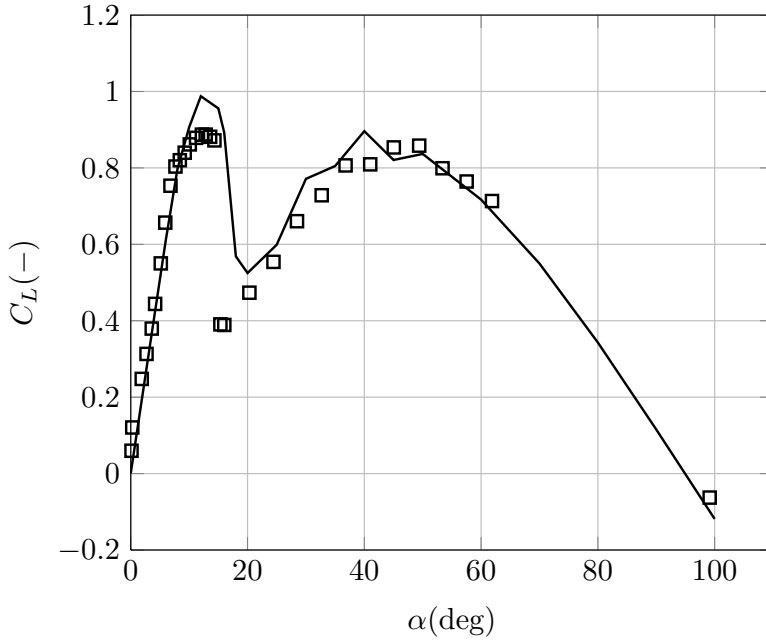


Figure 51: Comparison of lift coefficient distribution between experiments and numerical simulation at $Re = 290e3$: \square exp., — num.

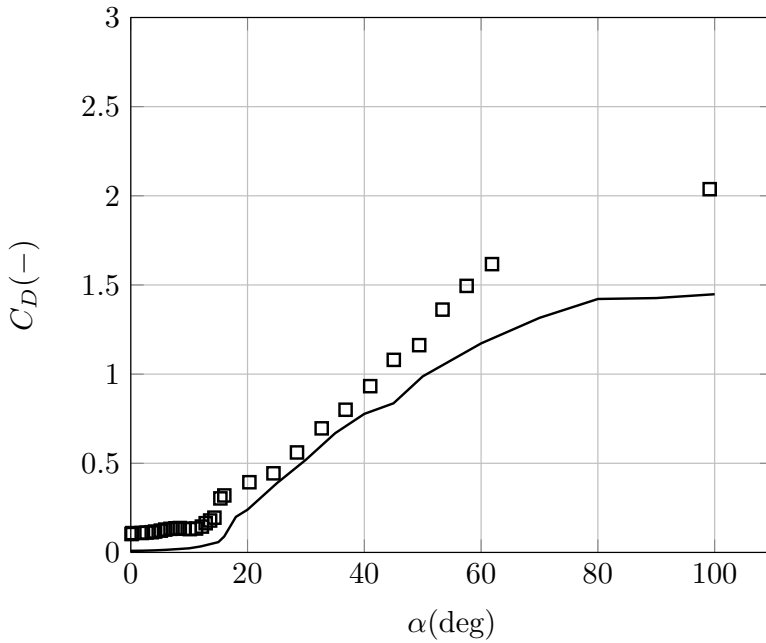


Figure 52: Comparison of drag coefficient distribution between experiments and numerical simulation at $Re = 290e3$: \square exp., — num.

Fixed transition

In this subsection the comparison between experimental measurements and numerical simulation on NACA 0018 airfoil in tripped condition are collected; the zigzag tape location and geometric detail has been given in table 8 on page 50. In Figure 53-55-57 the lift coefficient vs angle of attack is shown, while in Figure 54-56-58 the drag coefficient vs angle of attack is shown, for each Reynolds number investigated.

Concerning the lift coefficient, a common observation not dependent on the Reynolds number could be made: the maximum attainable lift coefficient is over-predicted by the numerics and a more abrupt reduction in lift coefficient, after that the maximum has been reached, is computed by the numerics, especially for the two higher Reynolds number, namely $230e3$ and $290e3$. A difference in $C_{L,max}$ up to 0.1 is observed. For the lower Reynolds number, the lift-curve slope at very low angle of attack is under-estimated by the numerics, as if the bubble strength would have been severely scaled down and still present at these angle of attack although a zigzag tape is present. For both Reynolds number $230e3$ and $290e3$ a prediction closer to experiments is performed in the linear range. The post-stall behavior ($\alpha \in [20, 40]$ deg) is well described, even if generally over-estimated, with a difference with respect to the experiments that rise up to 0.1 somewhere. The high angle of attack regime, i.e. from 50 degrees and further on, there is a good prediction of numerics.

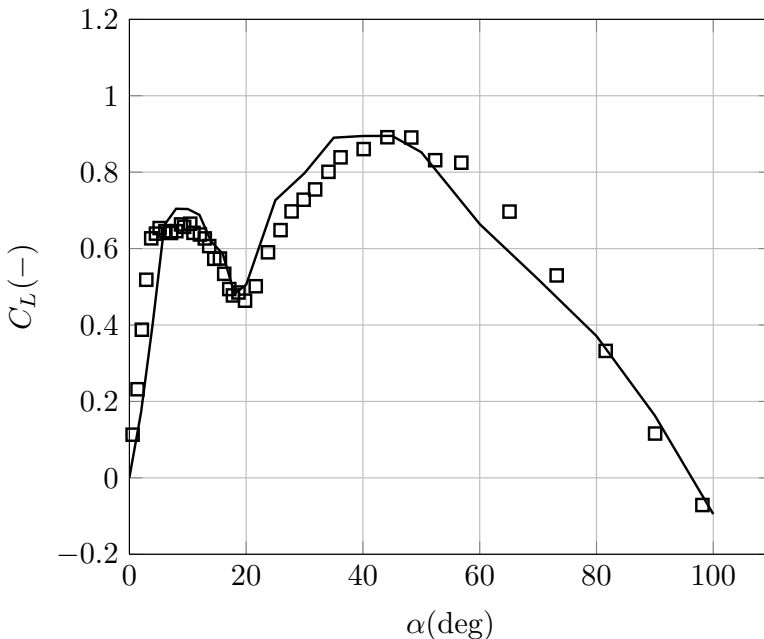


Figure 53: Comparison of lift coefficient distribution between experiments and numerical simulation at $Re = 115e3$ for tripped case: \square exp., — num.

RESULTS

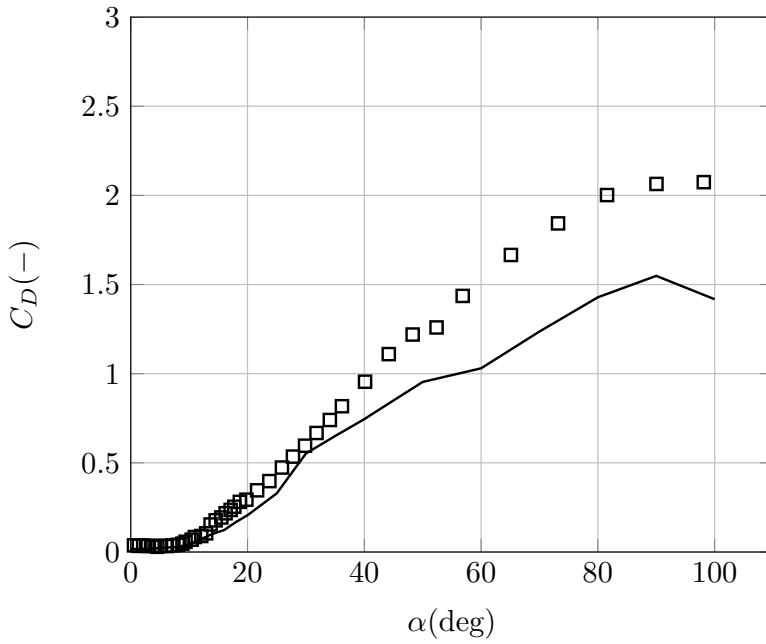


Figure 54: Comparison of drag coefficient distribution between experiments and numerical simulation at $Re = 115e3$ for tripped case: \square exp., — num.

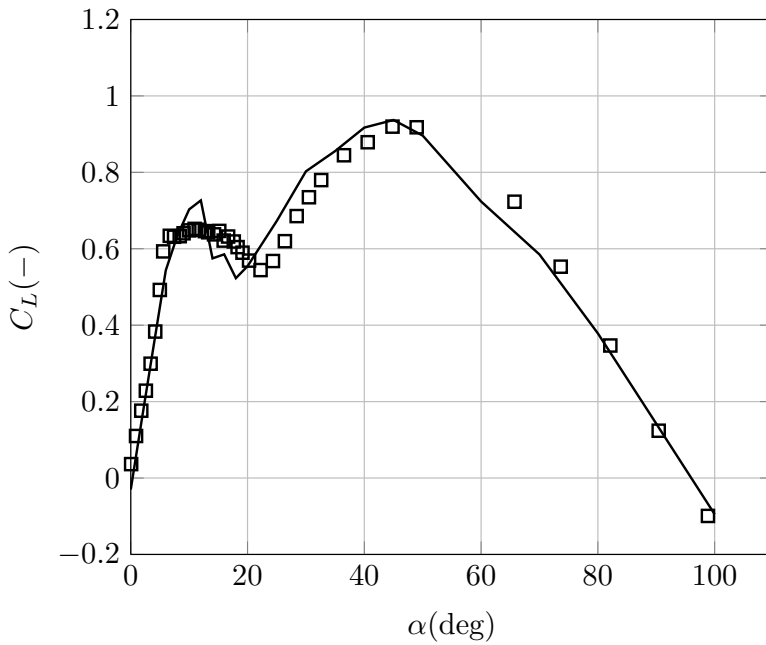


Figure 55: Comparison of lift coefficient distribution between experiments and numerical simulation at $Re = 230e3$ for tripped case: \square exp., — num.

Concerning the drag coefficient, no match could be found at low angle of attack ($\alpha < 20$) because of force balance based drag measurements, while the post-stall behavior is, as for the lift coefficient, well captured. Starting from $\alpha \simeq 50$ degrees and more a drastic difference is present between experiments and numerics: CFD simulations are, for both Reynolds number, agree among them in predicting a maximum drag coefficient that, from what stated by equation 2.29 (see page 20), seems to be derived by a finite wing and not a bi-dimensional wind tunnel test.

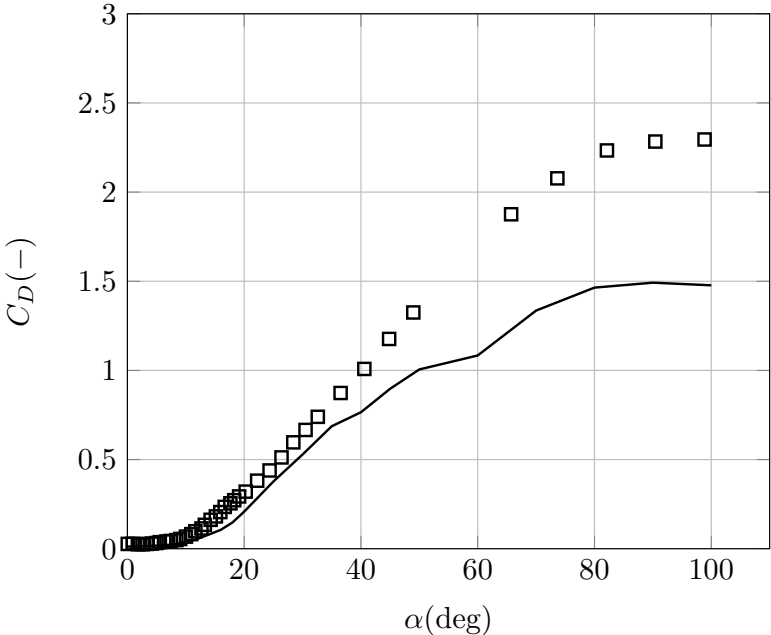


Figure 56: Comparison of drag coefficient distribution between experiments and numerical simulation at $Re = 230e3$ for tripped case: \square exp., — num.

RESULTS

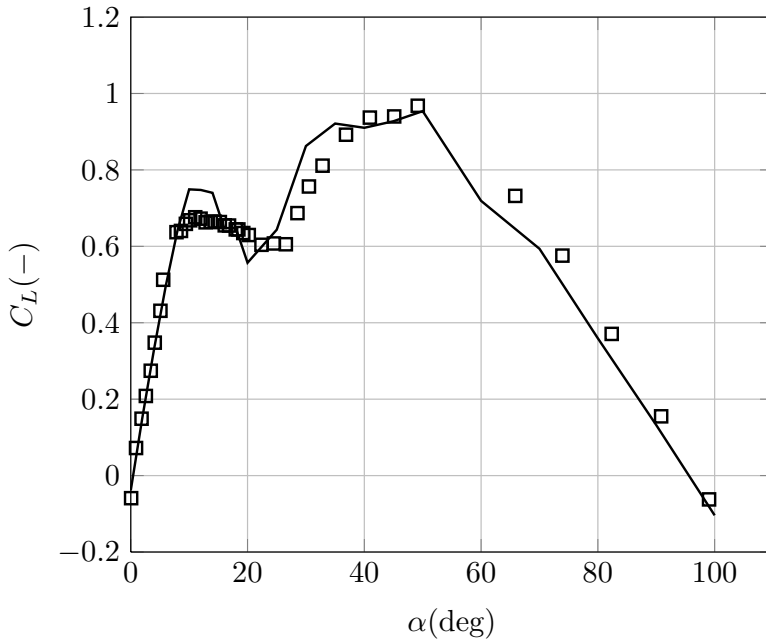


Figure 57: Comparison of lift coefficient distribution between experiments and numerical simulation at $Re = 290e3$ for tripped case: \square exp., — num.

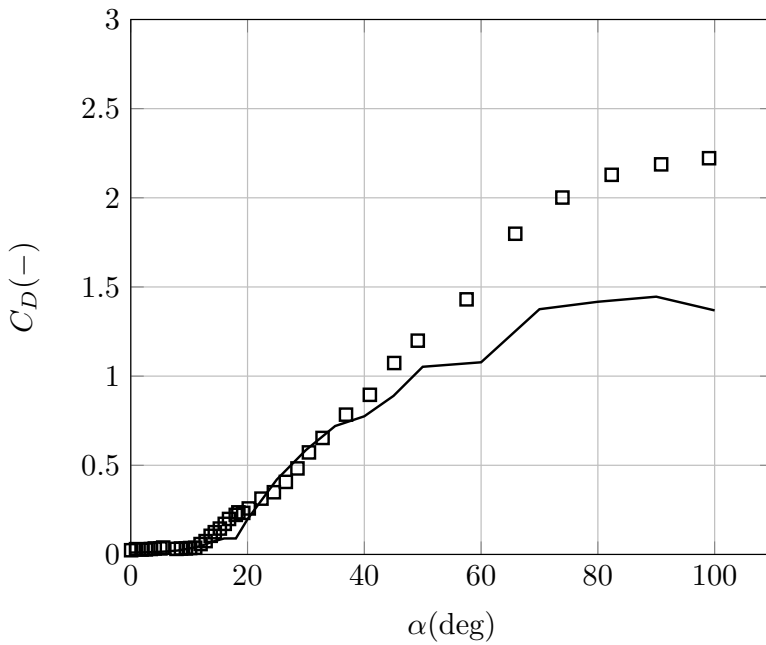


Figure 58: Comparison of drag coefficient distribution between experiments and numerical simulation at $Re = 290e3$ for tripped case: \square exp., — num.

Roughness effects

In this subsection a simple recapitulation of what already separately summarized in the previous subsections has been made in order to better exploit the roughness effects induced by the real and virtual applied zigzag tape on the airfoil leading edge region. Moreover, the differences in numerical simulations for both clean and tripped case are made more visible so that a clearer understanding of the capability of the numerical method in itself in predicting different behavior for airfoil simulated with or without a numerically step shaped zigzag tape is shown.

In Figure 59-61-63 and 60-62-64 are shown, respectively, the lift and drag coefficient for the NACA 0018 airfoil with respect to the angle of attack (AoA) for both clean and tripped condition and for the three Reynolds number investigated, namely 115e3, 230e3 and 290e3.

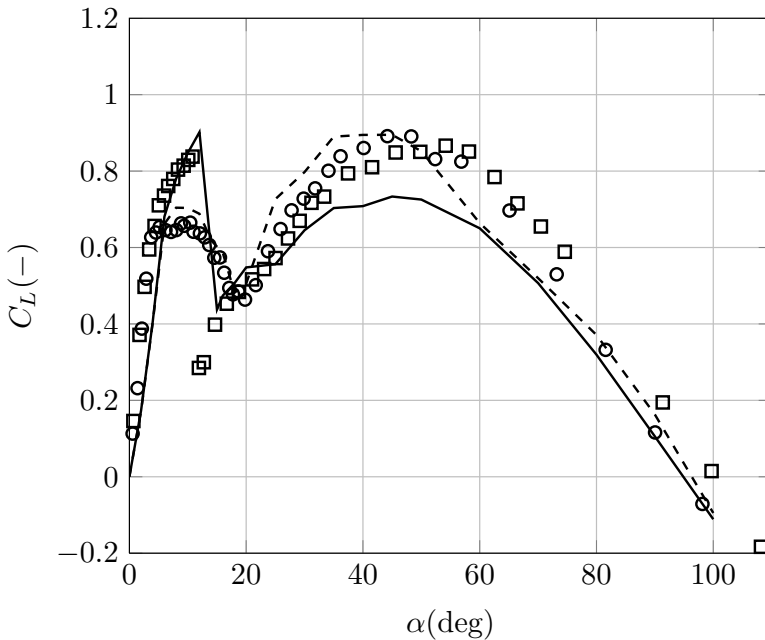


Figure 59: Comparison of lift coefficient vs AoA between experiments and numerical simulation at $Re = 115e3$ for clean and tripped case: \square exp. clean, \circ exp. tripped, — num. clean, - - num. tripped

RESULTS

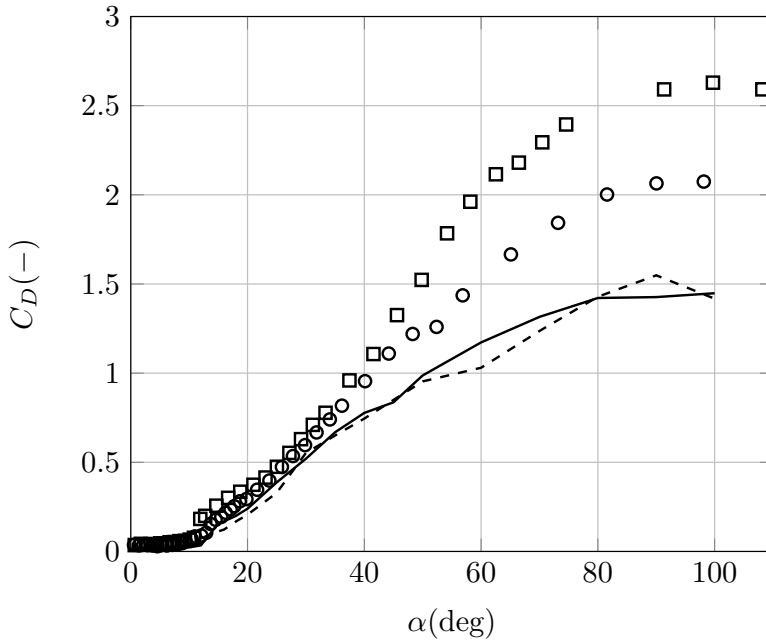


Figure 60: Comparison of drag coefficient vs AoA between experiments and numerical simulation at $Re = 115e3$ for clean and tripped case: \square exp. clean, \circ exp. tripped, — num. clean, - - num. tripped

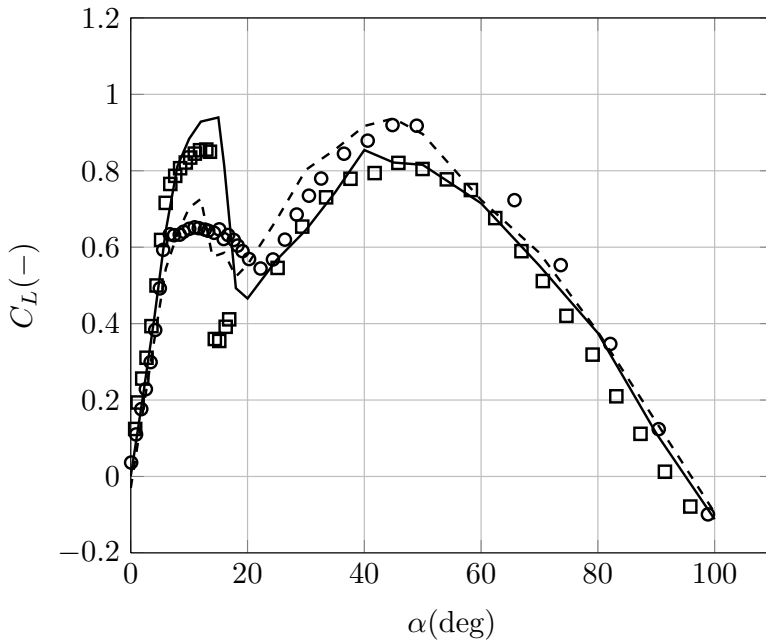


Figure 61: Comparison of lift coefficient vs AoA between experiments and numerical simulation at $Re = 230e3$ for clean and tripped case: \square exp. clean, \circ exp. tripped, — num. clean, - - num. tripped

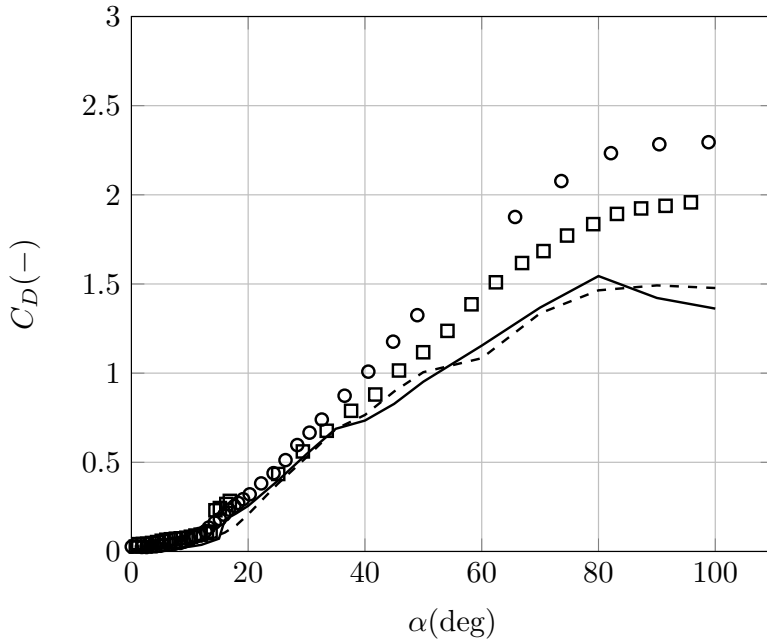


Figure 62: Comparison of drag coefficient vs AoA between experiments and numerical simulation at $Re = 230e3$ for clean and tripped case: \square exp. clean, \circ exp. tripped, — num. clean, - - num. tripped

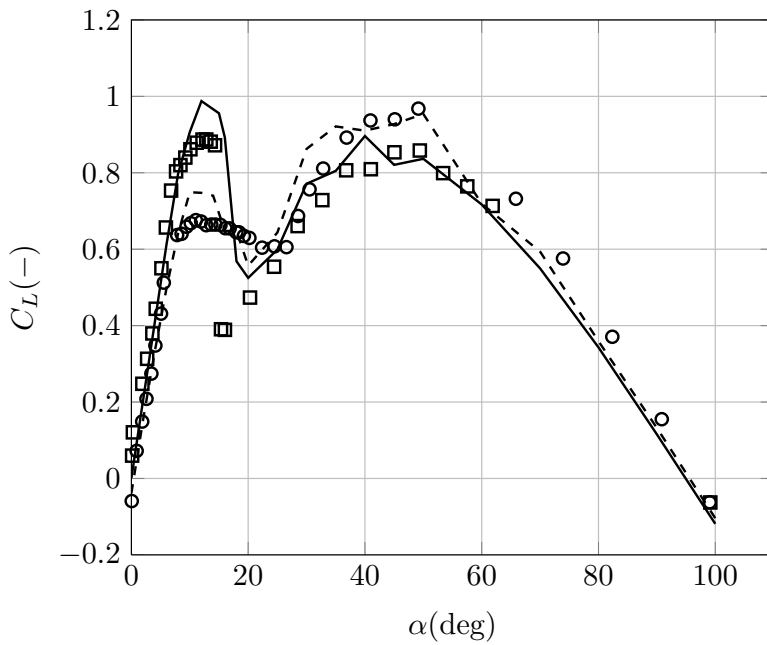


Figure 63: Comparison of lift coefficient vs AoA between experiments and numerical simulation at $Re = 290e3$ for clean and tripped case: \square exp. clean, \circ exp. tripped, — num. clean, - - num. tripped

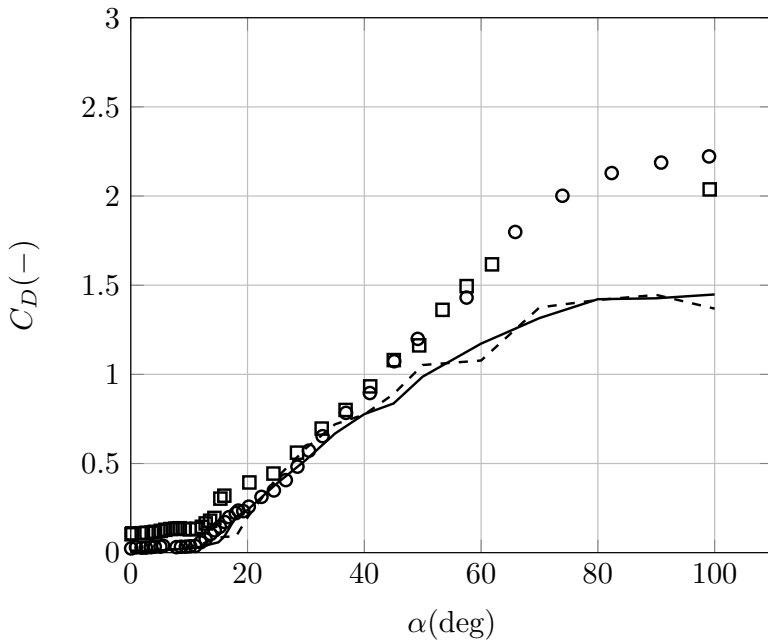


Figure 64: Comparison of drag coefficient vs AoA between experiments and numerical simulation at $Re = 290e3$ for clean and tripped case: \square exp. clean, \circ exp. tripped, — num. clean, - - num. tripped

NACA 0018 synoptic table

In this paragraph a synoptic table for the NACA 0018 airfoil is presented in order to summarize the main aerodynamic characteristics for both clean and tripped condition derived from a comparison between experimental measurements and numerical analysis. It is important to underline that the numerical simulations are performed between 0 and 20 degrees with a sample every 2 degrees, while between 20 and 50 degrees with a sample every 5 degrees, and finally between 50 and 100 degrees with a sample every 10 degrees, thus having a sampling very different from the experiments. As already discussed in Section 2.3, having the drag coefficient evaluated by means of force balance there is no proper meaning in the derivation of the aerodynamic efficiency from experiments, thus only the numerical value should be taken into account and no difference between the two is made available.

Parameter	Re = 115e3				Re = 230e3				Re = 290e3			
	Exp.	Num.	$\Delta(\%)$		Exp.	Num.	$\Delta(\%)$		Exp.	Num.	$\Delta(\%)$	
α_{0L} (deg)	0	0	0		0	0	0		0	0	0	
$C_{L,\alpha}$ (deg ⁻¹)	0.1450	0.1165	-24		0.1227	0.1164	+5.1		0.1090	0.1016	-6.7	
E_{max} (-)	16.1007	46.6438	n.a.		11.1915	37.4424	n.a.		6.5864	42.4149	n.a.	
$\alpha_{E_{max}}$ (deg)	5.9	6	n.a.		6.8	8	n.a.		10.1	8	n.a.	
$C_{L,max}$ (-)	0.8379	0.9019	+7.1		0.8555	0.9395	+9.8		0.8871	0.9867	+11	
$\alpha_{C_{L,max}}$ (deg)	10.8	12	+10		12.9	15	+16		12.8	12	-6.2	
α_{0L} (deg)	0	0	0		0	0	0		0	0	0	
$C_{L,\alpha}$ (deg ⁻¹)	0.1412	0.1162	-18		0.0875	0.0952	+8.8		0.0858	0.0825	-3.8	
E_{max} (-)	21.7415	27.1270	n.a.		16.1168	28.1710	n.a.		20.4167	29.9277	n.a.	
$\alpha_{E_{max}}$ (deg)	5.4	6	n.a.		5.5	6	n.a.		7.8	6	n.a.	
$C_{L,max}$ (-)	0.6651	0.7042	+5.8		0.6520	0.7265	+11		0.6761	0.7491	+11	
$\alpha_{C_{L,max}}$ (deg)	10.4	8	-23		10.9	12	+10		11	10	-9.1	

Table 10: NACA 0018 synoptic table for aerodynamic characteristics

3.2.3 Post-stall modelling

In this subsection a comparison of the prediction that based on experiments could be carried out using both the two semi-empirical post-stall models described in 2.2 is performed. The comparisons are based on both clean and tripped conditions. The Viterna-Corrigan model is applied in three different ways:

1. attaching the extrapolation at the maximum lift coefficient point, as stated by Viterna in his first proposal [78] (indicated as – – VC up in the following figures);
2. attaching the extrapolation at the lift coefficient before the beginning of the ascending post-stall region, as suggested by Viterna itself in a second proposal (indicated as – – VC low in the following figures);
3. attaching the extrapolation at the angle of attack that match the theoretical flat plate aerodynamic efficiency value, as suggested by Tangler [73] (indicated as – · – VC f.p. in the following figures).

No particular arrangements are made to the AERODAS model that is used in its own original fashion. For both semi-empirical models a sensitivity analysis with respect to the aspect ratio, AR, has been conducted. Firstly, a 2D version is proposed, imposing in eq. 2.29 on 20 an aspect ratio equal to 50. Secondly, a tested model geometric aspect ratio based value is analysis is performed, that in this case is equal to 10, having the span to chord ratio equal to 10. Finally, an intermediate aspect ratio equal to 30 is used, in order to understand if an assumption of partly dependent on finiteness effect for lift coefficient distribution would better fit the experimental measurements.

Free transition

In Figure 65-66-67 the post-stall semi-empirical models are applied to lift coefficient vs AoA with an aspect ratio equal to 50 assuming a fully 2D wind tunnel test condition. In Figure 68-69-70 the post-stall semi-empirical models are applied to lift coefficient vs AoA with an aspect ratio equal to 10 assuming the finiteness to be related to the sole geometrical parameter of the tested model. In Figure 71-72-73 the post-stall semi-empirical models are applied to lift coefficient vs AoA with an aspect ratio equal to 30 assuming the finiteness to be related to an intermediate value between a fully 2D and the real geometric aspect ratio of the model.

The main indication is that when experimental data are available up to and just after stall onset is extremely important to use the second proposal of those enumerate on page 65, i. e. attach the extrapolation after the stall, at least for clean condition and Reynolds number as low as those here investigated for which the effects of laminar bubble on the abrupt reduction in lift coefficient at stall are so strong.

For $AR = 50$, i. e. a 2D assumption, a general over-estimation in lift coefficient secondary peak occurs; conversely using $AR = 10$ a general under-estimation is observed. The choice of an intermediate value for the aspect ratio, in this case equal to 30 exhibits a better fitting to the experimental measurements carried out within this study.

RESULTS

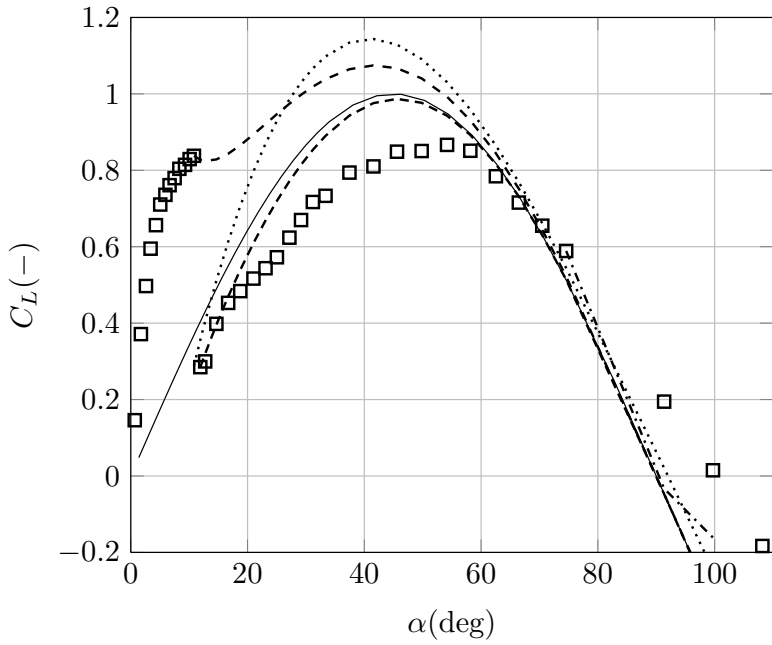


Figure 65: NACA 0018 comparison of lift coefficient vs AoA for experiments and post-stall model at $Re = 115e3$ with $AR = 50$ for clean condition: \square exp., — Flat Plate, - - VC up, - · - VC low, · · · VC f.p., · · · AERODAS

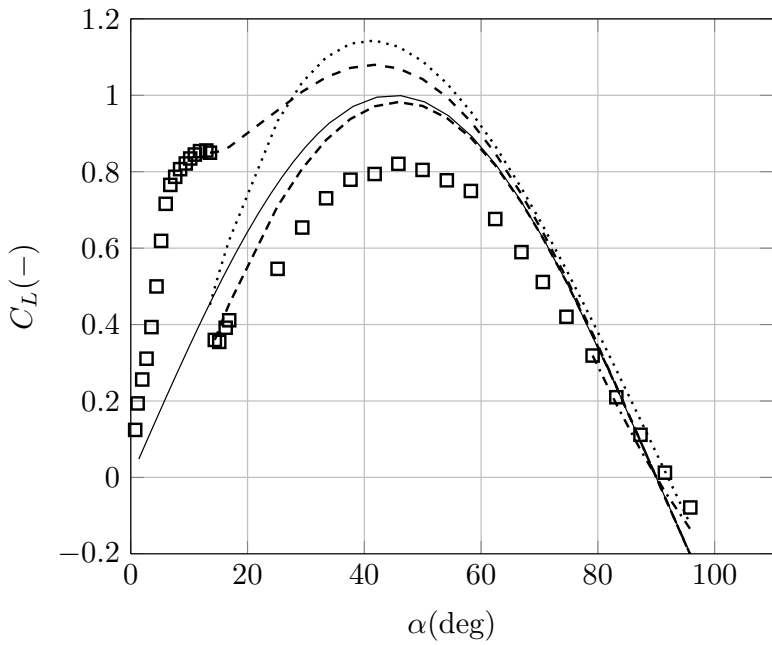


Figure 66: NACA 0018 comparison of lift coefficient vs AoA for experiments and post-stall model at $Re = 230e3$ with $AR = 50$ for clean condition: \square exp., — Flat Plate, - - VC up, - · - VC low, · · · VC f.p., · · · AERODAS

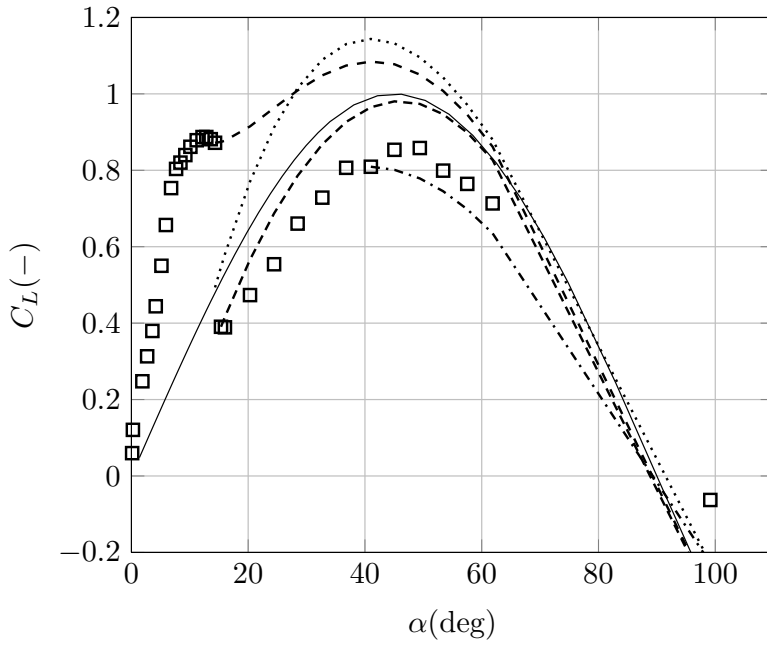


Figure 67: NACA 0018 comparison of lift coefficient vs AoA for experiments and post-stall model at $Re = 290e3$ with $AR = 50$ for clean condition: \square exp., — Flat Plate, - - VC up, - · - VC low, · · · VC f.p., · · · AERODAS

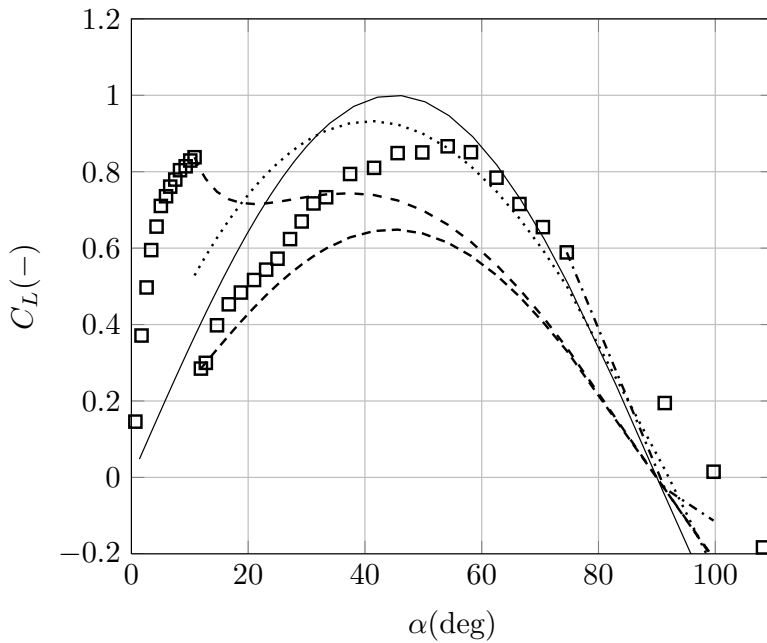


Figure 68: NACA 0018 comparison of lift coefficient vs AoA for experiments and post-stall model at $Re = 115e3$ with $AR = 10$ for clean condition: \square exp., — Flat Plate, - - VC up, - · - VC low, · · · VC f.p., · · · AERODAS

RESULTS

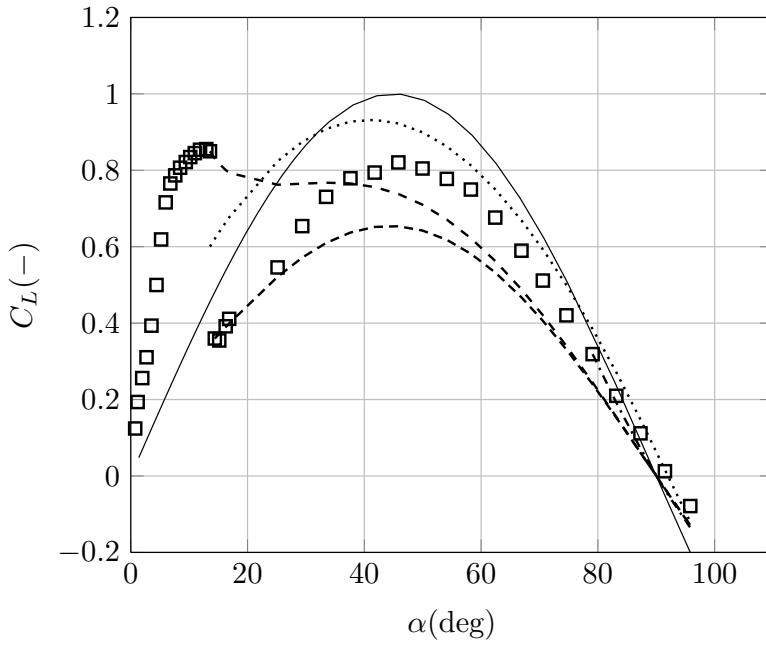


Figure 69: NACA 0018 comparison of lift coefficient vs AoA for experiments and post-stall model at $Re = 230e3$ with $AR = 10$ for clean condition: \square exp., — Flat Plate, - - VC up, - · - VC low, · · · VC f.p., · · · AERODAS

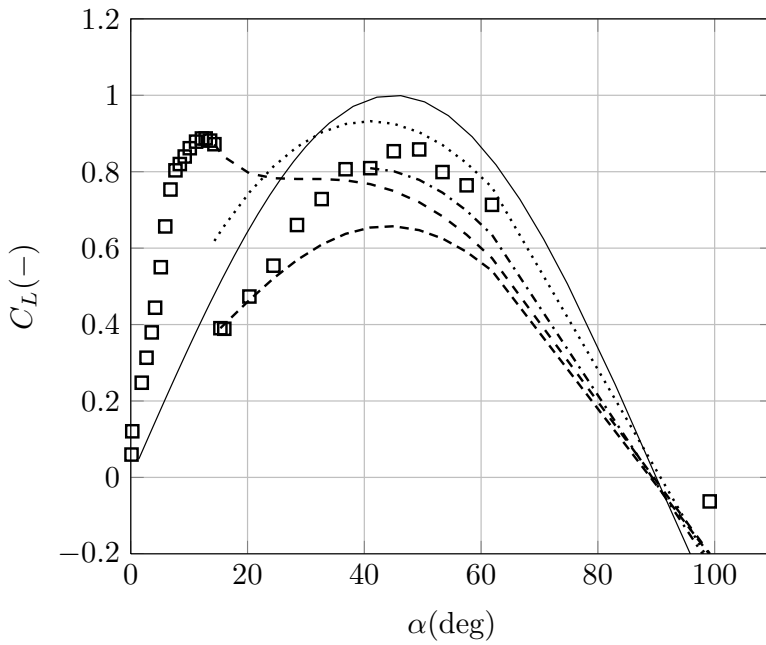


Figure 70: NACA 0018 comparison of lift coefficient vs AoA for experiments and post-stall model at $Re = 290e3$ with $AR = 10$ for clean condition: \square exp., — Flat Plate, - - VC up, - · - VC low, · · · VC f.p., · · · AERODAS

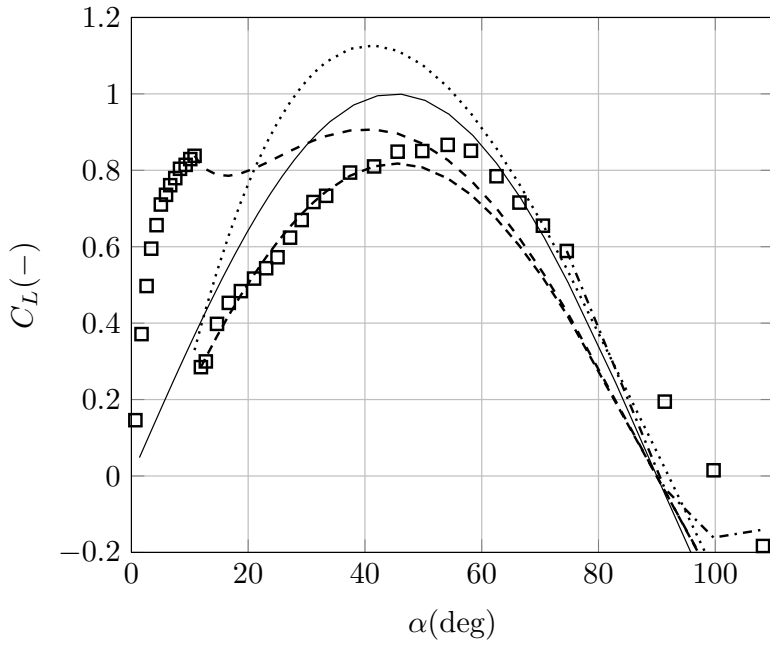


Figure 71: NACA 0018 comparison of lift coefficient vs AoA for experiments and post-stall model at $Re = 115e3$ with $AR = 30$ for clean condition: \square exp., — Flat Plate, - - VC up, -·- VC low, ··· VC f.p., ··· AERODAS

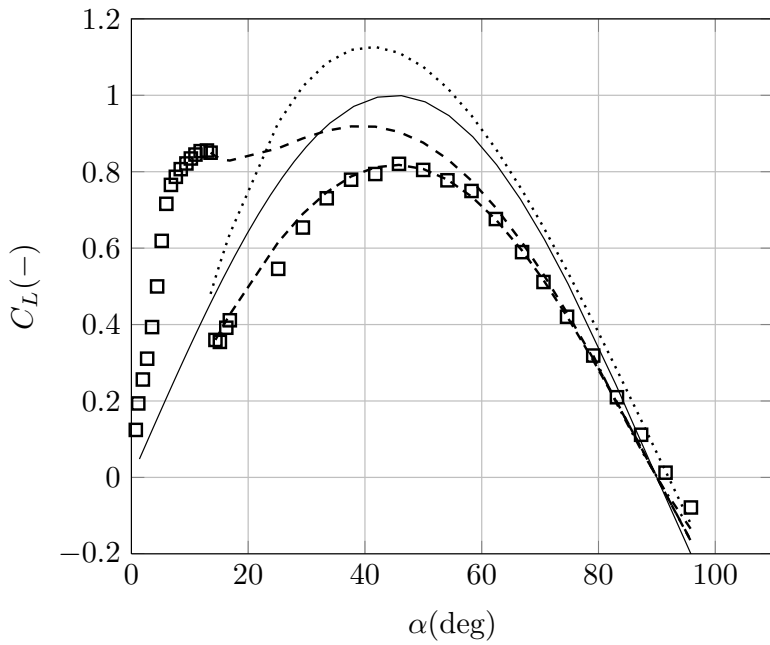


Figure 72: NACA 0018 comparison of lift coefficient vs AoA for experiments and post-stall model at $Re = 230e3$ with $AR = 30$ for clean condition: \square exp., — Flat Plate, - - VC up, -·- VC low, ··· VC f.p., ··· AERODAS

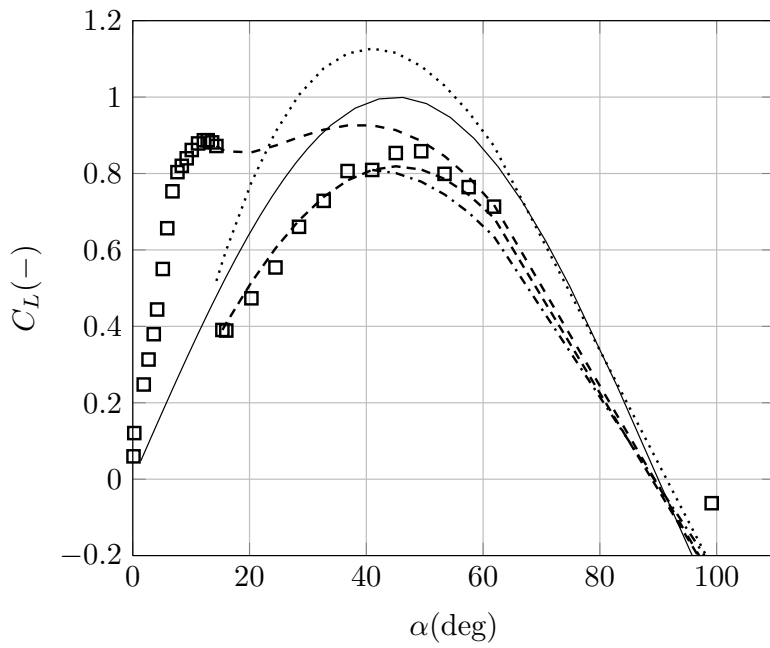


Figure 73: NACA 0018 comparison of lift coefficient vs AoA for experiments and post-stall model at $Re = 290e3$ with $AR = 30$ for clean condition: \square exp., — Flat Plate, --- VC up, -.- VC low, ··· VC f.p., ··· AERODAS

In Figure 74-75-76, 77-78-79 and 80-81-82 the post-stall semi-empirical models are applied to drag coefficient vs AoA with an aspect ratio, respectively, equal to 50, 10 and 30.

The post-stall modelling for the drag coefficient exhibits a far different behavior. Conversely from the lift coefficient vs AoA, in this case considering an aspect ratio different from that of 2D assumptions (i. e. 50), the match between experiments and modelling gives a general under-estimation of the high angle of attack region up to 90 degrees. Again here for drag coefficient, the better proposal among the three of page 65 remains the second, mostly because of the laminar bucket.

The third assumption of 65 undergoes to an ill posed extrapolation for the lower Reynolds number, i. e. $150e3$, because of the attachment point, that for the aerodynamic efficiency to be equal to that of the theoretical flat plate lies about 70 degrees, to have a drag coefficient higher than the maximum allowable from Viterna-Corrigan model equation 2.29, i. e. 2.

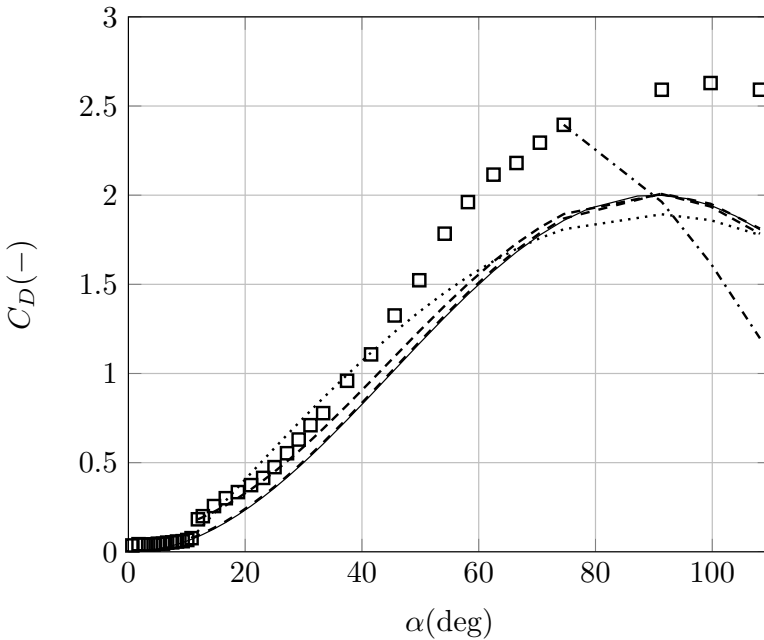


Figure 74: NACA 0018 comparison of drag coefficient vs AoA for experiments and post-stall model at $Re = 115e3$ with $AR = 50$ for clean condition: \square exp., — Flat Plate, - - VC up, - - VC low, - · - VC f.p., ··· AERODAS

RESULTS

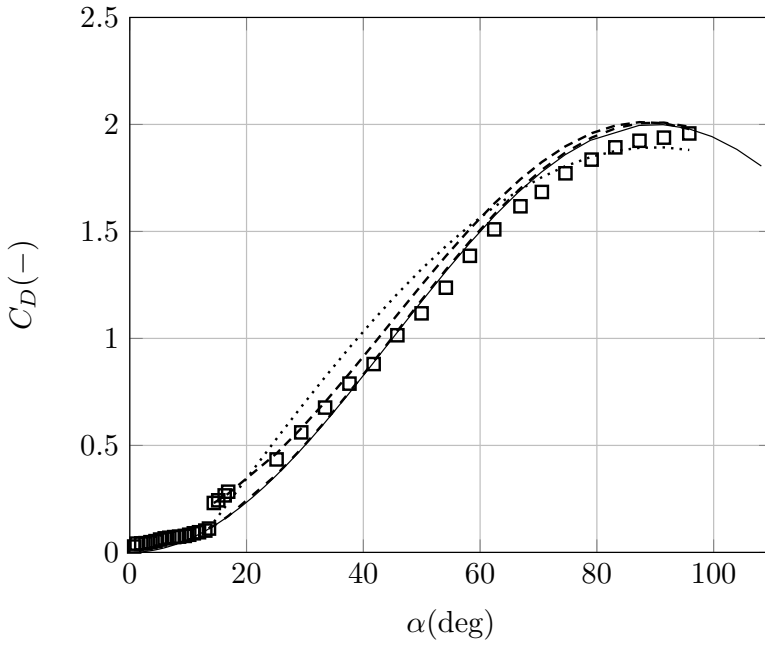


Figure 75: NACA 0018 comparison of drag coefficient vs AoA for experiments and post-stall model at $Re = 230e3$ with $AR = 50$ for clean condition: \square exp., — Flat Plate, - - VC up, - · - VC low, · · · VC f.p., · · · AERODAS

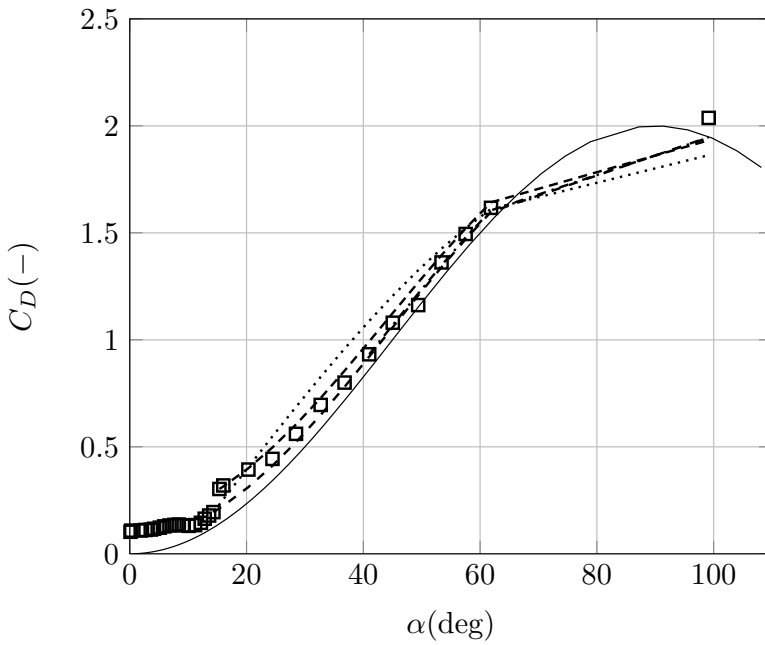


Figure 76: NACA 0018 comparison of drag coefficient vs AoA for experiments and post-stall model at $Re = 290e3$ with $AR = 50$ for clean condition: \square exp., — Flat Plate, - - VC up, - · - VC low, · · · VC f.p., · · · AERODAS

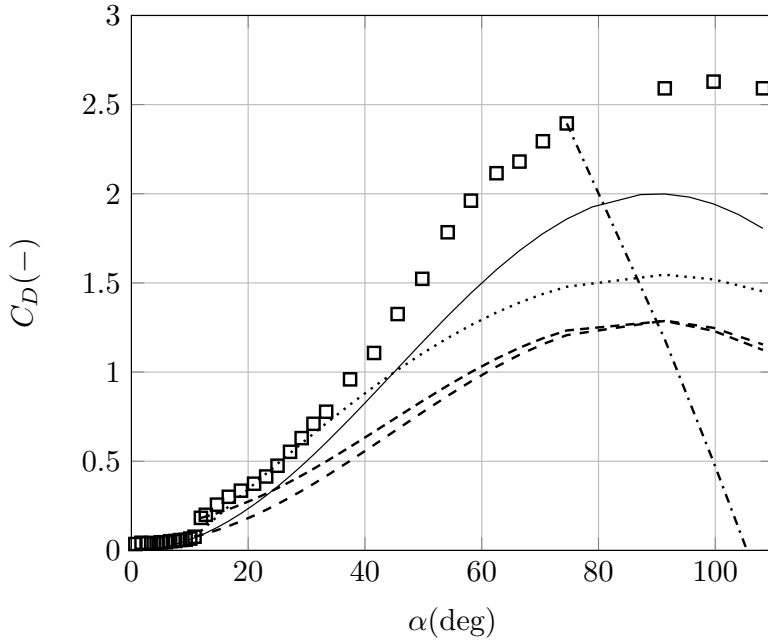


Figure 77: NACA 0018 comparison of drag coefficient vs AoA for experiments and post-stall model at $Re = 115e3$ with $AR = 10$ for clean condition: \square exp., — Flat Plate, - - VC up, - · - VC low, · · · VC f.p., · · · AERODAS

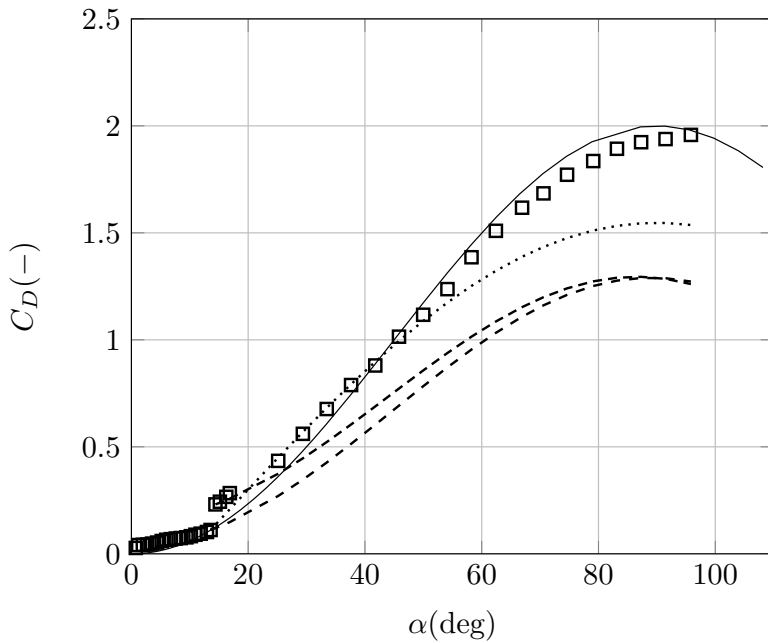


Figure 78: NACA 0018 comparison of drag coefficient vs AoA for experiments and post-stall model at $Re = 230e3$ with $AR = 10$ for clean condition: \square exp., — Flat Plate, - - VC up, - · - VC low, · · · VC f.p., · · · AERODAS

RESULTS

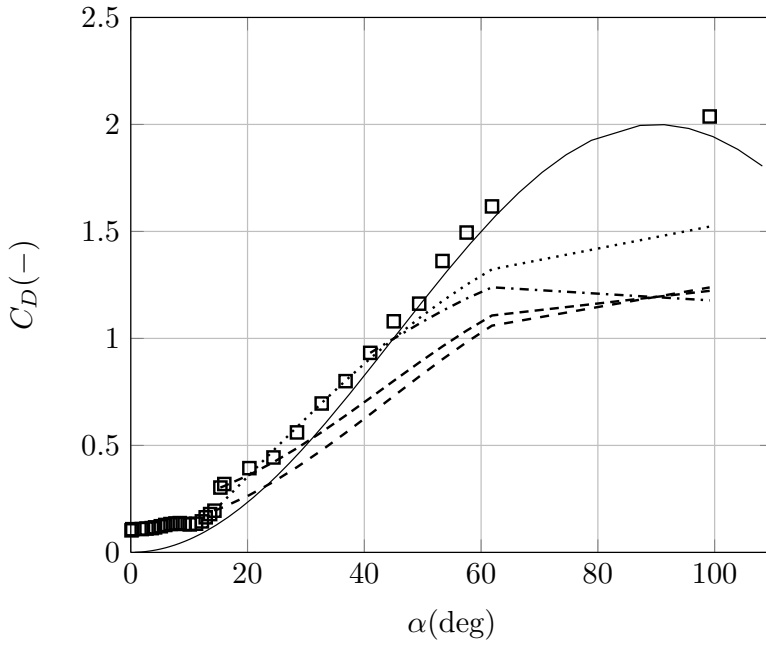


Figure 79: NACA 0018 comparison of drag coefficient vs AoA for experiments and post-stall model at $Re = 290e3$ with $AR = 10$ for clean condition: \square exp., — Flat Plate, - - VC up, - · - VC low, - · · - VC f.p., · · · AERODAS

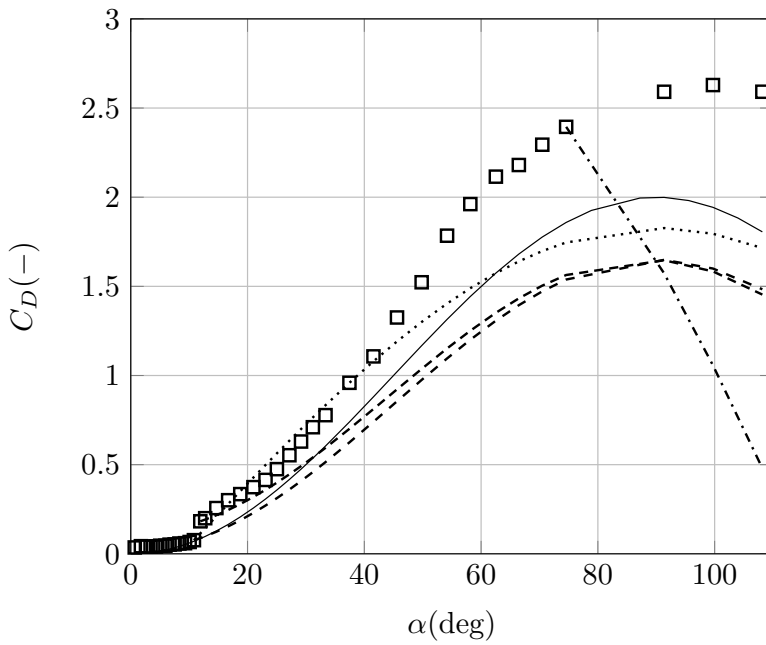


Figure 80: NACA 0018 comparison of drag coefficient vs AoA for experiments and post-stall model at $Re = 115e3$ with $AR = 30$ for clean condition: \square exp., — Flat Plate, - - VC up, - · - VC low, - · · - VC f.p., · · · AERODAS

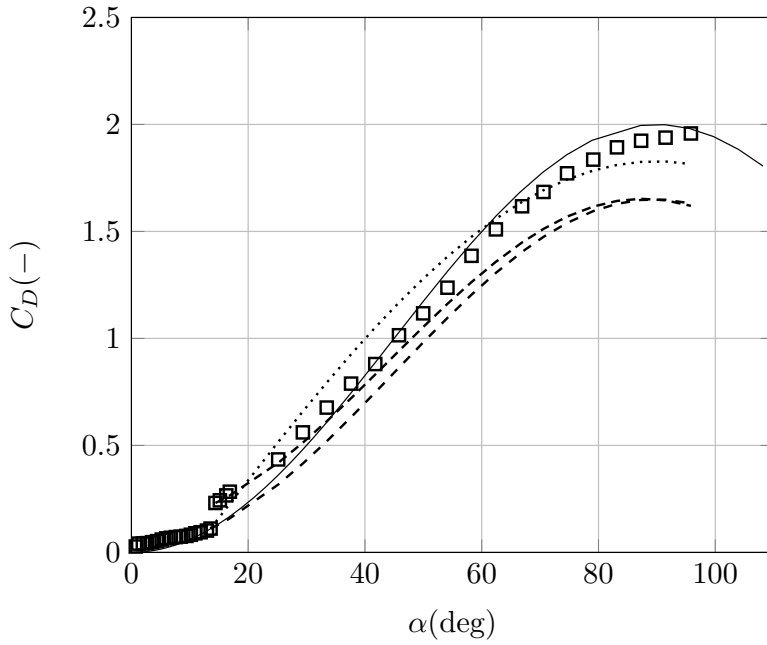


Figure 81: NACA 0018 comparison of drag coefficient vs AoA for experiments and post-stall model at $Re = 230e3$ with $AR = 30$ for clean condition: \square exp., — Flat Plate, - - VC up, - · - VC low, · · · VC f.p., · · · AERODAS

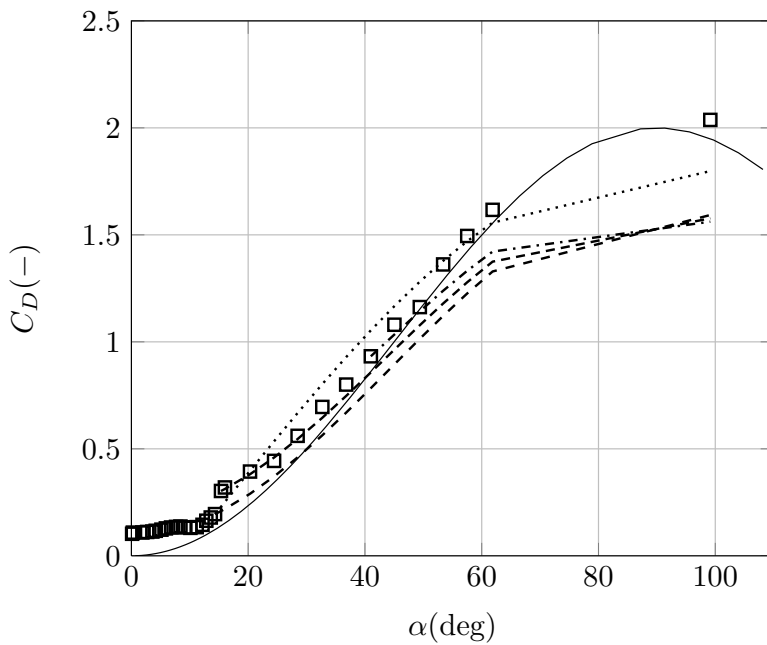


Figure 82: NACA 0018 comparison of drag coefficient vs AoA for experiments and post-stall model at $Re = 290e3$ with $AR = 30$ for clean condition: \square exp., — Flat Plate, - - VC up, - · - VC low, · · · VC f.p., · · · AERODAS

Fixed transition

In Figure 83-84-85, 86-87-88 and 89-90-91 the post-stall semi empirical models are applied to lift coefficient vs AoA with an aspect ratio, respectively, equal to 50, 10 and 30.

The main indication is that when experimental data are available up to and just after stall onset is extremely important to use the second proposal of those enumerate on page 65, i.e. attach the extrapolation after the stall, also in case of forced transition by use of zigzag tape on leading edge because of the persistent not negligible difference between maximum lift coefficient and the post-stall recovery value.

For $AR = 50$, i.e. a 2D assumption, a good estimation in lift coefficient secondary peak occurs; conversely using $AR = 10$ a general under-estimation is observed. The choice of an intermediate value for the aspect ratio, in this case equal to 30 exhibits in case of tripped condition a worse fitting to the experimental measurements with respect to the 2D value.

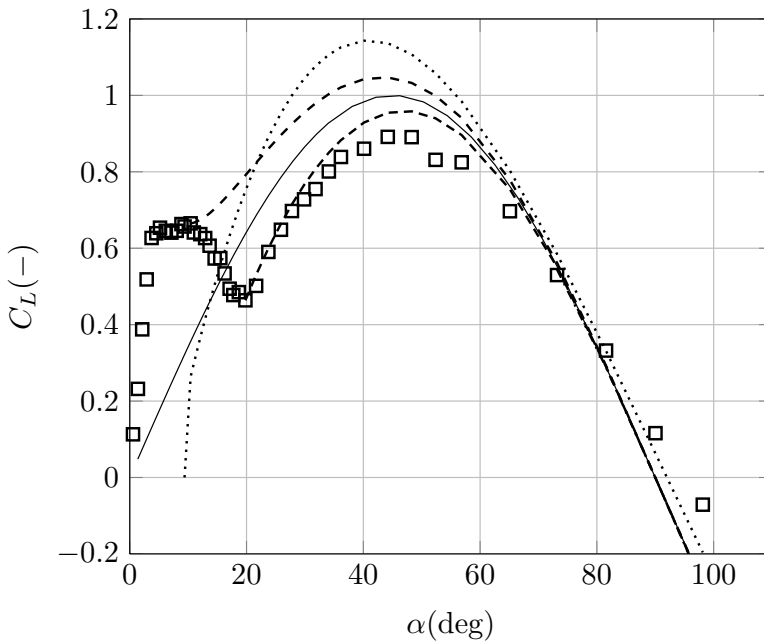


Figure 83: NACA 0018 comparison of lift coefficient vs AoA for experiments and post-stall model at $Re = 115e3$ with $AR = 50$ for tripped condition: \square exp., — Flat Plate, - - VC up, -- VC low, - · - VC f.p., ··· AERODAS

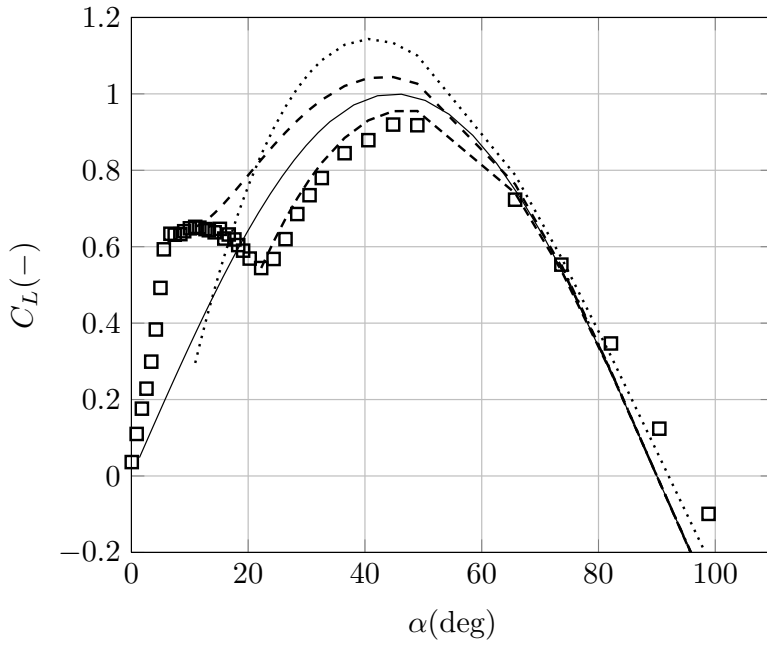


Figure 84: NACA 0018 comparison of lift coefficient vs AoA for experiments and post-stall model at $Re = 230e3$ with $AR = 50$ for tripped condition: \square exp., — Flat Plate, - - VC up, - · - VC low, · · - VC f.p., ··· AERODAS

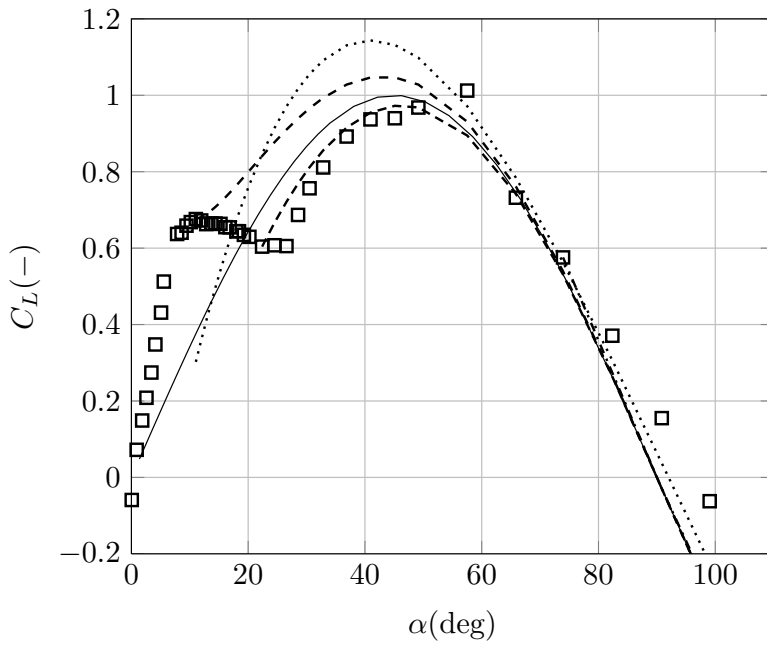


Figure 85: NACA 0018 comparison of lift coefficient vs AoA for experiments and post-stall model at $Re = 290e3$ with $AR = 50$ for tripped condition: \square exp., — Flat Plate, - - VC up, - · - VC low, · · - VC f.p., ··· AERODAS

RESULTS

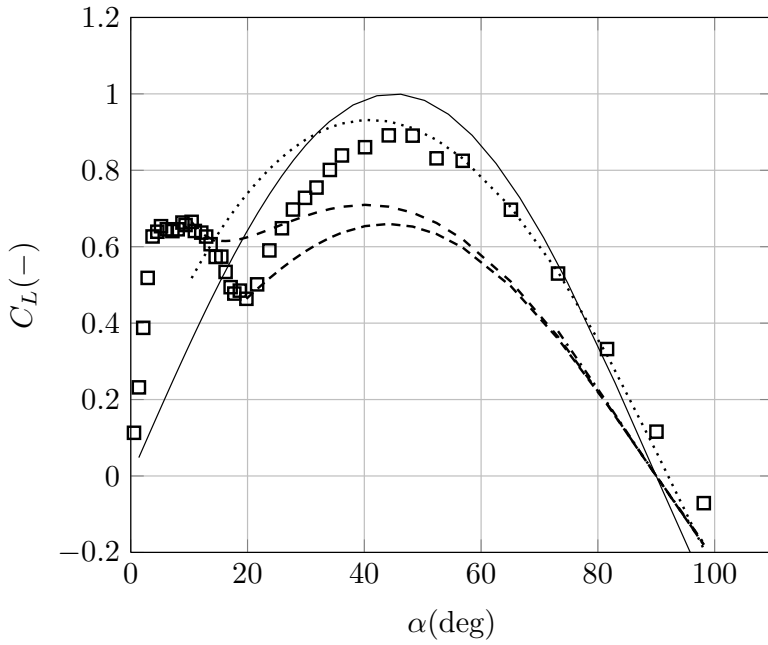


Figure 86: NACA 0018 comparison of lift coefficient vs AoA for experiments and post-stall model at $Re = 115e3$ with $AR = 10$ for tripped condition: \square exp., — Flat Plate, - - VC up, - · - VC low, · · · VC f.p., · · · AERODAS

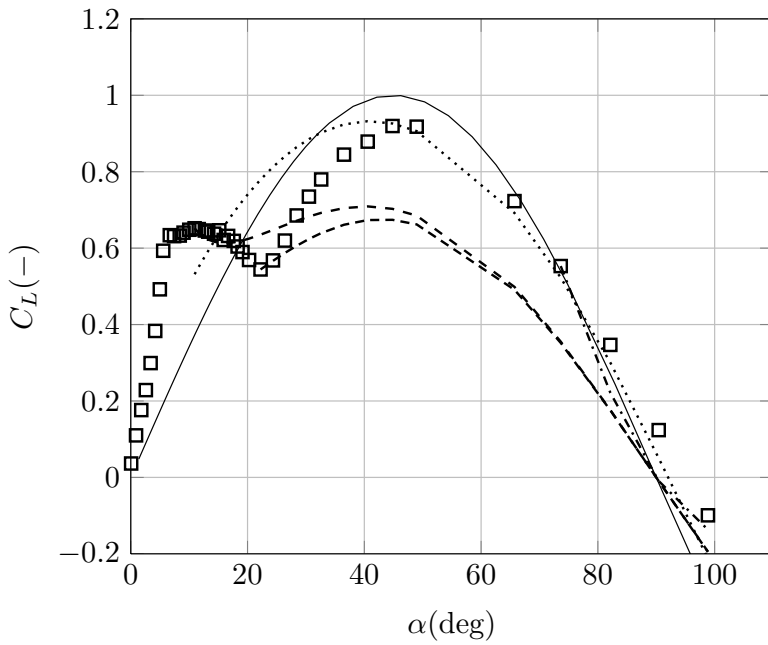


Figure 87: NACA 0018 comparison of lift coefficient vs AoA for experiments and post-stall model at $Re = 230e3$ with $AR = 10$ for tripped condition: \square exp., — Flat Plate, - - VC up, - · - VC low, · · · VC f.p., · · · AERODAS

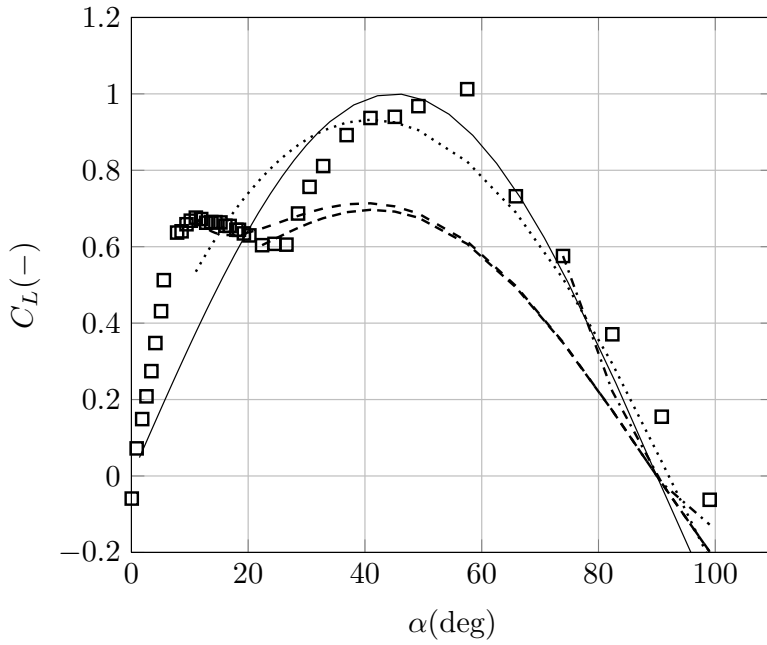


Figure 88: NACA 0018 comparison of lift coefficient vs AoA for experiments and post-stall model at $Re = 290e3$ with $AR = 10$ for tripped condition: \square exp., — Flat Plate, - - VC up, - · - VC low, - · · - VC f.p., · · · AERODAS

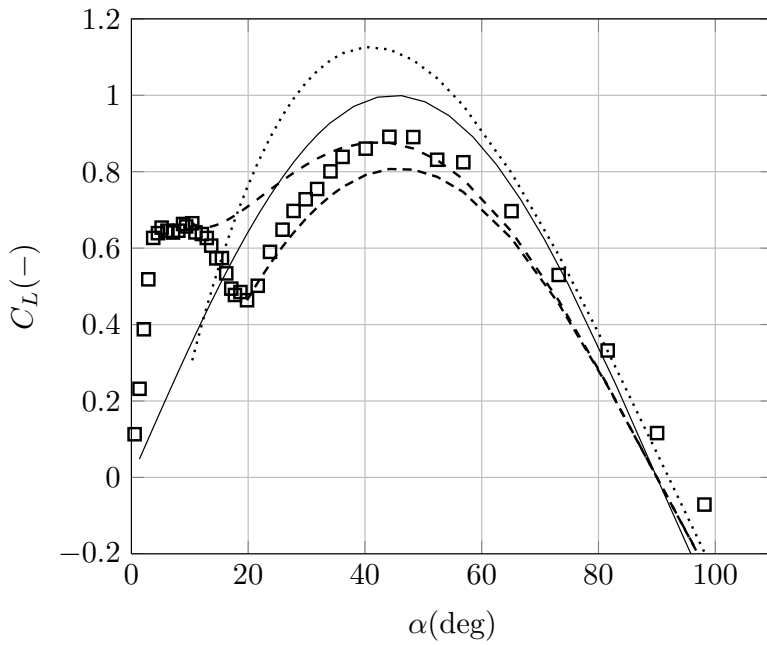


Figure 89: NACA 0018 comparison of lift coefficient vs AoA for experiments and post-stall model at $Re = 115e3$ with $AR = 30$ for tripped condition: \square exp., — Flat Plate, - - VC up, - · - VC low, - · · - VC f.p., · · · AERODAS

RESULTS

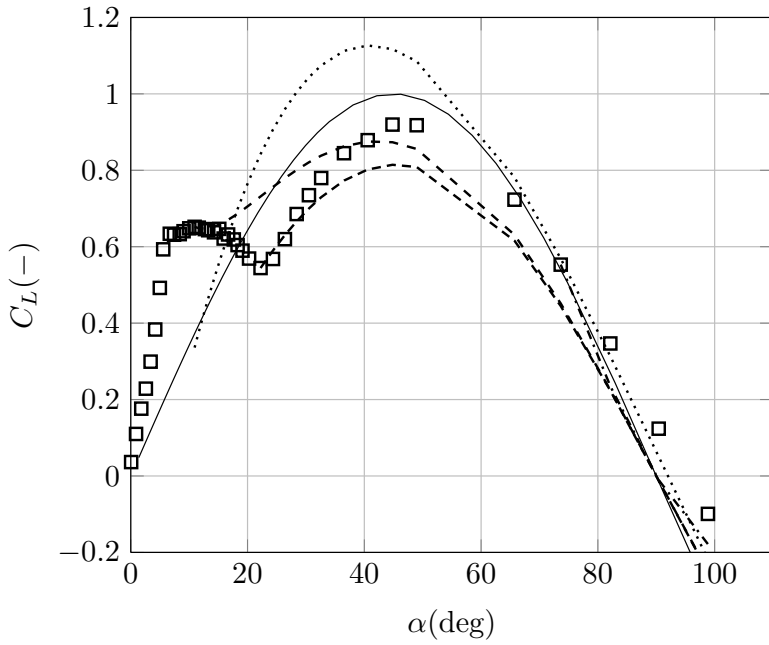


Figure 90: NACA 0018 comparison of lift coefficient vs AoA for experiments and post-stall model at $Re = 230e3$ with $AR = 30$ for tripped condition: \square exp., — Flat Plate, - - VC up, - · - VC low, · · - VC f.p., · · · AERODAS

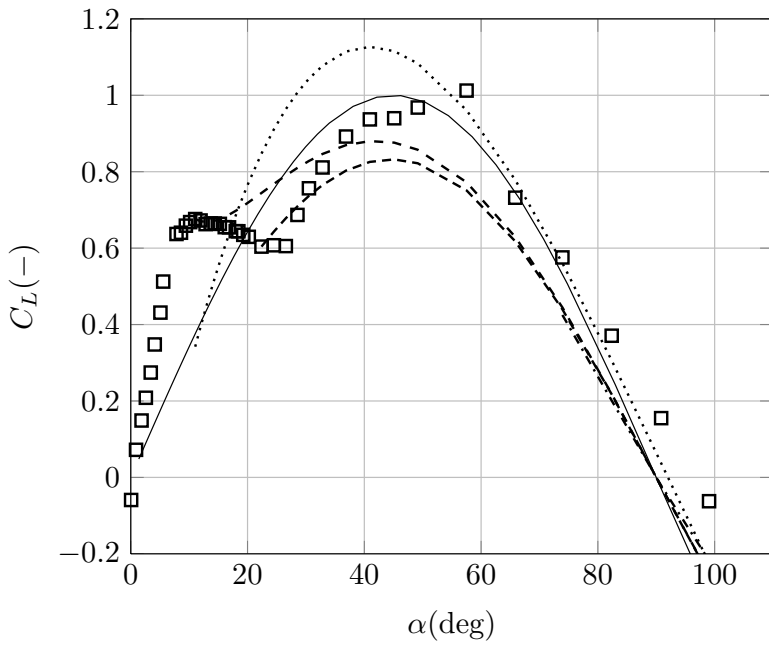


Figure 91: NACA 0018 comparison of lift coefficient vs AoA for experiments and post-stall model at $Re = 290e3$ with $AR = 30$ for tripped condition: \square exp., — Flat Plate, - - VC up, - · - VC low, · · - VC f.p., · · · AERODAS

In Figure 92-93-94, 95-96-97 and 98-99-100 the post-stall semi-empirical models are applied to drag coefficient distribution with an aspect ratio, respectively, equal to 50, 10 and 30.

The post-stall modelling for the drag coefficient exhibits a far different behavior. As for the lift coefficient vs AoA, in this case considering an aspect ratio different from that of 2D assumptions (i. e. 50), the match between experiments and modelling gives a good estimation of the high angle of attack region up to 90 degrees. Again here for drag coefficient, the better proposal among the three of page 65 remains the second, mostly because of the laminar bucket.

The third assumption of 65 undergoes to an ill posed extrapolation for almost all the Reynolds numbers because of the attachment point, that for the aerodynamic efficiency to be equal to that of the theoretical flat plate lies about 70 degrees, to have a drag coefficient higher than the maximum allowable from Viterna-Corrigan model equation 2.29, i. e. 2.

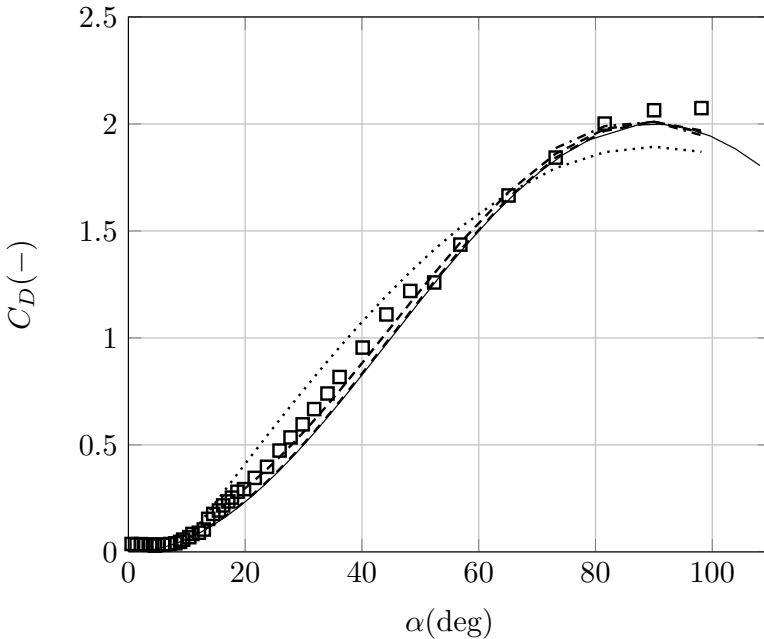


Figure 92: NACA 0018 comparison of drag coefficient vs AoA for experiments and post-stall model at $Re = 115e3$ with $AR = 50$ for tripped condition: \square exp., — Flat Plate, - - VC up, - · - VC low, · · · VC f.p., · · · AERODAS

RESULTS

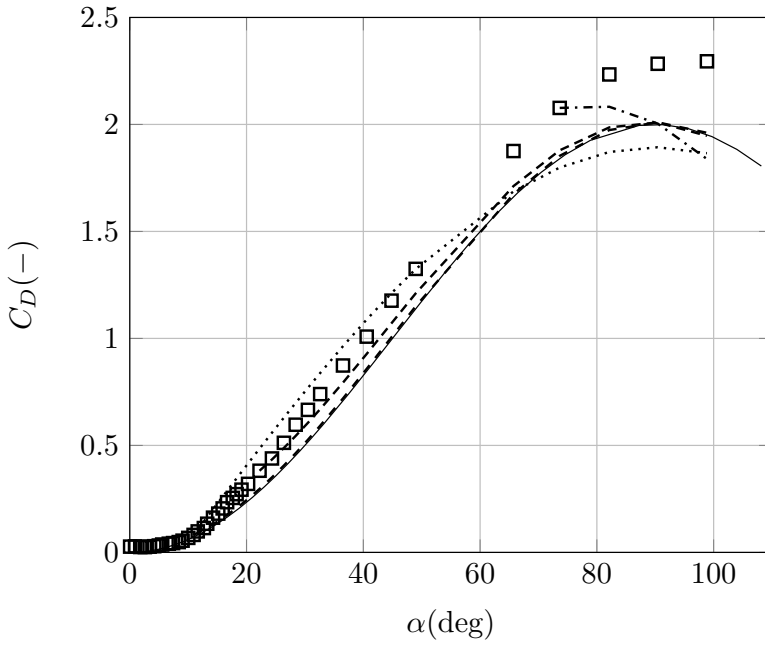


Figure 93: NACA 0018 comparison of drag coefficient vs AoA for experiments and post-stall model at $Re = 230e3$ with $AR = 50$ for tripped condition: \square exp., — Flat Plate, - - VC up, - · - VC low, · · · VC f.p., · · · AERODAS

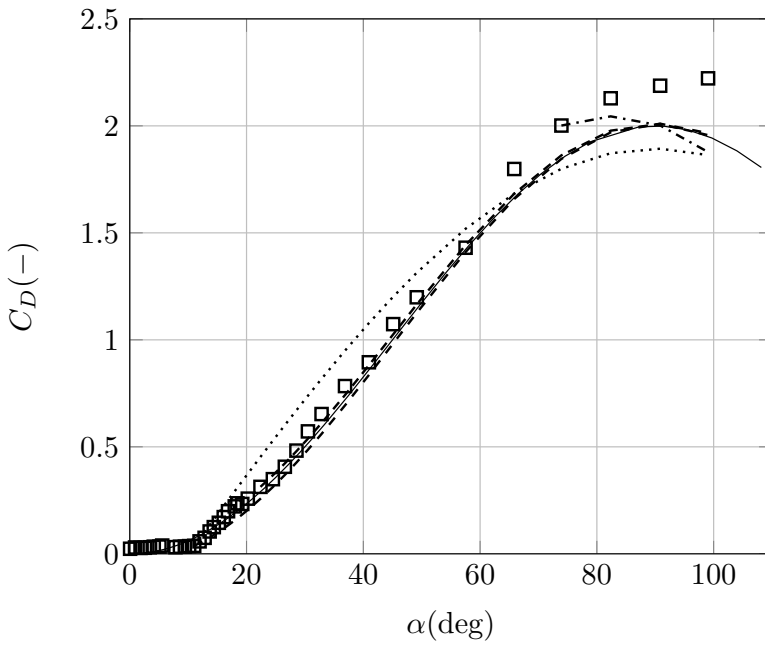


Figure 94: NACA 0018 comparison of drag coefficient vs AoA for experiments and post-stall model at $Re = 290e3$ with $AR = 50$ for tripped condition: \square exp., — Flat Plate, - - VC up, - · - VC low, · · · VC f.p., · · · AERODAS

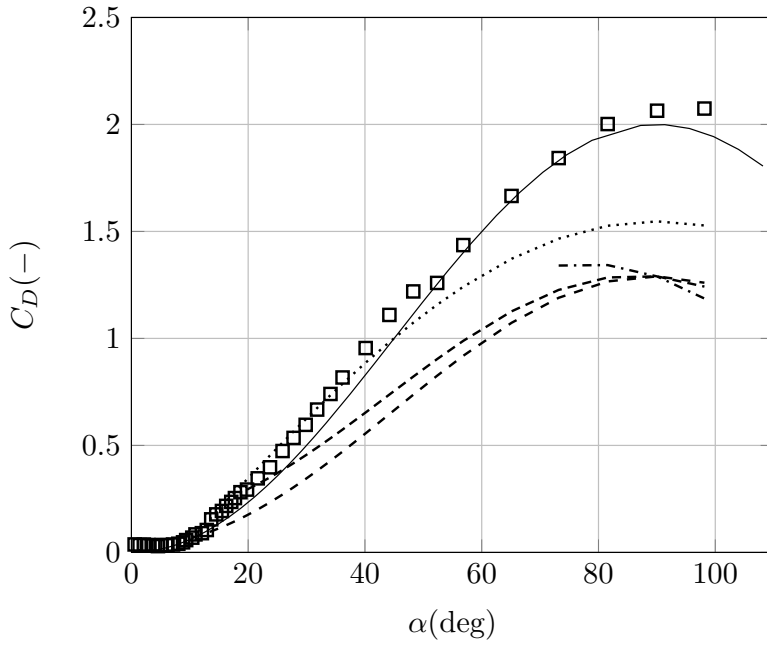


Figure 95: NACA 0018 comparison of drag coefficient vs AoA for experiments and post-stall model at $Re = 115e3$ with $AR = 10$ for tripped condition: \square exp., — Flat Plate, - - VC up, - · - VC low, · · · VC f.p., ··· AERODAS

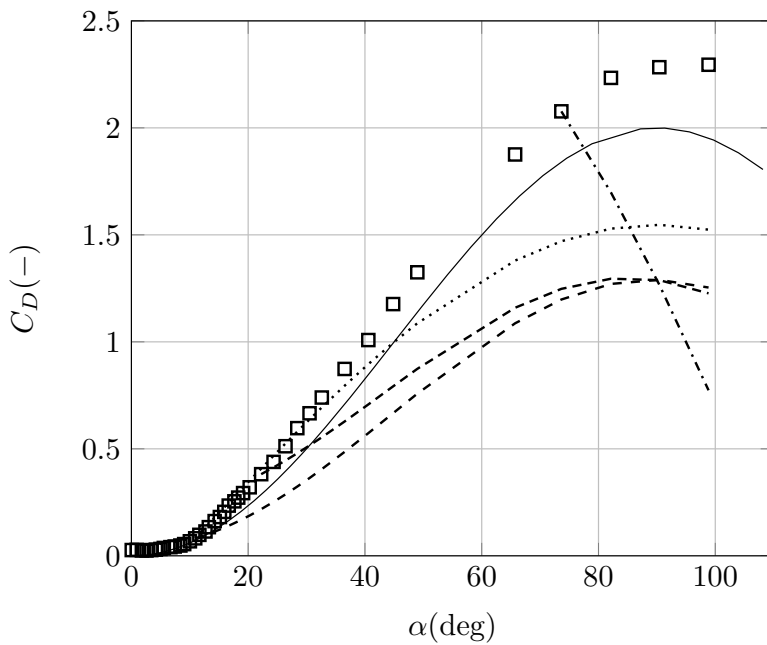


Figure 96: NACA 0018 comparison of drag coefficient vs AoA for experiments and post-stall model at $Re = 230e3$ with $AR = 10$ for tripped condition: \square exp., — Flat Plate, - - VC up, - · - VC low, · · · VC f.p., ··· AERODAS

RESULTS

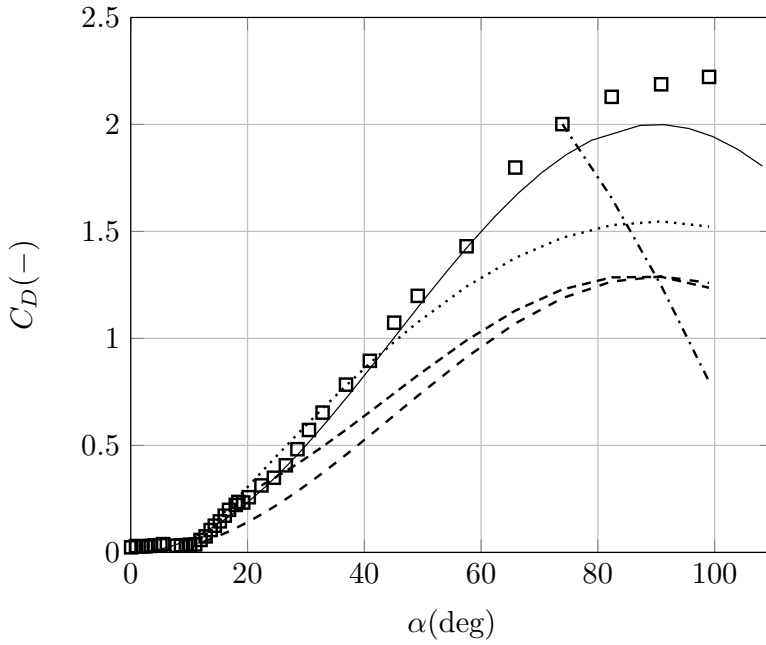


Figure 97: NACA 0018 comparison of drag coefficient vs AoA for experiments and post-stall model at $Re = 290e3$ with $AR = 10$ for tripped condition: \square exp., — Flat Plate, - - VC up, - · - VC low, - · · - VC f.p., ··· AERODAS

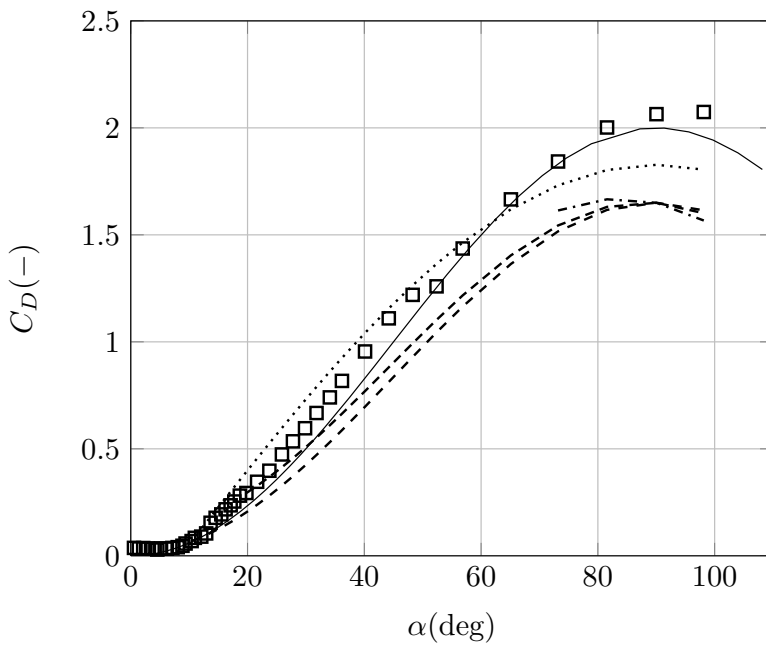


Figure 98: NACA 0018 comparison of drag coefficient vs AoA for experiments and post-stall model at $Re = 115e3$ with $AR = 30$ for tripped condition: \square exp., — Flat Plate, - - VC up, - · - VC low, - · · - VC f.p., ··· AERODAS

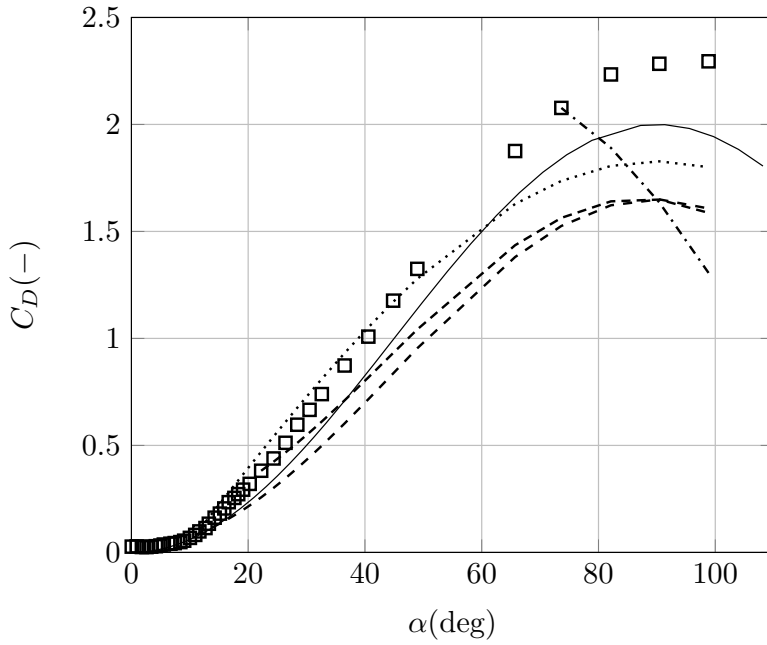


Figure 99: NACA 0018 comparison of drag coefficient vs AoA for experiments and post-stall model at $Re = 230e3$ with $AR = 30$ for tripped condition: \square exp., — Flat Plate, - - VC up, - · - VC low, - · · - VC f.p., ··· AERODAS

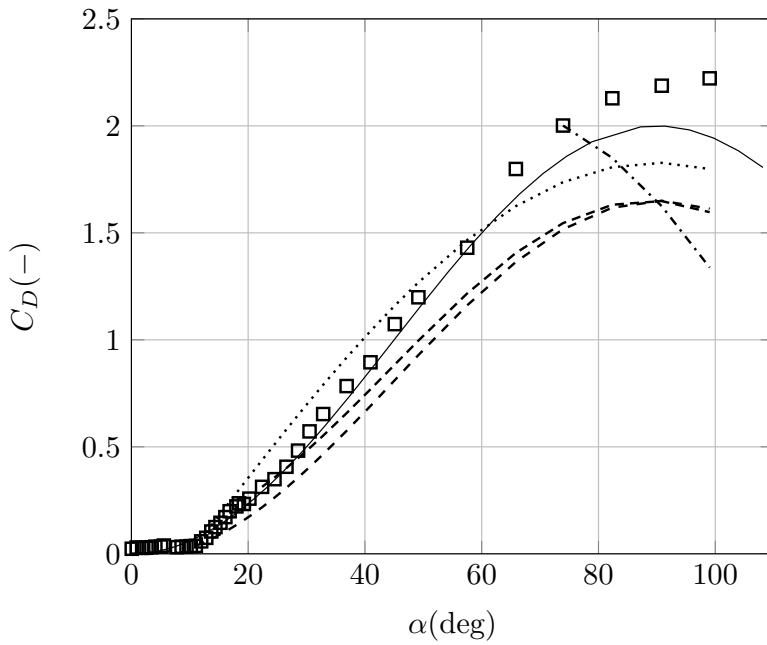


Figure 100: NACA 0018 comparison of drag coefficient vs AoA for experiments and post-stall model at $Re = 290e3$ with $AR = 30$ for tripped condition: \square exp., — Flat Plate, - - VC up, - · - VC low, - · · - VC f.p., ··· AERODAS

3.2.4 Comparison with Delft experiments

In this subsection a comparison of both experimental and numerical results obtained within this research and the experiments of Timmer [75] from TU Delft are performed. The TU Delft data refer to a wind tunnel which turbulence intensity is a bit lower than that present in our wind tunnel, and moreover, the Reynolds number investigated by Timmer where spread over a larger range (up to $700e3$) so that here only the first two values are considered, namely $150e3$ and $300e3$.

Experiments against Delft

In Figure 101-102, respectively, the lift and drag coefficient vs AoA obtained from experimental measurements are compared with those of Timmer from TU Delft. For the lift coefficient pressure measurements are considered, while for drag coefficient, because of no pressure wake rake installed, force measurements are considered.

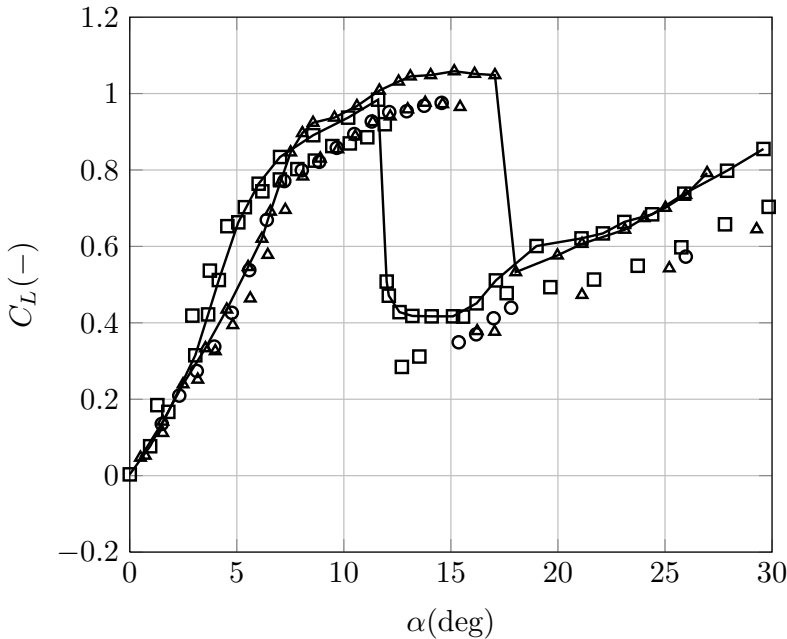


Figure 101: NACA 0018 comparison with Delft experiments for lift coefficient: pressure meas. \square Re = $115e3$, \circ Re = $230e3$, \triangle Re = $290e3$
 \square Timmer (pressure) Re = $150e3$, \triangle Timmer (pressure) Re = $300e3$

Concerning the lift coefficient vs AoA some differences arise. In linear range, i.e. angle of attack lower than 8 degrees, the lower Reynolds number investigated, i.e. $115e3$, exhibits a slightly higher lift coefficient with respect to the $150e3$ Reynolds number of Timmer, as if the lower the Reynolds number the higher the effect on lift coefficient of the laminar bubble presence; the other two Reynolds numbers, i.e. $230e3$, $290e3$ are in good agreement with the higher value of Timmer (i.e. $300e3$). In the stall region is observed a general trend in under-estimate the maximum lift coefficient, circumstance that could be related to the influence that the turbulence intensity has on the stall lift peak, while the stall onset angle

of attack seems to be for each Reynolds number investigated coherently located with would should be expected. A difference of about 0.1 in lift coefficient is observed in post-stall region, with no dependence on Reynolds number as confirmed by Timmer's results too.

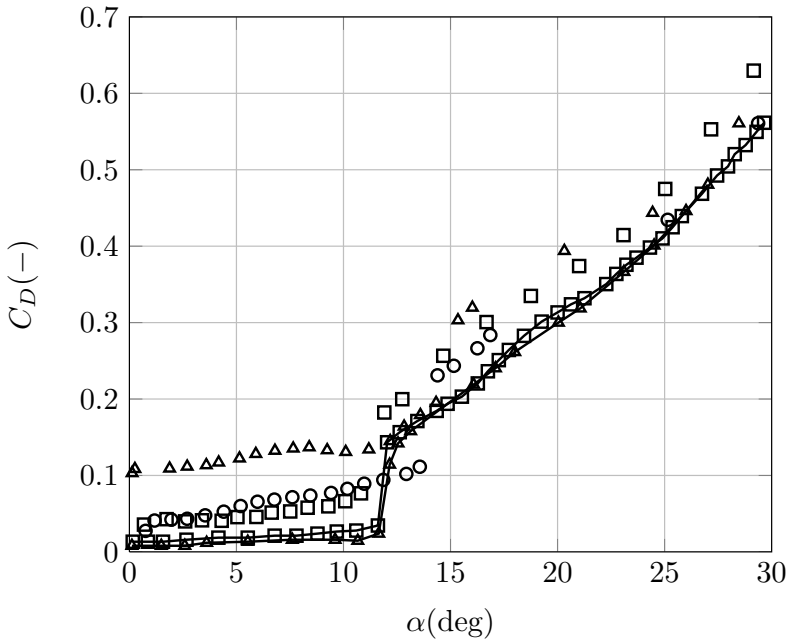


Figure 102: NACA 0018 comparison with Delft experiments for drag coefficient: force meas. \square Re = 115e3, \circ Re = 230e3, \triangle Re = 290e3
 \square Timmer (wake rake) Re = 150e3, \triangle Timmer (wake rake) Re = 300e3

Concerning, instead, the drag coefficient vs AoA clearly no direct comparison could be made for the low angle of attack region because of force measurements availability only. However, these same force measurements are more confident for post-stall region. The main difference here lies in the laminar bucket extension: our measurements via fore balance reproduce a laminar bucket extension depending on Reynolds number, precisely with its width growing with an increase in Reynolds number, while Delft measurements via pressure wake rake observe a width constant with a 100% increase in Reynolds number. Differences no bigger than 0.05 are present in post-stall region.

Numerics against Delft

In Figure 103-104, respectively, the lift and drag coefficient vs AoA obtained from numerical simulations are compared with those of Timmer from TU Delft.

Concerning the lift coefficient vs AoA some differences arise. In linear range, i. e. angle of attack lower than 8 degrees, the lower Reynolds number investigated, i. e. 115e3, exhibits a slightly lower lift coefficient with respect to the 150e3 Reynolds number of Timmer, as if the strength of laminar bubble present on the airfoil is not as high as that experienced into experiments; the other two Reynolds numbers, i. e. 230e3, 290e3 are in good agreement with the higher value of Timmer (i. e. 300e3). In the stall region is observed a general trend in under-estimate

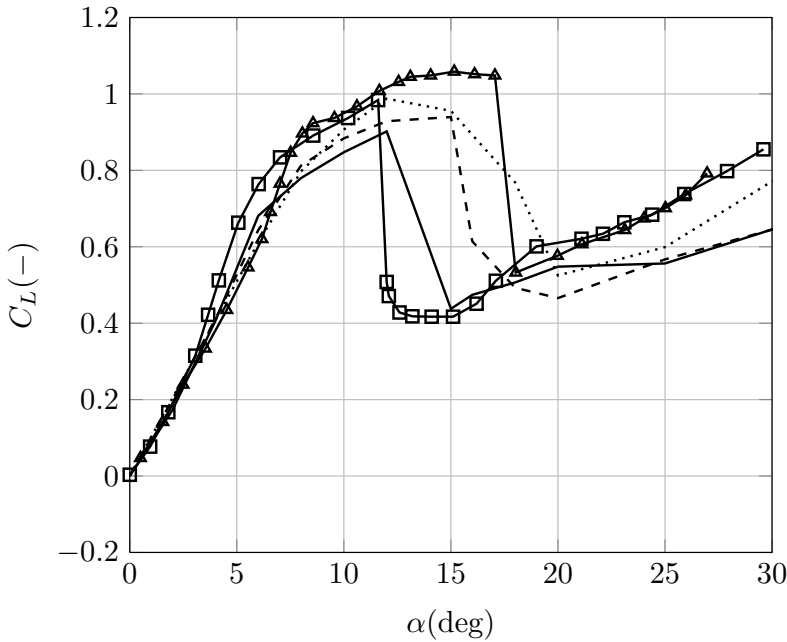


Figure 103: NACA 0018 simulations compared to Delft experiments for lift coefficient:
 num. — $Re = 115e3$, -- $Re = 230e3$, ... $Re = 290e3$
 \square Timmer (pressure) $Re = 150e3$, \triangle Timmer (pressure) $Re = 300e3$

the maximum lift coefficient, while the stall onset angle of attack seems to be for each Reynolds number investigated coherently located with would should be expected, nonetheless an abrupt reduction in lift coefficient is not experienced and it involves between 3 and 4 degrees to attain the post-stall recovery value. A difference of about 0.1 in lift coefficient (under-estimation) is observed in post-stall region, with no big dependence on Reynolds number as confirmed by Timmer's results too.

Concerning, instead, the drag coefficient vs AoA clearly in this case also a direct comparison could be made for the low angle of attack region, that seems to be in total agreement with the Delft measurements. The main difference here lies in the laminar bucket extension as for our experiments too: our simulations reproduce a laminar bucket extension depending on Reynolds number, precisely with its width growing with an increase in Reynolds number, while Delft measurements via pressure wake rake observe a width constant with a 100% increase in Reynolds number. Differences no bigger than 0.05 are present in post-stall region.

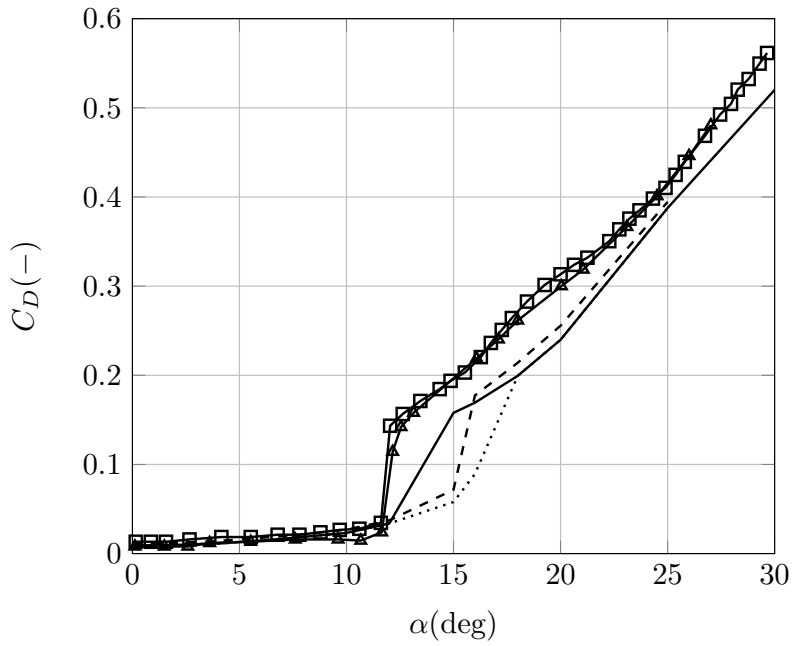


Figure 104: NACA 0018 simulations compared to Delft experiments for drag coefficient:
 num. — Re = 115e3, -- Re = 230e3, ... Re = 290e3
 □ Timmer (wake rake) Re = 150e3, △ Timmer (wake rake) Re = 300e3

3.2.5 Effect of wind tunnel wall on blockage

In this section the effect of wind tunnel wall on blockage are investigated by means of the repetition of the mid-span section pressure measurements similar to those discussed in subsection 3.2.1 on page 40 with a different wind tunnel facility, at out disposal in the Department of Aerospace Engineering, with an open test section (see Figure 105).

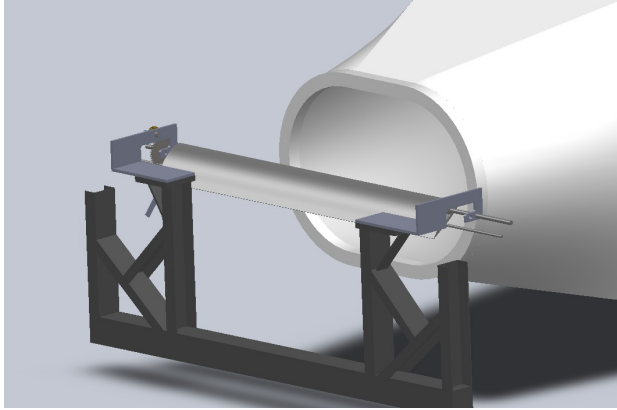


Figure 105: Open test section wind tunnel facility detail

Recently some authors [84] have observed a far different behavior in their experiments when comparing measurements derived from closed and open test section wind tunnel facility. In their tests a big difference has been observed in lift coefficient vs AoA around the secondary peak after post-stall recovery and maximum drag coefficient at about 90 degrees. In Figure 106 and Figure 107 a comparison between measurements of, respectively, lift and drag coefficient performed in open and closed test section wind tunnel for a NACA 0015 airfoil at $Re = 209e3$ is shown, as presented in [52, 84]. These results exhibit a fairly different behavior with respect to other literature results for more than a reason: firstly, the linear range seems to be characterized by a lower lift-curve slope than the one typically prescribed for 2D measurements; secondly, they show a maximum lift coefficient at stall definitely lower than that found in other literature data [60] even if this circumstance could be easily addressed to the lower Reynolds number investigated. Worasinchai [84] explained this by assuming the truthfulness of the hypothesis stated by Rainbird [52] concerning the affection that closed test section measurements for blockage ratio lower than 15 could lead to lift and drag coefficient estimation: in this case the blockage ratio is assumed to be defined as H/c , where H is the test section height, or in general the dimension perpendicular to the tested wing model.

In Figure 106 is evident the big difference in linear range for both experimental set-up with respect to the simple numerical solution given by the panel method based external aerodynamic code XFOIL [17]. Such a dissimilar behavior could be addressed to an intrinsic 3D effect derived from the experimental test arrangement (they have removed the top and bottom test section panel within some other little modifications to locate the model), or an effect of tripped condition or extremely turbulent flow. In order to better understand this circumstance an

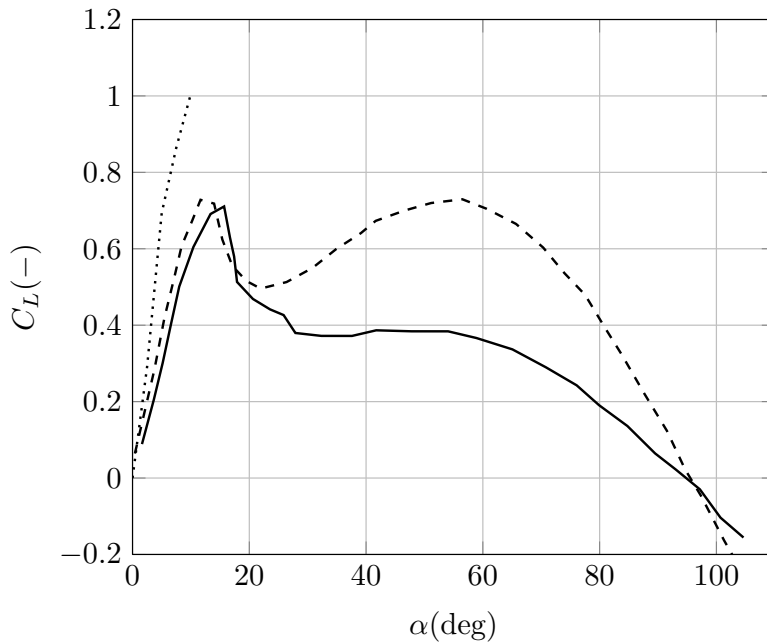


Figure 106: NACA 0015 airfoil at $Re = 209e3$ lift coefficient vs AoA from Rainbird experiments [52, 84]: — open test section, - - closed test section, \cdots XFOIL [17]

analogous investigation has been carried out in the open test section wind tunnel of the Department of Aerospace Engineering for both NACA 0018 and GT10 airfoils, for clean and tripped conditions.

In Figure 108-109 the lift coefficient vs AoA for the NACA 0018 airfoil at $Re = 230e3$ for both clean and tripped condition is shown. Figure 108 clearly reports that for the open test section test there is a consistent reduction in secondary peak for lift coefficient in both clean and tripped condition. As seen also in Worasinchai and Rainbird results, even the measurements from our tests exhibit a great difference in the linear range, where the angle of attack are low and the lift-curve slope is lower than expected from 2D measurements or simulations. In order to exploit this point in Figure 109 a detailed portion of the pre-stall and stall region is magnified: the grey circle enclosed the region where the differences are more evident, and with increasing angle of attack also the distinct behavior for stall onset. This aspect could be related to both 3D effects or particularly high turbulence intensity: XFOIL code predict in case of higher turbulence intensity or tripped on both upper and lower side airfoil condition a reduction of the lift slope in linear range that seems to be compatible with what observed in the experiments. The same situation has been observed also for different Reynolds, here not reported, and for a cambered different airfoil, namely the GT10. However, because of the consistent difference already underlined here, another wind tunnel test campaign in our closed test section wind tunnel facility providing an arrangement for halve open test section in order to, restraining to similar turbulent intensity condition, have better insight into this question.

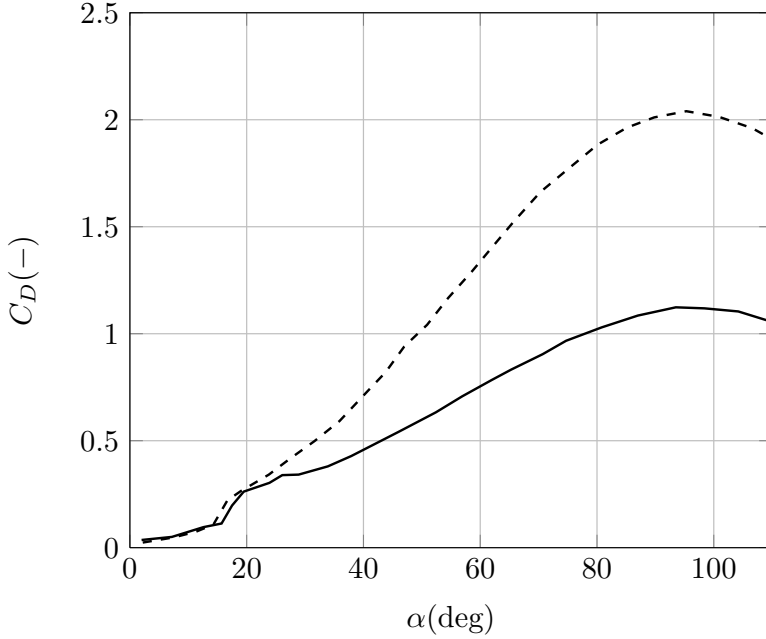


Figure 107: NACA 0015 airfoil at $Re = 209e3$ drag coefficient vs AoA from Rainbird experiments [52, 84]: — open test section, - - closed test section

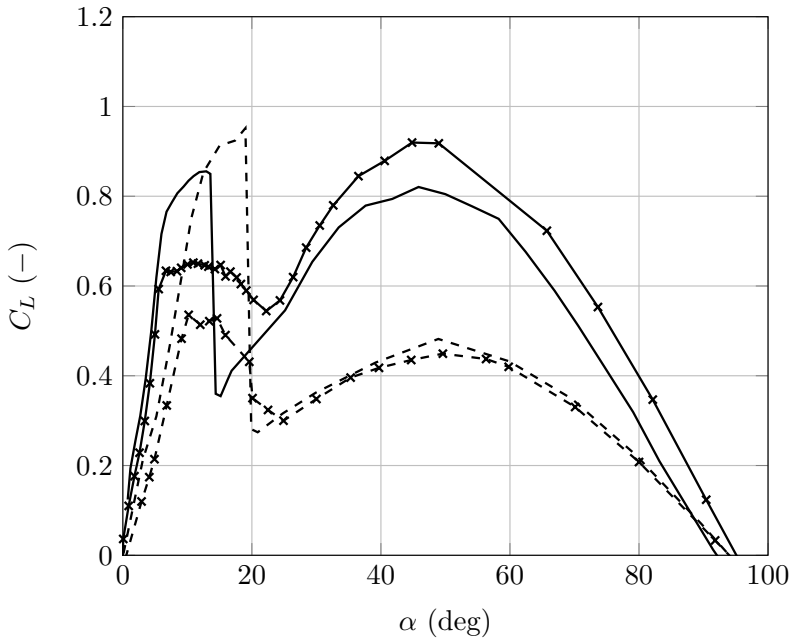


Figure 108: Blockage effects on NACA 0018 lift coefficient vs AoA for $Re = 230e3$: — closed test section clean, ✕- closed test section tripped, - - open test section clean, -✕- open test section tripped

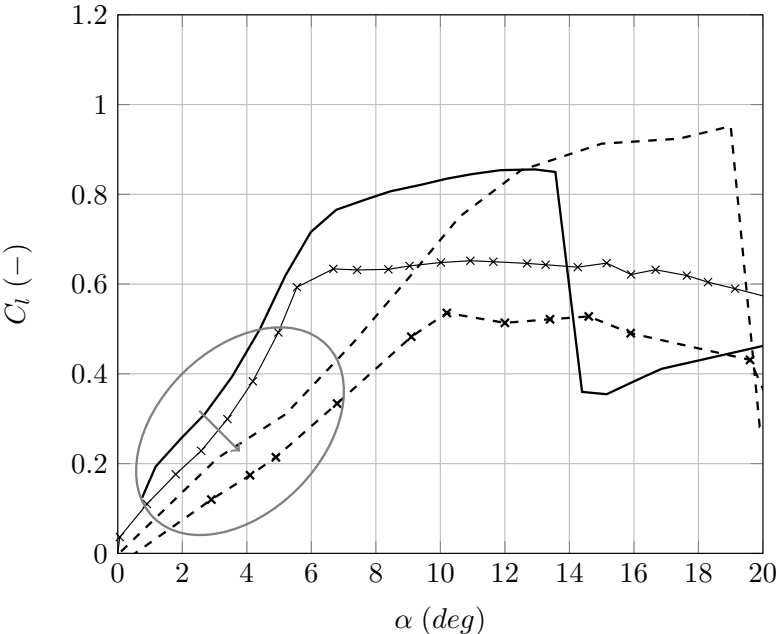


Figure 109: NACA 0018 lift coefficient vs AoA detail in pre-stall and stall region for $Re = 230e3$: — closed test section clean, \times - closed test section tripped, - - open test section clean, - \times - open test section tripped

3.3 GT10

The cambered airfoil GT10 developed at the Department of Industrial Engineering of University of Naples Federico II has been numerically investigated in clean condition for a range of Reynolds numbers analogous to those employed for NACA 0018 airfoil in section 3.2. No experimental results are available, thus no indication of location for zigzag tape is available and so no tripped condition have been replicated neither via numerical simulation.

3.3.1 Numerical simulations

In Figure 110 the lift coefficient vs AoA is shown. Only very little difference is exhibited in terms of maximum lift coefficient attainable, an almost negligible effects of Reynolds number could be observed in post-stall region.

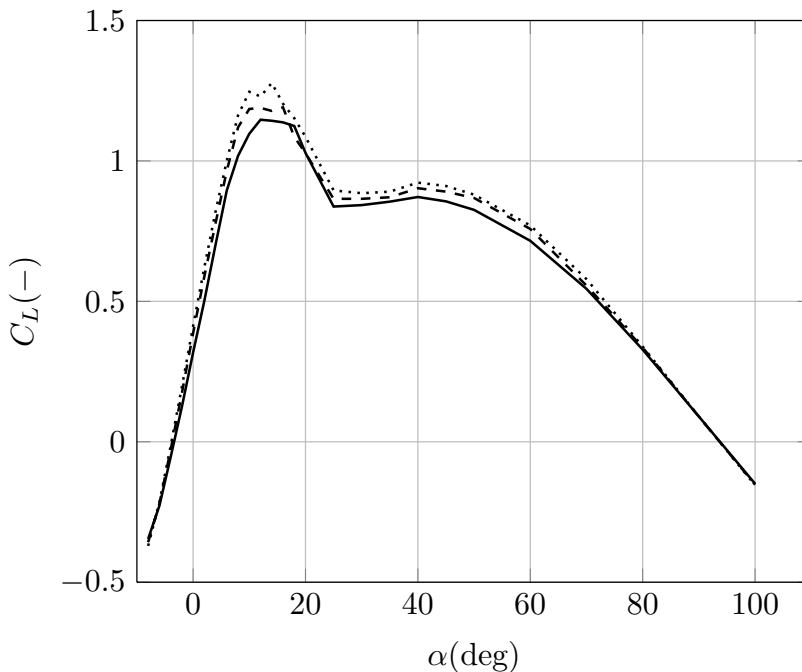


Figure 110: GT10 numerical lift coefficient vs AoA for clean case: — $Re = 115e3$, - - $Re = 230e3$, \cdots $Re = 290e3$

In Figure 111 the drag coefficient vs AoA is shown. Only very little difference is exhibited in terms of maximum drag coefficient attainable, an almost negligible effects of Reynolds number could be observed in post-stall region.

In Figure 112 the aerodynamic efficiency vs AoA is shown. The great difference is exhibited in the low angle of attack region, an almost negligible effects of Reynolds number could be observed in post-stall region. In order to exploit the difference with theoretical flat plate behavior, in Figure 113 a detailed portion is provided in order to emphasize the point where the attachment of the post-stall Viterna-Corrigan model should be placed under Tangler [73] assumptions.

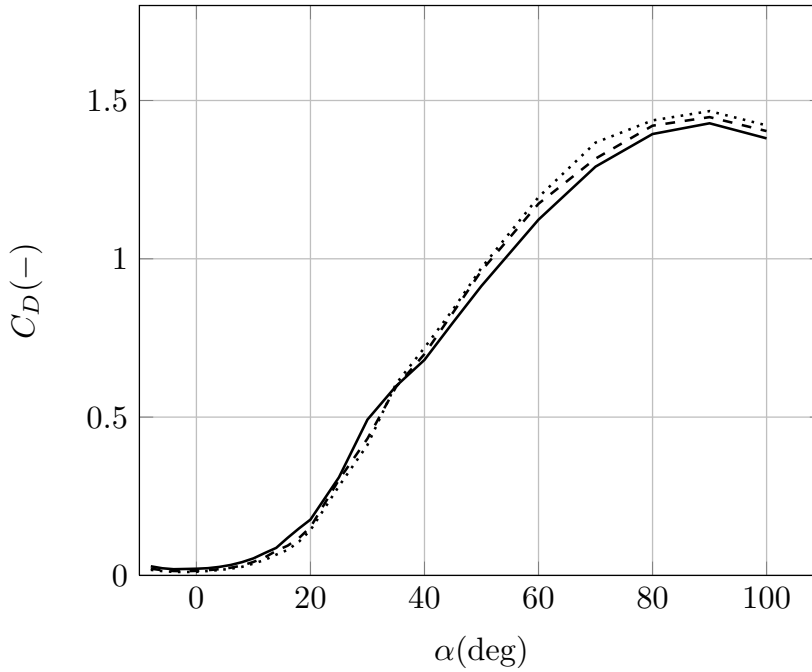


Figure 111: GT10 numerical drag coefficient vs AoA for clean case: — Re = 115e3, - - Re = 230e3, ··· Re = 290e3

GT10 synoptic table

In this paragraph a synoptic table for the GT10 airfoil is presented in order to summarize the main aerodynamic characteristics for clean condition derived from numerical analysis.

Parameter	Re = 115e3	Re = 230e3	Re = 290e3
α_{0L} (deg)	-3.4	-3.7	-3.9
$C_{L,\alpha}$ (deg ⁻¹)	0.0897	0.1010	0.1052
E_{max} (-)	27.2532	39.8831	47.9415
$\alpha_{E_{max}}$ (deg)	6	6	4
$C_{L,max}$ (-)	1.1467	1.1910	1.2776
$\alpha_{C_{L,max}}$ (deg)	12	16	14

Table 11: GT10 synoptic table for aerodynamic characteristics

RESULTS

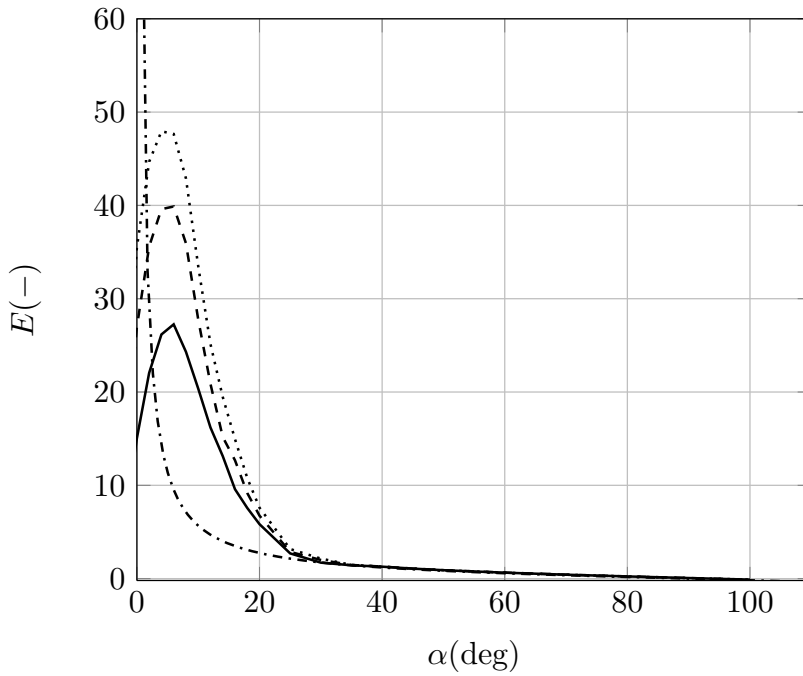


Figure 112: GT10 numerical aerodynamic efficiency coefficient vs AoA for clean case: — $\text{Re} = 115\text{e}3$, -- $\text{Re} = 230\text{e}3$, \cdots $\text{Re} = 290\text{e}3$, - · - flat plate

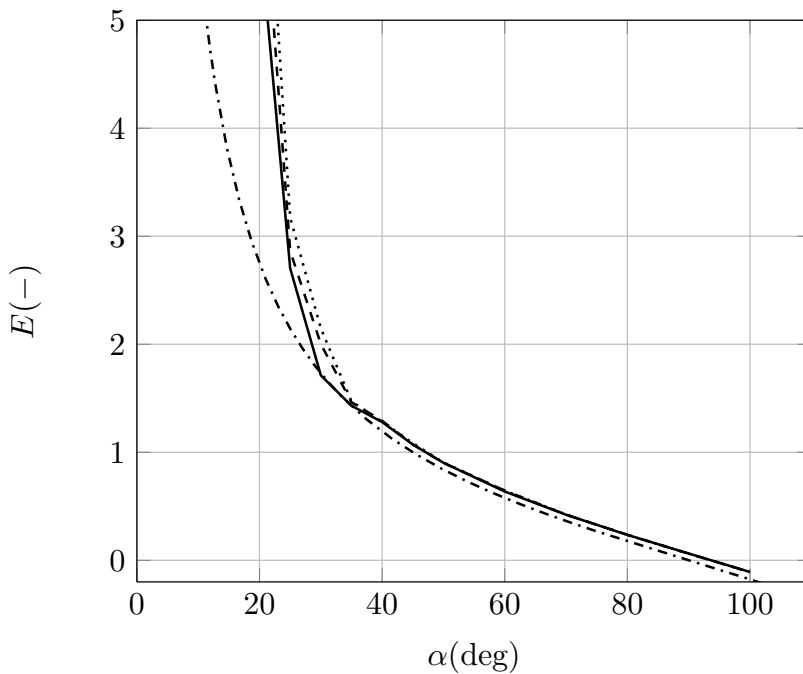


Figure 113: GT10 numerical aerodynamic efficiency coefficient vs AoA for clean case, a detail: — $\text{Re} = 115\text{e}3$, -- $\text{Re} = 230\text{e}3$, \cdots $\text{Re} = 290\text{e}3$, - · - flat plate

3.3.2 Post-stall modelling

In this subsection are presented the results of a comparison between the numerical simulations and the post-stall models already described in section 2.2 taking advantage of what already shown in subsection 3.2.3, i. e. limiting our discussion only to a single Reynolds number, namely the higher one $290e3$, because of the only little difference among the three in terms of both lift and drag coefficient behavior with respect to the angle of attack. Having many models to compare with the numerics, in the following figures the results derived from CFD simulations are indicated with a square (like this \square), typically used for experiments data.

In Figure 114-115 the lift coefficient against AoA is shown for the higher Reynold number for both aspect ratio values equal to 50 and 10. The case considering an intermediate aspect ratio value equal to 30, comprised between the bi-dimensional case and the geometrical value, is exploited for all the three Reynolds number in Figure 116-117-118 showing again the better agreement of the Viterna-Corrigan model attached to the post-stall beginning point with respect to all the other.

In Figure 119-120 the drag coefficient against AoA is shown for the higher Reynold number for both aspect ratio values equal to 50 and 10. The case considering an intermediate aspect ratio value equal to 30, comprised between the bi-dimensional case and the geometrical value, is exploited for all the three Reynolds number in Figure 121-122-123 showing again the better agreement of the Viterna-Corrigan model attached to the post-stall beginning point with respect to all the other. For the drag coefficient, as already seen for the NACA 0018 airfoil the suggested aspect ratio for post-stall extrapolation remains the bi-dimensional value, namely $AR = 50$.

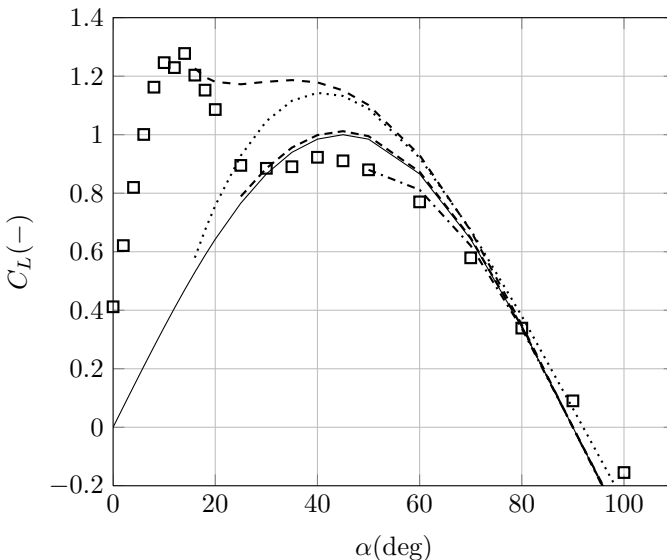


Figure 114: GT10 comparison of lift coefficient vs AoA for experiments and post-stall model at $Re = 290e3$ with $AR = 50$ for clean condition: \square exp., — Flat Plate, --- VC up, -.- VC low, ··· VC f.p., ···· AERODAS

RESULTS

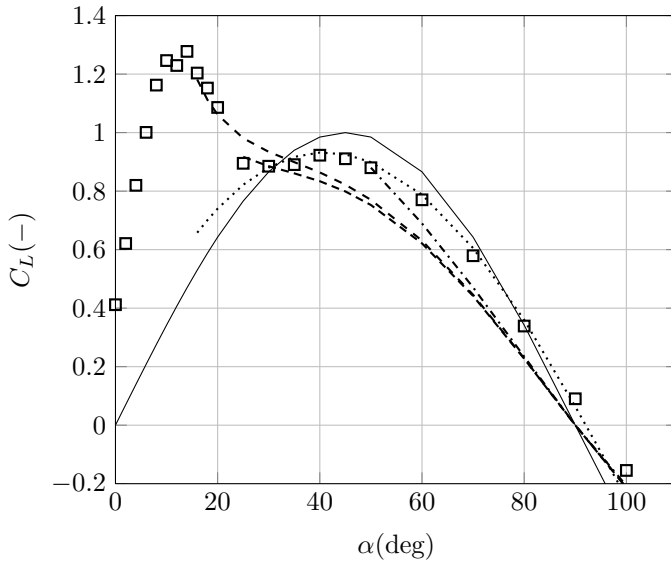


Figure 115: GT10 comparison of lift coefficient vs AoA for experiments and post-stall model at $Re = 290e3$ with $AR = 10$ for clean condition: \square exp., — Flat Plate, - - VC up, - · - VC low, - · · - VC f.p., ··· AERODAS

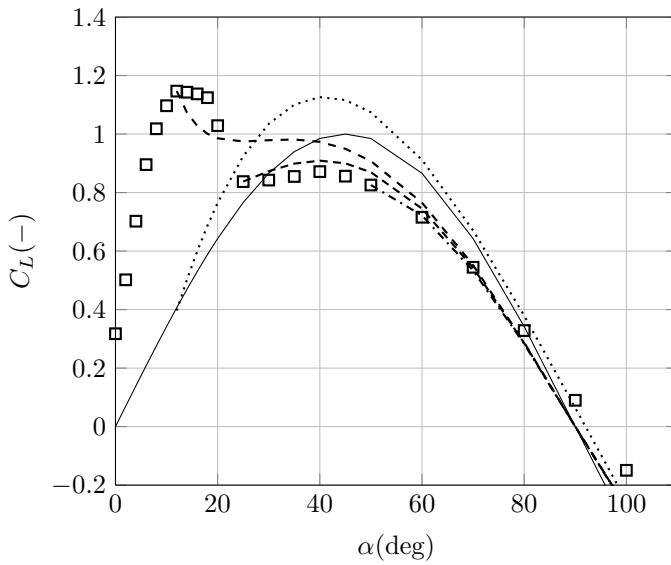


Figure 116: GT10 comparison of lift coefficient vs AoA for experiments and post-stall model at $Re = 115e3$ with $AR = 30$ for clean condition: \square exp., — Flat Plate, - - VC up, - · - VC low, - · · - VC f.p., ··· AERODAS

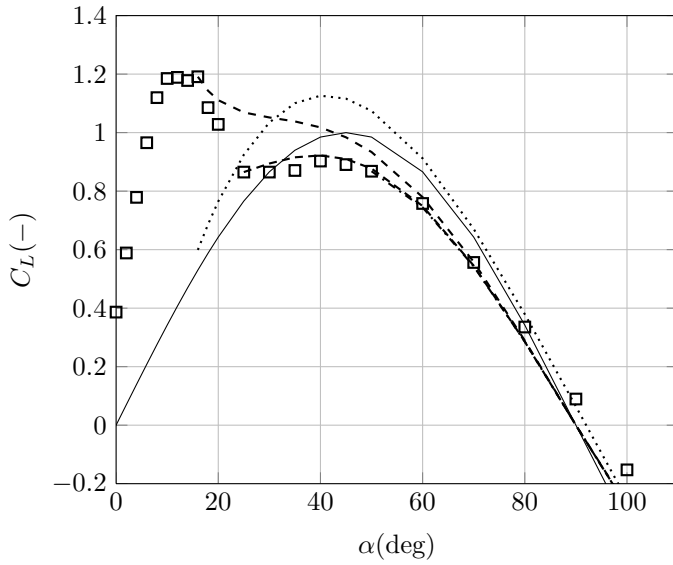


Figure 117: GT10 comparison of lift coefficient vs AoA for experiments and post-stall model at $Re = 230e3$ with $AR = 30$ for clean condition: \square exp., — Flat Plate, - - VC up, -·- VC low, ··· VC f.p., ··· AERODAS

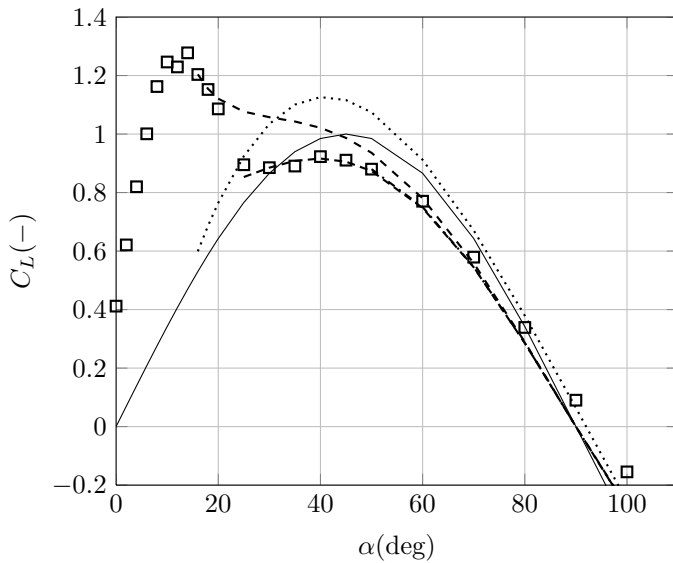


Figure 118: GT10 comparison of lift coefficient vs AoA for experiments and post-stall model at $Re = 290e3$ with $AR = 30$ for clean condition: \square exp., — Flat Plate, - - VC up, -·- VC low, ··· VC f.p., ··· AERODAS

RESULTS

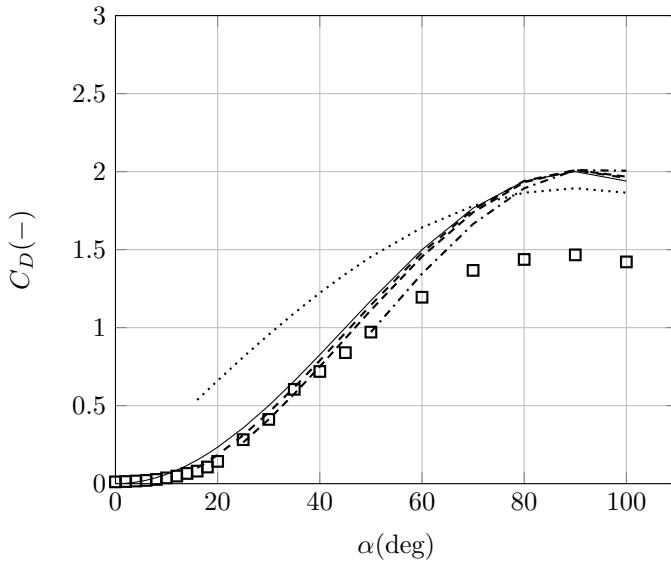


Figure 119: GT10 comparison of drag coefficient vs AoA for experiments and post-stall model at $Re = 290e3$ with $AR = 50$ for clean condition: \square exp., — Flat Plate, - - VC up, - · - VC low, - · - VC f.p., ··· AERODAS

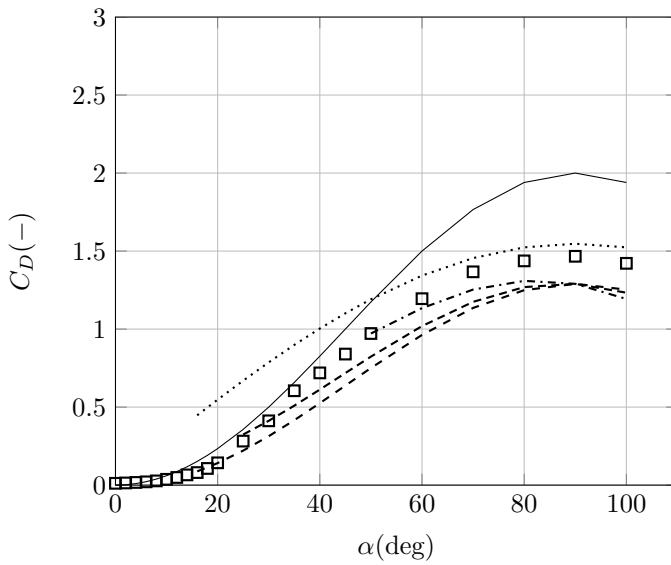


Figure 120: GT10 comparison of drag coefficient vs AoA for experiments and post-stall model at $Re = 290e3$ with $AR = 10$ for clean condition: \square exp., — Flat Plate, - - VC up, - · - VC low, - · - VC f.p., ··· AERODAS

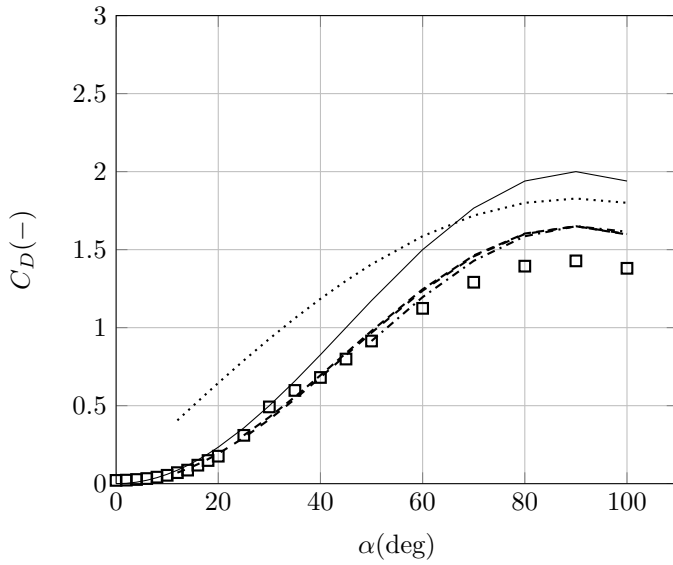


Figure 121: GT10 comparison of drag coefficient vs AoA for experiments and post-stall model at $Re = 115e3$ with $AR = 30$ for clean condition: \square exp., — Flat Plate, - - VC up, -·- VC low, ··· VC f.p., ··· AERODAS

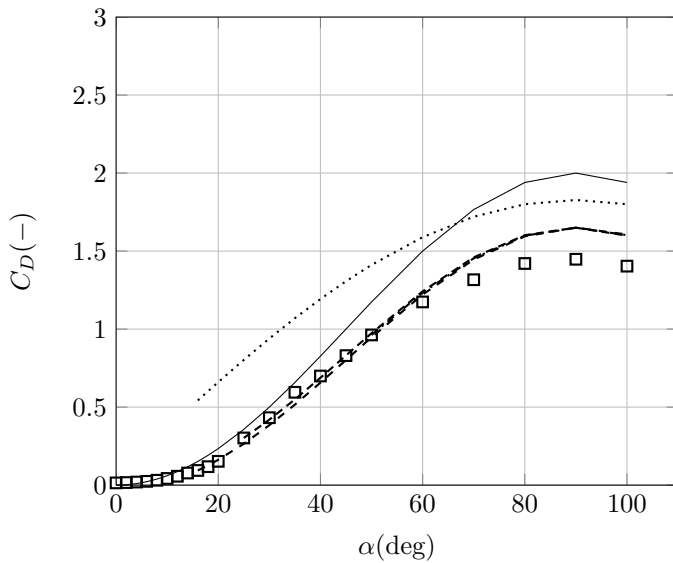


Figure 122: GT10 comparison of drag coefficient vs AoA for experiments and post-stall model at $Re = 230e3$ with $AR = 30$ for clean condition: \square exp., — Flat Plate, - - VC up, -·- VC low, ··· VC f.p., ··· AERODAS

RESULTS

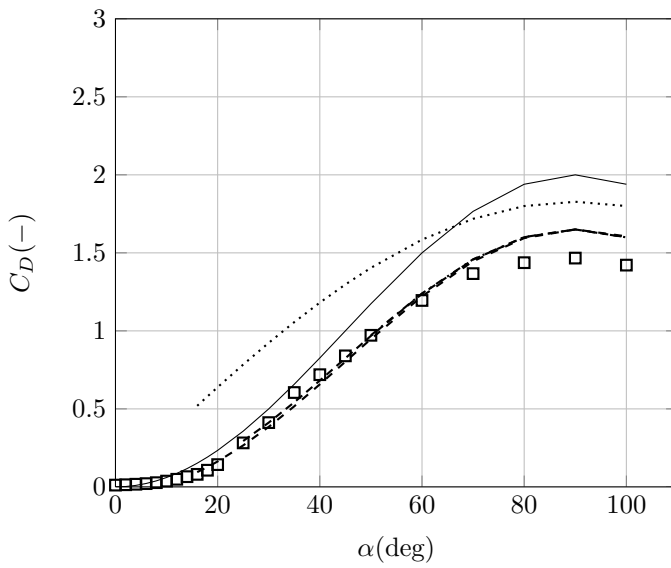


Figure 123: GT10 comparison of drag coefficient vs AoA for experiments and post-stall model at $Re = 290e3$ with $AR = 30$ for clean condition: \square exp., — Flat Plate, --- VC up, -·- VC low, ··· VC f.p., ··· AERODAS

4

CONCLUSIONS

In this work an both experimental and numerical investigation on post-stall characteristics of airfoil for wind turbine blade operating at low Reynolds number has been conducted. The NACA 0018 airfoil has been tested in the closed circuit closed test section wind tunnel facility of the Department of Industrial Engineering of University of Naples Federico II. The range of Reynolds number is about $[1e5, 3e5]$, while the angle of attack is comprised between 0 and 110 degrees. Both free and forced transition condition have been analyzed by means of zigzag adaption on airfoil leading edge. Aerodynamic coefficient have been computed with data coming from both force and pressure measurements deriving from force balance and one instrumented section at the midspan of the tested model.

Has been observed a low reliability of the more recent post-stall model named AERODAS (developed by Spera [66]): many comparisons with both experimental and numerical simulations shown a very poor agreement concerning, in particular, the lift coefficient distribution in post-stall where the magnitude of the computed lift secondary peak lies quite above what has been observed with CFD analysis and measured in the wind tunnel.

The Viterna-Corrigan model has generally shown a better agreement with experiments with respect to the AERODAS model. However, it has been observed that a different choice of the attachment point (in the plane α , C_L) and aspect ratio AR could lead to big differences especially for the lift coefficient distribution. In particular an intermediate value for the AR, between the ideal testing condition (i.e. a 2D case, that corresponds to $AR = 50$ together with Viterna assumptions) and the geometrical value, depending on the real tested model span and chord size (in this case $AR = 10$), lead to a very good agreement between analytical extrapolation and the results coming from both experiments and numerical simulations. This could be addressed to the intrinsic 3D flow condition present at large angle of attack (i.e. around 45 deg) where mushroom shaped stall cells are located on all the wing span, so that a strong dependence on AR is present. However, the drag coefficient distribution still gives good results in comparison with experiments for aspect ratio value corresponding to 2D case (i.e. $AR = 50$). This could lead to a separated relationship for C_L and C_D with respect to the aspect ratio AR in order to assess a slightly modified formulation that would better describe the results from experiments. More experiments on a cambered airfoil, namely the GT10 18% thickness airfoil developed by Department of Aerospace Engineering of University of Naples Federico II, are needed to constitute a more robust basis for such hypothesis.

The CFD simulations performed on NACA 0018 airfoil has shown a fairly good agreement with respect to the experiments. The stall behavior is well captured in terms of maximum lift coefficient, while the abrupt decrease of the same coefficient after the stall is, for all the Reynolds numbers considered, is not good described because of a delay on stall onset seen by numerical simulations together with a more gradually decrease of the C_L . Analogously, the drag coeffi-

cient show a similar laminar bucket region, in comparison with TU Delft data because of no pressure rake wake measurements taken in our experiments, with a delay of stall onset induced drag coefficient increase for all the Reynolds numbers analyzed. The post-stall behavior is instead fairly good captured by the numerical simulations for all the Reynolds numbers considered: this is a very promising alternative to Viterna extrapolation when still some uncertainties remain concerning the exact point of attachment of the analytical method to the data from experiments and, moreover, 3D effects on lift coefficient distribution, due to not 2D nor geometrical aspect ratio value as stated before, could lead to unacceptable differences with respect to experiments, and in our case also to 2D numerical simulations. This would favourably improve the design of passive stall controlled HAWT, although the computational and numerical solution assessment time required by CFD method would sound not so good as the simple, almost no time, application of Viterna method. The requirement for a very fine tuned aerodynamic useful in critical off-design operation would be the threshold in deciding which one should be preferred.

NACA 0018 airfoil has undergone a numerical analysis considering the introduction of a step shaped zigzag tape within the computational grid. For all the Reynolds numbers investigated the difference in stall behavior is generally well captured with respect to the experiments: the step geometry introduced clearly reduce the maximum lift coefficient attainable resulting also in a delayed stall onset with a more smooth decrease of the same coefficient before the post-stall portion that leads to the secondary peak. Because of no pressure rake wake measurements taken in our experiments, nothing could be stated about the drag coefficient at low angle of attack regime, and only a pure numerical simulations with and without the step-shaped zigzag tape could be presented. As indicated by the experiments in clean and tripped condition, no big differences in lift coefficient distribution in post-stall region is present between the numerical simulations with and without the zigzag tape, and again they are both in fairly good agreement with the experiments. This evidence would favourably affect the prediction of a wind turbine whose blades are far from maintenance period for which dirty leading edge region lead to lower performance, and so a better evaluation of energy extraction capability and further the payback time for this machine.

A | $k_T - k_L - \omega$ MODEL FORMULATION

The transport equations are:

$$\frac{Dk_T}{Dt} = P_{k_T} + R_{BP} + R_{NAT} - \omega k_t - D_T + \frac{\partial}{\partial x_j} \left[\left(\nu + \frac{\alpha_T}{\sigma_k} \right) \frac{\partial k_T}{\partial x_j} \right] \quad (A.1)$$

$$\frac{Dk_L}{Dt} = P_{k_L} + R_{BP} + R_{NAT} - D_L + \frac{\partial}{\partial x_j} \left[\nu \frac{\partial k_L}{\partial x_j} \right] \quad (A.2)$$

$$\begin{aligned} \frac{D\omega}{Dt} = & C_{\omega 1} \frac{\omega}{k_T} P_{k_T} + \left(\frac{C_{\omega R}}{f_W} - 1 \right) \frac{\omega}{k_T} (R_{BP} + R_{NAT}) \\ & - C_{\omega 2} \omega^2 + C_{\omega 3} f_{\omega} \alpha_T f_W^2 \frac{\sqrt{k_T}}{d^3} + \frac{\partial}{\partial x_j} \left[\left(\nu + \frac{\alpha_T}{\sigma_{\omega}} \right) \frac{\partial \omega}{\partial x_j} \right]. \end{aligned} \quad (A.3)$$

In the ω equation, the fully turbulent production, destruction, and gradient transport terms (first, third, and fifth terms on the right-hand side of Eq. A.3) are analogous to the similar terms in the k_T and k_L equations and are similar to terms that appear in other $k - \omega$ model forms. The transition production term (second term on right-hand side) is intended to produce a reduction in turbulence length scale during the transition breakdown process. The production of turbulent and laminar kinetic energy by mean strain is modelled as:

$$P_{k_T} = \nu_{T,s} S^2 \quad (A.4)$$

$$P_{k_L} = \nu_{T,l} S^2. \quad (A.5)$$

The “small-scale” eddy-viscosity is defined as

$$\nu_{T,s} = f_{\nu} f_{INT} C_{\mu} \sqrt{k_{T,s}} \lambda_{eff} \quad (A.6)$$

where $k_{T,s}$ is the effective small-scale turbulence

$$k_{T,s} = f_{SS} f_W k_T. \quad (A.7)$$

The kinematic wall effect is included through an effective (wall limited) turbulence length scale λ_{eff} and damping function f_W

$$\lambda_{eff} = \min(C_\lambda d, \lambda_T) \quad (A.8)$$

$$\lambda_T = \frac{\sqrt{k_T}}{\omega} \quad (A.9)$$

$$f_W = \left(\frac{\lambda_{eff}}{\lambda_T} \right). \quad (A.10)$$

The viscous wall effect is incorporated through the viscous damping function, which is computed in terms of the effective turbulence Reynolds number

$$f_v = 1 - \exp\left(-\frac{\sqrt{Re_T}}{A_v}\right) \quad (A.11)$$

$$Re_T = \frac{f_W^2 k_T}{\nu \omega}. \quad (A.12)$$

The shear-sheltering effect discussed in the previous subsection is included in the damping function

$$f_{SS} = \exp\left[-\left(\frac{C_{SS} \nu \Omega}{k_T}\right)^2\right]. \quad (A.13)$$

The turbulent viscosity coefficient C_μ is defined to satisfy the realizability constraint following Shih et al. [61]

$$C_\mu = \frac{1}{A_0 + A_s \left(\frac{S}{\omega}\right)}. \quad (A.14)$$

The effect of intermittency on the turbulence production is included through an empirical intermittency damping function

$$f_{INT} = \min\left(\frac{k_L}{C_{INT} k_{TOT}}, 1\right). \quad (A.15)$$

The production of laminar kinetic energy k_L is assumed to be governed by the large-scale near-wall turbulent fluctuations [81], based on the correlation of pretransitional fluctuation growth with freestream low-frequency wall-normal turbulent fluctuations [80, 33]. The large-scale turbulence contribution is

$$k_{T,L} = k_T - k_{T,s}, \quad (A.16)$$

where the small-scale contribution is defined by Eq. A.7. The production term is

$$P_{k_L} = \nu_{T,L} S^2, \quad (A.17)$$

where

$$v_{T,l} = \min \left\{ f_{\tau,l} C_{11} \left(\frac{\Omega \lambda_{eff}^2}{\nu} \right) \sqrt{t_{T,l} \lambda_{eff}} + \beta_{TS} C_{12} \text{Re}_\Omega d^2 \Omega, \frac{0.5 \cdot (k_L + k_{T,l})}{S} \right\} \quad (\text{A.18})$$

The limit is applied to ensure satisfaction of the realizability constraint for the total Reynolds stress contribution. The production term is comprised of two parts - the first addresses the development of Klebanoff modes and the second addresses self-excited (i.e., natural) modes, with

$$\text{Re}_\Omega = \frac{d^2 \Omega}{\nu} \quad (\text{A.19})$$

$$\beta_{TS} = 1 - \exp \left(- \frac{\max \text{Re}_\Omega - C_{TS,crit}, 0}{A_{TS}} \right) \quad (\text{A.20})$$

$$f_{\tau,l} = 1 - \exp \left[- C_{\tau,l} \frac{k_{T,l}}{\lambda_{eff}^2 \Omega^2} \right]. \quad (\text{A.21})$$

The anisotropic (near-wall) dissipation terms for k_T and k_L take a common form

$$D_T = \nu \frac{\partial \sqrt{k_T}}{\partial x_j} \frac{\partial \sqrt{k_T}}{\partial x_j} \quad (\text{A.22})$$

$$D_L = \nu \frac{\partial \sqrt{k_L}}{\partial x_j} \frac{\partial \sqrt{k_L}}{\partial x_j}. \quad (\text{A.23})$$

The turbulent transport terms in the k_T and ω equations include an effective diffusivity α_T defined as

$$\alpha_T = f_\nu C_{\mu,std} \sqrt{k_{T,s}} \lambda_{eff}. \quad (\text{A.24})$$

The boundary layer production term (intended to reproduce proper behavior of the boundary layer wake region) includes a kinematic damping function of the form

$$f_\omega = 1 - \exp \left[- 0.41 \cdot \left(\frac{\lambda_{eff}}{\lambda_T} \right)^4 \right]. \quad (\text{A.25})$$

The remaining terms in the transport equations are related to the laminar-to-turbulent transition mechanism in the model. As mentioned above, transition occurs as a transfer of energy from k_L to k_T , with a concurrent reduction in

$A_0 = 4.04$	$C_{INT} = 0.75$	$C_{\omega 1} = 0.44$
$A_s = 2.12$	$C_{TS,crit} = 1000$	$C_{\omega 2} = 0.92$
$A_v = 6.75$	$C_{R,NAT} = 0.02$	$C_{\omega 3} = 0.3$
$A_{BP} = 0.6$	$C_{l1} = 3.4 \cdot 10^{-6}$	$C_{\omega R} = 1.5$
$A_{NAT} = 200$	$C_{l2} = 1.0 \cdot 10^{-10}$	$C_\lambda = 2.495$
$A_{TS} = 200$	$C_R = 0.12$	$C_{\mu,std} = 0.09$
$C_{BP,crit} = 1.2$	$C_{\alpha,\theta} = 0.035$	$Pr_\theta = 0.85$
$C_{NC} = 0.1$	$C_{SS} = 1.5$	$\sigma_k = 1$
$C_{NAT,crit} = 1250$	$C_{\tau,l} = 4360$	$\sigma_\omega = 1.17$

Table 12: Constants value for $k_T - k_L - \omega$ model.

turbulence length scale from the freestream value to the value found in an equilibrium turbulent boundary layer. The model terms R_{BP} and R_{NAT} appear with opposite signs in the k_T and k_L equations and represent bypass and natural transition, respectively. The model forms are

$$\beta_{BP} = 1 - \exp\left(-\frac{\phi_{BP}}{A_{BP}}\right) \quad (A.26)$$

$$\phi_{BP} = \max\left[\left(\frac{k_T}{\nu\Omega} - C_{BP,crit}\right), 0\right] \quad (A.27)$$

$$\beta_{NAT} = 1 - \exp\left(-\frac{\phi_{NAT}}{A_{NAT}}\right) \quad (A.28)$$

$$\phi_{NAT} = \max\left[\left(\text{Re}_\Omega - \frac{C_{NAT,crit}}{f_{NAT,crit}}\right), 0\right] \quad (A.29)$$

$$f_{NAT} = 1 - \exp\left(-C_{NC} \frac{\sqrt{k_L} d}{\nu}\right). \quad (A.30)$$

Note that the function $f_{NAT,crit}$ is included so that the amplitude of the pre-transitional fluctuations influences the initiation of natural transition in an appropriate manner. The turbulent viscosity used in the momentum equations is the sum of the small-scale and large-scale contributions defined above.

$$\nu_T = \nu_{T,s} + \nu_{T,l}, \quad (A.31)$$

In Table 12 there is a summary of all model's constants values.

BIBLIOGRAPHY

- [1] Abbott, I.H., von Doenhoff, A.E.: *Theory of Wing Sections: Including a Summary of Airfoil Data*. Dover Publications, ISBN 978-0486605869 (1959).
- [2] Aholt, J., Finaish, F.: Active Flow Control Strategy of Laminar Separation Bubbles Developed over Subsonic Airfoils at Low Reynolds Numbers. In: 49th AIAA Aerospace Sciences Meeting including the New Horizons Forum and Aerospace Exposition, 4-7 January 2011, Orlando, Florida, AIAA 2011-733 (2011).
- [3] Aupoix, B., Spalart, P.R.: Extensions of the Spalart-Allmaras turbulence model to account for wall roughness. In: *International Journal of Heat and Fluid Flow*, Vol. 24, pp. 454-62 (2003).
- [4] Barlow, J.B., Rae, W.H., Pope, A.: *Low-Speed Wind Tunnel Testing*. John Wiley & Sons. ISBN-13: 978-0471557746 (1999).
- [5] Bechly, M.E., Clausen, P.D., Ebert, P.R., Pemberton, A., Wood, D.H.: Development and testing of a 5 kW Wind Turbine. In: *Proc. ANZ Solar Energy Soc Conf. Solar '95* (1995).
- [6] Blackwell, T.J.: Subsonic Wind-Tunnel Wall Corrections on a Wing with Clark Y-14 Airfoil. A Masters Project Presented to The Faculty of the Department of Mechanical and Aerospace Engineering San Jose State University (2011).
- [7] Burton, T., Sharpe, D., Jenkins, N., Bossanyi, E.: *Wind Energy Handbook*. John Wiley & Sons, Ltd Eds, ISBN 9780470846063 (2002).
- [8] Claessens, M.C.: *The Design and Testing of Airfoils for Application in Small Vertical Axis Wind Turbines*. Master of Science Thesis, TU Delft, November 2006.
- [9] D'Amato, E., Daniele, E., Mallozzi, L., Petrone, G.: Waiting time costs in a bilevel location-allocation problem. In: *Contributions to game theory and management*, Vol. V, pagg 178-186 (2012), Graduate School of Management, St. Petersburg University, Eds. L. A. Petrosyan and N. A. Zenkevich, ISBN 9785992400755.
- [10] D'Amato, E., Daniele, E., Mallozzi, L., Petrone, G., Tancredi, S.: A Hierarchical Multi-modal Hybrid Stackelberg-Nash GA for a Leader with Multiple Followers Game. In: *Dynamics of Information Systems: Mathematical Foundations*, Springer Proceedings in Mathematics & Statistics, Ed. Sorokin, A.; Murphey, R.; Thai, M.T.; Pardalos, P.M., Vol. 20, pp. 267-280 (2012), Springer Verlag USA, ISBN 9781461439059.
- [11] D'Amato, E., Daniele, E., Mallozzi, L., Petrone, G.: Equilibrium strategies via GA to Stackelberg games under multiple follower's best reply. In: *International Journal of Intelligent Systems*, Vol. 27, no. 2, pp. 74-85 (2012), Wiley Periodicals, Inc., DOI 10.1002/int.21514.

Bibliography

- [12] Daniele, E.: Aerodynamic design and preliminary aeroelastic analysis of a 50 KW HAWT's rotor (only in italian). Master's Thesis, Department of Aerospace Engineering, University of Naples Federico II (2009).
- [13] Daniele, E., Nicolosi, F., Coiro, D.P.: Improvements in performance estimation of wind turbine blade airfoils at low Reynolds number. In: 3rd CEAS Air & Space Conference, 21th AIDAA Congress, October 24 - 27, 2011, San Giorgio Maggiore Island, Venice, Italy, ISBN 9788896427187.
- [14] Daniele, E., Herraes, I., Stoevesandt, B., Peinke, J.: DES study of airfoil lift coefficient sensitivity to flow turbulence. In: Proceedings of Wind Energy and the impact of turbulence on the conversion process, EUROMECH Colloquium 528, Oldenburg, Germany 22nd-24th February 2012.
- [15] Daniele, E., De Fenza, A., Della Vecchia, P.: Conceptual adaptive wing-tip design for pollution reductions. In: Journal of Intelligent Materials Systems and Structures, Volume 23, Issue 11, pp. 1197-2212 (2012). DOI 10.1177/1045389X12445030.
- [16] Dillsaver, M.J.: Experimental Investigation of Oblique Wing Aerodynamics at Low Speed. Master Thesis, Department of the Air Force, Air University, Air Force Institute of Technology, Wright-Patterson Air Force Base, Ohio (2007).
- [17] Drela, M.: XFOIL: An Analyse and Design System for Low Reynolds Number Airfoils. In: Low Reynolds Number Aerodynamics, Springer Verlag Lecture Notes in Engineering, Vol. 54 (1989).
- [18] Drela, M.: Newton solution of coupled viscous/inviscid multielement airfoil flows. In: AIAA, Fluid Dynamics, Plasma Dynamics and Lasers Conference, Seattle, WA, June 1990. American Institute of Aeronautics and Astronautics (AIAA). AIAA Paper no. 90-1470 (1990).
- [19] Ewald, B.F.R.: Wind tunnel wall correction. In: AGARDograph 336 (1998).
- [20] FAST: An Aeroelastic Computer-Aided Engineering Tool for Horizontal Axis Wind Turbines. NWTC Computer-Aided Engineering Tools (FAST by Jason Jonkman, Ph.D.). <http://wind.nrel.gov/designcodes/simulators/fast/>, (2012).
- [21] Garner, H.C., Rogers, E.W.W., Acum, W.E.A., Maskell, E.C.: Subsonic wind tunnel wall corrections. In: AGARDograph 109 (1966).
- [22] Garad-Hassan: Bladed, Wind Turbine Design Software, <http://www.gl-garradhasan.com/en/software/GHBladed.php>
- [23] Gregory, N., O'Reilly, C.L.: Low-speed aerodynamic characteristics of NACA 0012 aerofoil section, including the effects of upper-surface roughness simulating hoar frost. In: Aeronautical Research Council reports and memoranda no. 3726 (1973).
- [24] Hau, E.: Wind Turbines Fundamentals, Technologies, Application, Economics. Springer Verlag, ISBN 978-3-540-24240-6 (2006).

- [25] Hoener, S.F.: Fluid Dynamic Drag: Practical Information on Aerodynamic Drag and Hydrodynamic Resistance. Published by Hoerner Fluid Dynamics, ISBN 978-9991194448 (1965).
- [26] Iyer, V.: A Wall Correction Program Based on Classical Methods for the National Transonic Facility (Solid Wall or Slotted Wall) and the 14x22-Ft Subsonic Tunnel at NASA LaRC. In: NASA/CR-2004-213261(2004).s
- [27] Jacobs, R. G., Durbin, P. A.: Simulations of Bypass Transition. In: J. Fluid Mech., 428, pp. 185-212 (2001). 7th-10th January, 2008, Grand Sierra Resort - Reno, Nevada.
- [28] Klebanoff, P. S.: Effects of Free-Stream Turbulence on a Laminar Boundary Layer. In: Bull. Am. Phys. Soc., 16, p. 1323 (1971).
- [29] KPGM Advisory: Investire nelle rinnovabili: trend, opportunità, prospettive. <http://www.abilab.it/documents/10180/185915/Investire%20nelle%20Rinnovabili%200k.pdf>, (2011).
- [30] Langtry, R. B., Menter, F. R.: Transition Modeling for General CFD Applications in Aeronautics, In: AIAA, Vol. 100 (2005).
- [31] Langtry, R. B., Menter, F. R., Likki, S. R., Suzen, Y. B., Huang, P. G., Völker, S.: A Correlation-Based Transition Model Using Local Variables – Part II: Test Cases and Industrial Applications. In: Journal of Turbomachinery, Vol. 128, pp. 423-434 (2006).
- [32] Lardeau, S., Li, N., Leschziner, M. A.: Large Eddy Simulation of Transitional Boundary Layers at High Freestream Turbulence Intensity and Implications for RANS Modeling. In: ASME J. Turbomach., 129, pp. 311-317 (2007).
- [33] Leib, S. J., Wundrow, D. W., Goldstein, M. E.: Effect of FreeStream Turbulence and Other Vortical Disturbances on a Laminar Boundary Layer. In: J. Fluid Mech., Vol. 380, pp. 169-203 (2007).
- [34] Mallozzi, L., D'Amato, E., Daniele, E., Petrone, G.: N leader-M follower coaliton games with genetic algorithms and applications. In: Proceedings of EUROGEN2011 Evolutionary and Deterministic Methods for Design, Optimization and Control, edited by C. Poloni, D. Quagliarella, J.PÃ'riaux, N. Gauger and K. Giannakoglou, pp. 852-866 (2011). IISBN: 9788890632303.
- [35] Mallozzi, L., D'Amato, E., Daniele, E., Petrone, G.: Waiting time costs in a bilevel location-allocation problem. In: Contributions to game theory and management V, edited by L. A. Petrosyan and N. A. Zenkevich, Graduate School of Management, St. Petersburg University, Russia, pp. 178-186 (2012).
- [36] Maskell, E.C. : A theory of blockage effects on bluff bodies and stalled wings in a closed wind tunnel. In: Aeronautical research council reports and memoranda, no. 3400, AD-A955-243 (1963).
- [37] Matsubara, M., Alfredsson, P. H.: Disturbance Growth in Boundary Layers Subjected to Free-Stream Turbulence. In: J. Fluid Mech., Vol. 430, pp. 149-168 (2001).

Bibliography

- [38] Mayda, E.A., van Dam, C.P.: Bubble-Induced Unsteadiness on A Wind Turbine Airfoil. In: *Journal of Solar Energy Engineering*, Vol. 124, pp. 335-344 (2002).
- [39] McArthur, J.: *Aerodynamics of wings at low Reynolds numbers*. Ph.D. Thesis in Aerospace and Mechanical Engineering, University of Southern California (2007).
- [40] Menter, F. R.: Two-equation Eddy-viscosity turbulence models for engineering applications. In: *AIAA J.*, Vol. 32(8), pp. 1598-1605 (1994).
- [41] Menter, F. R., Langtry, R. B., Likki, S. R., Suzen, Y. B., Huang, P. G., Völker, S.: A Correlation-Based Transition Model Using Local Variables – Part I: Model Formulation. In: *Journal of Turbomachinery*, Vol. 128, pp. 413-422 (2006).
- [42] Menter, F. R., Langtry, R. B., Völker, S.: Transition Modelling for General Purpose CFD Codes. In: *Flow, Turbulence and Combustion*, Springer, Vol. 77, pp. 277-303 (2006).
- [43] OpenFOAM is a free, open source CFD software package: <http://www.openfoam.com/>.
- [44] Ostowari C., Naik D.: Post Stall Studies of Untwisted Varying Aspect Ratio Blades with an NACA 4415 Airfoil Section - Part I. In: *Wind Engineering*, Vol. 8, No. 3, pp. 176-194 (1984).
- [45] Ostowari C., Naik D.: Post Stall Studies of Untwisted Varying Aspect Ratio Blades with an NACA 4415 Airfoil Section - Part II. In: *Wind Engineering*, Vol. 9, No. 3, pp. 149-164 (1985).
- [46] Ostowari C., Naik D.: Post-Stall Wind Tunnel Data for NACA 44XX Series Airfoil Sections. In: *SERI/STR-217-2559*, UC Category: 60, DE85002948 (1985).
- [47] Paraschivoiu, I.: *Wind Turbine Design : With Emphasis on Darrieus Concept*. Presses Polytechnique de Montréal, ISBN 978-2553009310 (2002).
- [48] ParaView is an open-source, multi-platform data analysis and visualization application: <http://www.paraview.org/>.
- [49] Parlamento Italiano: Disposizioni per la formazione del bilancio annuale e pluriennale dello Stato (legge finanziaria 2008). In: *Legge n.244/07*, <http://www.parlamento.it/parlam/leggi/072441.pdf>, (2007).
- [50] Pehlivanoglu, M.Y.V.: Representation method effects on vibrational genetic algorithm in 2-D Airfoil Design. In: *Journal of aeronautics and Space Technologies*, July, Vol. 4, no. 2, pagg. 7-13 (2009).
- [51] Presidenza della Repubblica Italiana: Attuazione della direttiva 2009/28/CE sulla promozione dell'uso dell'energia da fonti rinnovabili, recante modifica e successiva abrogazione delle direttive 2001/77/CE e 2003/30/CE. (11G0067). In: *Decreto legislativo 3 marzo 2011, n. 28*, <http://www.normattiva.it/uri-res/N2Ls?urn:nir:stato:decreto.legislativo:2011;028>, (2011).

- [52] Rainbird, J.: The aerodynamics development of a vertical axis wind turbine. Master's thesis, School of Engineering, University of Durham, (2007).
- [53] Redford, J.A., Johnson, M.W.: Predicting Transitional Separation Bubbles. In: *Journal of Turbomachinery*, Vol. 127, pp. 497-501 (2005).
- [54] Ren, N., Ou, J.: Dust Effect on the Performance of Wind Turbine Airfoils. In: *J. Electromagnetic Analysis & Applications*, Vol.1, pp. 102-107, DOI:10.4236/jemaa.2009.12016 (2009).
- [55] Rumsey, C.L., Spalart, P. R.: Turbulence Model Behavior in Low Reynolds Number Regions of Aerodynamic Flowfields. In: 38th AIAA Fluid Dynamics Conference and Exhibit, Seattle, WA, June 23-26, 2008.
- [56] Scanivalve ZOC33 miniature pressure scanner data sheet and user manual: <http://www.scanivalve.com/products/pressure-measurement/miniature-pressure-scanners/zoc33-miniature-pressure-scanner/>.
- [57] Schlichting, H., Gersten, K.: *Boundary Layer Theory*. 8th ed., Springer-Verlag, Berlin (2000).
- [58] Schneemann, J., Knebel, P., Milan, P., Peinke, J.: Lift measurements in unsteady flow conditions. EWEC 2010, 20th-23rd april 2010, Warsaw, Poland.
- [59] Sheldahl, R.E., Kilmas, P.C., Feltz, L.V.: Aerodynamic Performance of a 5-Metre-Diameter Darrieus Turbine With Extruded Aluminium NACA-0015 Blades. In: SAND80-0179 U.S. Government Printing Office, (1980).
- [60] Sheldahl, R.E., Kilmas, P.C.: Aerodynamic Characteristics of Seven Symmetrical Airfoil Sections Through 180-Degree Angle of Attack for Use in Aerodynamic Analysis of Vertical Axis Wind Turbines. In: SAND80-2114 U.S. Government Printing Office, (1981).
- [61] Shih, T.-H., Liou, W. W., Shabbir, A., Yang, Z., Zhu, J.: A New $k - \omega$ Eddy Viscosity Model for High Reynolds Number Turbulent Flows. In: *Comput. Fluids*, Vol. 24, pp. 227-238 (1995).
- [62] Somers, D.M.: Design and Experimental Results for the S809 Airfoil. In: NREL/SR-440-6918, UC Category: 1213, DE97000206 (1997).
- [63] Somers, D.M., Tangler, J.L.: Wind-Tunnel Tests of Two Airfoils for Wind Turbines Operating at High Reynolds Numbers. In: NREL/CP-500-27891, presented at the ASME Wind Energy Symposium, Reno, Nevada, January 10-13 (2000).
- [64] Spalart, P.R., Allmaras, S.R.: A one-equation turbulence model for aerodynamic flows. In: *Recherche Aerospaciale*, No. 1, pp. 5-21 (1994).
- [65] Spalart, P.R., Rumsey, C.L.: Effective Inflow Conditions for Turbulence Models in Aerodynamic Calculations. In: *AIAA Journal*, Vol. 45, No. 10, pp. 2544-2553 (2007).
- [66] Spera, D.: Models of Lift and Drag Coefficients of Stalled and Unstalled Airfoils in Wind Turbines and Wind Tunnels. In: NASA/CR2008-215434 (2008).

Bibliography

- [67] Taghavi-Zenouz, R., Salari, M., Etemadi, M.: Prediction of laminar, transitional and turbulent flow regimes, based on three-equation $k - \omega$ turbulence model. In: *The Aeronautical Journal*, Vol. 112, no. 1134, pp. 469-476 (2008).
- [68] Taira, K. Dickson, W.B., Colonius, T., Dickinson, M.H., Rowley, C.W.: Unsteadiness in flow over a flat plate at angle-of-attack at low Reynolds numbers. In: *AIAA Paper 2007-710* (2007).
- [69] Taira, K., Colonius, T.: Three-dimensional flows around low-aspect-ratio wings at low Reynolds numbers. In: *J. Fluid Mech.*, vol. 623, pp. 187-207, DOI:10.1017/S0022112008005314 (2009).
- [70] Tancredi, S., D'Amato, E., Daniele, E., Della Vecchia, P., Petrone, G.: A Nash equilibrium-genetic algorithm optimization code for structural problems. test case: an aluminum plate subjected to low velocity impact events. In: *2010 ENGINSOFT International Conference, CAE Technologies for Industry and ANSYS Italian Conference Proceedings, Brescia, Italy, 21-22 October 2010*.
- [71] Tangler, J.L.: The Nebulous Art of Using Wind Tunnel Aerofoil Data for Predicting Rotor Performance. In: *Wind Energy*, Vol. 5, pp. 245-257, DOI: 10.1002/we.71 (2002).
- [72] Tangler, J.L.: Insight into wind turbine stall and post-stall aerodynamics. In: *Wind Energy*, Vol. 7, Issue 3, pp. 247-260, July/September 2004, DOI: 10.1002/we.122 (2004).
- [73] Tangler, J.L., Kocurek, J.D.: Wind Turbine Post-Stall Airfoil Performance Characteristics Guidelines for Blade-Element Momentum Methods. In: *NREL/CP-500-36900*. Presented at the 43rd AIAA Aerospace Sciences Meeting and Exhibit, Reno, Nevada, January 10-13, 2005 (2005).
- [74] Timmer, W.A., van Rooij, R.P.J.O.M.: Summary of the Delft University wind turbine dedicated airfoils. In: *AIAA paper 2003-0352* (2003).
- [75] Timmer, W.A.: Two-dimensional low-Reynolds number wind tunnel results for airfoil NACA 0018. In: *Wind Engineering*, Vol. 32, no. 6, pp. 525-537 (2008).
- [76] Tognaccini, R.: *Lezioni di aerodinamica dell'ala rotante, eliche, rotori ed aeromotori*. Department of Aerospace Engineering, University of Naples Federico II, http://wpage.unina.it/rtogna/Aerodinamica_del_rotore_2011.pdf (2011).
- [77] Rooij, R.P.J.O.M. van, Timmer, W.A.: Roughness Sensitivity Considerations for Thick Rotor Blade Airfoils. In: *Transactions of the ASME*, Vol. 125, pp. 468-478 (2003).
- [78] Viterna, L.A., Corrigan, R.D.: Fixed pitch rotor performance of large horizontal axis wind turbines. In: *NTRS*, 83N19233 (1982).
- [79] Viterna, L.A., Janetzke, D.C.: Theoretical and Experimental Power from Large Horizontal-Axis Wind Turbine. In: *NASA TM-82944* (1982).

- [80] Volino, R. J., Simon, T. W.: Boundary Layer Transition Under High Free-Stream Turbulence and Strong Acceleration Conditions: Part 2-Turbulent Transport Results. In: ASME J. Heat Transfer, Vol. 119, pp. 427-432 (1997).
- [81] Walters, D. K., Leylek, J. H.: A New Model for Boundary Layer Transition Using a Single-Point RANS Approach. In: ASME J. Turbomach., Vol. 126, pp. 193-202 (2004).
- [82] Walters, D. K., Leylek, J. H.: A CFD Study of Wake-Induced Transition on a Compressor-Like Flat Plate. In: ASME J. Turbomach., Vol. 127, pp. 52-63 (2005).
- [83] Walters, D.K., Cokljat, D.: A Three-Equation Eddy-Viscosity Model for Reynolds-Averaged Navier-Stokes Simulations of Transitional Flow. In: Journal of Fluids Engineering, Vol. 130, no. 12, 121401 (14 pages) (2008).
- [84] Worasinchai S., Ingram, G., Dominy, R.: A low-Reynolds-number, high-angle-of-attack investigation of wind turbine aerofoils. In: Proceedings of the Institution of Mechanical Engineers, Part A: Journal of Power and Energy, Vol. 225, pp. 748-763, DOI: 10.1177/0957650911405411, <http://pia.sagepub.com/content/225/6/748>, (2011).
- [85] Zahle, F., Sørensen, N.N., Johansen, J.: CFD Study of a NACA 63-415 Aerofoil Fitted with Stall Strips. In: Risø-R-1370(EN) (2002).
- [86] Zhang, Y., Igarashi, T., Hu, H.: Experimental Investigations on the Performance Degradation of a Low-Reynolds-Number Airfoil with Distributed Leading Edge Roughness. In: 49th AIAA Aerospace Sciences Meeting including the New Horizons Forum and Aerospace Exposition 4-7 January 2011, Orlando, Florida, AIAA 2011-1102 (2011).